

Near-field Optical Properties of InN Nanostructures

By

KISHORE KUMAR MADAPU

Enrolment No: PHYS 02 2013 04 012

**Indira Gandhi Centre for Atomic Research, Kalpakkam,
Tamil Nadu-603102, India**

A thesis submitted to the

Board of Studies in Physical Sciences

In partial fulfillment of requirements

for the Degree of

DOCTOR OF PHILOSOPHY

of

HOMI BHABHA NATIONAL INSTITUTE




August, 2018

Homi Bhabha National Institute¹

Recommendations of the Viva Voce Committee

As members of the Viva Voce Committee, we certify that we have read the dissertation prepared by **Kishore Kumar Madapu** entitled "**Near-field optical properties of InN nanostructures**" and recommend that it may be accepted as fulfilling the thesis requirement for the award of Degree of Doctor of Philosophy.


Chairman - Dr. M. Kamruddin Date: 28/11/18


Guide / Convener - Dr. Sandip Kumar Dhara Date: 28/11/18

Co-guide - <Name> (if any) N. A Date: 28/11/2018


Examiner - Dr. Chuan-Pu Liu Date: 28.11.18


Member 1- Dr. Arup Dasgupta Date: 28/11/2018

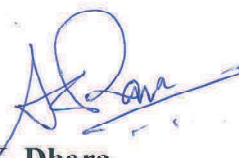
Member 2- Dr. T. R. Ravindran Date: 28/11/2018

Final approval and acceptance of this thesis is contingent upon the candidate's submission of the final copies of the thesis to HBNI.

I/We hereby certify that I/we have read this thesis prepared under my/our direction and recommend that it may be accepted as fulfilling the thesis requirement.

Date: 28/11/2018

Place: Karpakkam


Dr. S. K. Dhara
Guide

STATEMENT BY AUTHOR

This dissertation has been submitted in partial fulfillment of requirements for an advanced degree at Homi Bhabha National Institute (HBNI) and is deposited in the Library to be made available to borrowers under rules of the HBNI.

Brief quotations from this dissertation are allowable without special permission, provided that accurate acknowledgement of source is made. Requests for permission for extended quotation from or reproduction of this manuscript in whole or in part may be granted by the Competent Authority of HBNI when in his or her judgment the proposed use of the material is in the interests of scholarship. In all other instances, however, permission must be obtained from the author.



Kishore Kumar Madapu

DECLARATION

I, hereby declare that the investigation presented in the thesis has been carried out by me. The work is original and has not been submitted earlier as a whole or in part for a degree / diploma at this or any other Institution / University.



Kishore Kumar Madapu

List of Publications Arising from the Thesis

Journals

1. Surface-enhanced Raman spectroscopy using 2D plasmons of InN Nanostructures
Kishore K. Madapu and Sandip Dhara
Appl. Phys. A, **2018**, 124, 435; doi:10.1007/s00339-018-1845-5
2. Observation of surface plasmon polaritons in 2D electron gas of surface electron accumulation in InN nanostructures
Kishore K. Madapu, A. K Sivadasan, M. Baral and Sandip Dhara,
Nanotechnology, **2018**, 29, 275707; doi:10.1088/1361-6528/aabe60
3. Excitation dependent Raman studies of self-seeded grown InN nanoparticles with different carrier concentration
Kishore K. Madapu, S. R. Polaki and Sandip Dhara
Phys. Chem. Chem. Phys., **2016**, 18, 18584; doi: 10.1039/C6CP02405J
4. Effect of strain relaxation and the Burstein–Moss energy shift on the optical properties of InN films grown in the self-seeded catalytic process
Kishore K. Madapu and Sandip Dhara
CrystEngComm, **2016**, 18, 3114; doi: 10.1039/C5CE02339D
5. Growth of InN quantum dots to nanorods: a competition between nucleation and growth rates
Kishore K. Madapu, Sandip Dhara, S. Polaki, S. Amirthapandian and A. K. Tyagi
CrystEngComm, **2015**, 17, 3139; doi: 10.1039/C5CE00053J

In Preparation

1. Size-dependent work function of Si-doped InN nanorods studied using Kelvin Probe Force Microscopy and role of surface band bending
Kishore K. Madapu, S. Parida, Sandip Dhara and K. Jeganathan
(*Under preparation*)

National and International Conferences

1. Imaging of surface plasmon polaritons of 2D plasmons of InN nanostructures having Surface Electron Accumulation (***Contributory Presentation***)
Kishore K. Madapu, and Sandip Dhara
Intl. Symp. on Growth of III-Nitrides (ISGN) (August 5-10, **2018**, Unipress), Warsaw, Poland.
2. Surface band bending of InN nanostructures using Kelvin probe force microscopy
Kishore K. Madapu, Santanu Parida and S. Dhara
Res. Scholars Meet on Mater. Sci. and Engg. of Nucl. Mater.-HBNI-2018 (May 7-9, **2018**, IGCAR), Kalpakkam, India.
3. Observation of surface plasmon polariton in InN nanostructures using the near field scanning optical microscopy
Kishore K. Madapu, A. K Sivadasan, and Sandip Dhara
Nano India (March 15-16, **2017**, IIT Delhi), New Delhi, India.
4. Near field optical and spectroscopic imaging of InN nanostructures
Kishore K. Madapu, A. K. Sivadasan and Sandip Dhara
61st Dept. of Atomic Energy-Solid State Phys. Symp. (DAE-SSPS) (December 26-30, **2016**, KIIT University), Bhubaneswar, India.
5. Burstein-Moss and strain effects on optical properties of degenerate InN Nanocrystals
Kishore K. Madapu, Sandip Dhara
Emerging Trends in Adv. Func. Mater. (ETA FM) (January 18-21, **2016**, Institute of Physics), Bhubaneswar, India.
6. Investigation of gas sensing properties of InN nanoparticles
Kishore K. Madapu, A. K. Prasad, A. K. Tyagi, and Sandip Dhara
59th Dept. of Atomic Energy-Solid State Phys. Symp. (DAE-SSPS) (December 16-20, **2015**, VIT University), Vellore, Tamil Nadu, India.
7. Role of phase transformation temperature in the growth of InN nanorods
Kishore K. Madapu, Sandip Dhara, and A. K. Tyagi
Intl. Conf. on Nano Sci. and Technol. (CONSAT), (March 3-5, **2014**, Institute of Nano science and Technology) Chandigarh, India.
8. Optimization of growth of InN nanorods using chemical vapor deposition and electrical characterization
Kishore K. Madapu, and Sandip Dhara
Intl. Union of Mater. Res. Soc.-Intl. Conf. in Asia (IUMRS-ICA) (December 16-20, **2013**, JNCASR) Bangalore, India.
9. Raman Spectroscopic Imaging of III-V Nitride Nanostructures
Sandip Dhara, P. Sahoo, A. Patsha, **Kishore K. Madapu** and A. K. Tyagi

Intl. Union of Mater. Res. Soc.-Intl. Conf. in Asia (IUMRS-ICA) (December 16-20, **2013**, JNCASR) Bangalore, India.

10. Growth of InN nanostructures using chemical vapor deposition
Kishore K. Madapu, Sandip Dhara and S. Polaki
Mater. Res. Soc. of India-AGM (MRSI-AGM), (January 11-15, **2013**, IGCAR), Kalpakkam, India.

Conference Proceedings

1. Near field optical and spectroscopic imaging of InN nanostructures
Kishore K. Madapu, A. K. Sivadasan and Sandip Dhara
AIP Conf. Proc., **2017**, 1832, 050147; doi: 10.1063/1.4980380
2. Investigation of gas sensing properties of InN nanoparticles
Kishore K. Madapu, A. K. Prasad, A. K. Tyagi, Sandip Dhara
AIP Conf. Proc., **2015**, 1665, 050089; doi: 10.1063/1.4917730

Other Journal Publications (Not Included in the Thesis)

1. Synthesis, microstructure and visible luminescence properties of vertically aligned lightly doped porous silicon nanowalls
A. K. Behera, R. N. Viswanatha, C.Lakshmanan, **Kishore K. Madapu**, M.Kamruddin and T.Mathews
Microporous and Mesoporous Mater. **2018**, 273, 99.
2. In-situ formation of Ge-rich SiGe alloy by electron beam evaporation and the effect of post deposition annealing on the energy band gap
Ch. K. Singh, T. Tah, **Kishore K. Madapu**, K. Saravanan, S. Ilango and S. Dash
Mater. Sci. in Semicond. Process. **2018**, 18, 31.
3. Microwave plasma induced surface modification of diamond-like carbon films
S. R. Polaki, N. Kumar, N. G. Krishna, **Kishore K. Madapu**, M. Kamruddin, S. Dash and A. K.Tyagi
Surf. Topogr. : Metrol. Prop. **2017**, 5, 045005.
4. Au induced crystallization and layer exchange in a-Si/Au thin film on glass below and above the eutectic temperature
Ch .K. Singh, T. Tah, **Kishore K. Madapu**, K. Saravanan, S. Ilango and S.Dash
J. Non-Cryst. Solids **2017**, 460, 130.

5. Interpretation of friction and wear in DLC film: Role of surface chemistry and test environment
S. R. Polaki, N. Kumar, **Kishore K. Madapu**, K. Ganesan, N. G. Krishna, S. K. Srivastava, S. Abhaya, M. Kamruddin, S. Dash and A. K. Tyagi
J. Phys. D: Appl. Phys. **2016**, 49, 44.
6. The light–matter interaction of a single semiconducting AlGaN nanowire and noble metal Au nanoparticles in the sub-diffraction limit
A. K. Sivadasan, **Kishore K. Madapu** and Sandip Dhara
Phys. Chem. Chem. Phys. **2016**, 18, 23680.
7. Nano scale investigation of particulate contribution to diamond like carbon film by pulsed laser deposition
M. Panda, G. Mangamma, R. Krishnan, **Kishore K. Madapu**, D. N. G. Krishna, S. Dash and A. K. Tyagi
RSC Adv. **2016**, 6, 6016.
8. Tribological behavior of hydrogenated DLC film: Chemical and physical transformations at nano-scale
S. R. Polaki, N. Kumar, K. Ganesan, **Kishore K. Madapu**, A. Bahuguna, M. Kamruddin, S. Dash and A. K. Tyagi
Wear, **2015**, 338, 105.
9. Imaging nanostructures by Raman spectral mapping
A. Patsha, **Kishore K. Madapu**, Sandip Dhara
MAPAN-Journal of Metrology Society of India **2013**, 28, 279.



Kishore Kumar Madapu

Dedicated to

My Sister Late Smt. Mamatha

ACKNOWLEDGEMENTS

Firstly, I would like to express my sincere gratitude to my advisor Prof. Sandip Kumar Dhara for the continuous support of my Ph.D study and related research, for his patience, motivation, and immense knowledge. I could not have imagined having a better advisor and mentor for my Ph.D study.

Besides my advisor, my sincere thanks to the doctoral committee chairman Dr. M. Kamruddin, and members Dr. Arup Dasgupta and Dr. T. R. Ravindran for their insightful comments and encouragement.

I convey my gratitude to Dr. G. Amarendra, Director, Materials Science Group, for his encouragement in conducting the thesis work. I also bestow my regards to the Director of IGCAR for facilitating the research activities.

I convey my deep gratitude to my research collaborators Dr. S. Amirthapandian, Dr. S. R. Polaki, Dr. A. K. Sivadasan, Mr. Santanu Parida of IGCAR, Dr. T. Ganguly and Ms. M. Baral of RRCAT, Indore and Dr. K. Jeganathan of Bharathidasan University, Tamil Nadu. I want to thank the reviewers of my manuscripts for their valuable comments and suggestions which helped in fine-tuning the ideas for my research.

I deeply express my heart full thanks to all of my colleagues Dr. G.Mangamma, Dr. A. Das, Dr. A. K. Prasad and present NCSS members. I thank Dr. Prasana K. Sahoo for introducing the CVD system to me and making my research work easy. It is a pleasure to thank my friends and former research scholars Dr. Avinash Patsha, Dr. B.V. Ramana, and Dr. Subrata Ghosh for not only sharing scientific adventures but also for making the workplace pleasant. I would also like to thank present research scholars Ms. Raktima Basu, Mr. Binaya Kumar Sahu, and Mr. Gopinath Sahoo for their help at the laboratory.

In this occasion, I thank my training school friends Dr. G. Sainath and Mr. Nagaraju Bekkenti for their excellent off-research companion at IGCAR and home.

I owe deep gratitude to my parents Bikshama Chary (Bapu) and Radha (Amma), my brother Madhav (Anna) and my late sister Mamatha (Akka) who are the driving force behind my every achievement.

Finally, I would like to thank my wife (Swathi) and son (Vedhaansh) for allowing me to stay late hours and for everything else.

CONTENTS

| | Page No. |
|--|-----------------|
| SYNOPSIS | i |
| LIST OF FIGURES | ix |
| LIST OF TABLES | xiii |
| CHAPTER 1: INTRODUCTION | 1 |
| 1.1 Indium Nitride | 1 |
| 1.1.1 Crystal structure | 2 |
| 1.1.2 InN: Difficulties in the synthesis | 4 |
| 1.1.3 InN nanostructures | 6 |
| 1.1.4 Surface electron accumulation of InN | 7 |
| 1.2 Optical Properties of InN | 8 |
| 1.3 Vibrational Properties of InN | 10 |
| 1.4 Work Function of InN | 13 |
| 1.5 InN as Plasmonic Material | 13 |
| 1.6 Objective and Overview of the Thesis | 15 |
| 1.7 References | 18 |
| CHAPTER 2: GROWTH AND EXPERIMENTAL TECHNIQUES | 23 |
| 2.1 Growth Techniques | 23 |
| 2.1.1 Atmospheric pressure chemical vapour deposition | 23 |
| 2.1.2 Plasma-assisted molecular beam epitaxy | 27 |
| 2.2 Near-Field Light-Matter Interaction | 29 |
| 2.2.1 Near-field scanning optical microscopy | 29 |
| 2.2.2 Surface plasmon polaritons: Role of NSOM | 34 |
| 2.3 Work Function Measurements: Kelvin Probe Force Microscopy | 35 |
| 2.4 Surface Electron Accumulation: UV Photoemission Spectroscopy | 38 |
| 2.5 Other Characterization Techniques | 39 |
| 2.5.1 Raman and photoluminescence spectroscopy | 39 |
| 2.5.2 Morphological studies and structural analysis | 40 |
| 2.6 Conclusion | 41 |

| | | |
|-------------------|--|-----------|
| 2.7 | References | 41 |
| CHAPTER 3: | GROWTH OF InN NANOSTRUCTURES AND FILMS | 43 |
| 3.1 | Introduction | 43 |
| 3.2 | Growth of InN Nanostructures and Nanorods Using In ₂ O ₃ | 44 |
| 3.2.1 | Morphological and structural studies | 45 |
| 3.2.2 | Raman spectroscopic studies | 50 |
| 3.2.3 | Evolution of nanorod growth and optimization | 52 |
| 3.2.4 | Growth mechanism of nanorods | 55 |
| 3.3 | Growth of InN Thin Films | 60 |
| 3.3.1 | Growth mechanism of InN films | 61 |
| 3.3.2 | Morphology and structural studies | 62 |
| 3.3.3 | Raman spectroscopic studies: Effect of strain and carrier density | 63 |
| 3.3.4 | Photoluminescence spectroscopic studies: Effect of strain and Burstein-Moss shift | 70 |
| 3.4 | Conclusion | 74 |
| 3.5 | References | 75 |
| CHAPTER 4: | GROWTH OF InN NANOSTRUCTURES ON SAPPHIRE SUBSTRATE AND EXCITATION DEPENDENT RAMAN STUDIES | 77 |
| 4.1 | Introduction | 77 |
| 4.2 | Growth of InN Nanostructures on Sapphire Substrate | 78 |
| 4.2.1 | Growth and morphological studies | 78 |
| 4.2.2 | Raman spectroscopic studies: Observation of 2D plasmon peak | 79 |
| 4.2.3 | PL and UPS studies: Confirmation of surface electron accumulation | 84 |
| 4.3 | Excitation Dependent Raman Studies of InN Nanostructures | 87 |
| 4.4 | Conclusion | 93 |
| 4.5 | References | 94 |

| | |
|--|------------|
| CHAPTER 5: NEAR-FIELD LIGHT-MATTER INTERACTION OF InN NANOSTRUCTURES AND PLASMONIC PROPERTIES | 97 |
| 5.1 Introduction | 97 |
| 5.2 Near-field Light-matter Interaction of InN Nanostructures | 100 |
| 5.2.1 NSOM imaging of nanostructures grown at 580 °C | 100 |
| 5.2.2 NSOM imaging of nanostructures grown at 620 °C | 103 |
| 5.2.3 NSOM imaging of nanostructures grown at 630 °C | 104 |
| 5.3 SERS Activity of InN Nanostructures | 109 |
| 5.4 Conclusion | 119 |
| 5.5 References | 120 |
| CHAPTER 6: WORK FUNCTION MEASUREMENTS OF InN NANOSTRUCTURES | 123 |
| 6.1 Introduction | 123 |
| 6.2 Raman and PL Spectroscopic Studies | 125 |
| 6.3 Kelvin Probe Force Microscopy Study of InN nanostructures | 127 |
| 6.3.1 KPFM measurements on undoped InN nanorods | 127 |
| 6.3.2 KPFM measurements on Si-doped InN nanorods | 128 |
| 6.4 Conclusion | 133 |
| 6.5 References | 134 |
| CHAPTER 7: SUMMARY OF THESIS AND SCOPE FOR FUTURE WORK | 137 |
| 7.1 Summary of Thesis | 137 |
| 7.2 Scope for Future Work | 140 |

LIST OF FIGURES

| Figure No. | Title of the Figure | Page No. |
|------------|---|----------|
| 1.1 | (a) Stick and ball representation of unit cell of the <i>wurtzite</i> InN structure. (b) Important crystal planes of the wurtzite hexagonal structure. (c) Top view of the crystal planes. | 2 |
| 1.2 | Melting points of III-nitrides and equilibrium N ₂ pressure over the III-nitrides system from the high pressure experiments and theoretical calculation. | 4 |
| 1.3 | Calculated conduction and valence band dispersion of InN using the <i>k</i> · <i>p</i> model. | 9 |
| 1.4 | Schematic illustration of atomic motions corresponds to different optical phonon modes. | 11 |
| 2.1 | Schematic of the home made APCVD experimental setup. | 25 |
| 2.2 | Schematic of a typical cross-sectional view of MBE chamber. | 28 |
| 2.3 | Schematic of Synge proposal to overcome the diffraction limit. | 30 |
| 2.4 | Schematic of NSOM technique used for the study of near-field optical properties of InN nanostructures. Inset of the figure shows the schematic of the evanescent field at the end of the aperture. | 33 |
| 2.5 | Schematic band diagram illustrating the principle of KPFM technique. b) Schematic of an experimental technique of KPFM. | 36 |
| 3.1 | Morphology of InN nanostructures grown at different temperatures a) 550, b) 600, c) 650 and d) 700 °C. | 45 |
| 3.2 | Low and high-resolution TEM images of nanostructures grown at 550 and 650 °C. (a)–(c) The size distribution of nanoparticles grown at 550 °C. d) Low magnification image of NRs grown at 650 °C. | 46 |
| 3.3 | Detailed HRTEM analysis of NR grown at 650 °C. a) Low magnification image of apex part of NR which shows that the angle between growth direction and surface facet planes is 60°. b) and c) HRTEM images of apex part of NR and its enlarged view, respectively, showing the (10–10) lattice fringes. d) FFT of apex part of the NR (area is indicated by red square in (c)). e) Low magnification image of NR shows the growth direction of middle part. f) and g) High-resolution images of middle part of the NR and its enlarged view, respectively, showing the lattice fringes of (0002) planes. h) FFT of middle part of the NR (area indicated by red square in (g)). | 47 |
| 3.4 | XRD pattern of a) nanoparticles grown at 550 °C along with the substantial presence of cubic In ₂ O ₃ and b) NRs grown at 650 °C (JCPDS # 50–1239). c) Variation of atomic percentages of In, N and O in nanostructures grown at different temperatures. | 49 |
| 3.5 | Raman spectra of nanostructures grown at temperatures of (a) 550–700 °C. (b) $I(A_1(LO))/I(E_2(\text{high}))$ at different growth temperatures. Lines are drawn | 51 |

| | | |
|------|---|----|
| | as a guide to the eye. (c) Variation of E_2 mode FWHM with respect to growth temperature. A tiny peak at the shoulder of E_2 (high) mode in the range of 471–477 cm^{-1} is assigned to the E_1 (TO) (marked by *). L^- is denoted as one of the LOPC modes. | |
| 3.6 | Evolution of NRs with increase in growth temperatures a) 610 °C, b) 620 °C, c) 630 °C, and d) 640 °C. | 53 |
| 3.7 | Morphology variation with growth times of a) 1, b) 2, c) 3, and d) 4 hr at the optimized growth temperature of 650 °C. | 53 |
| 3.8 | Optimization of flow rates a) 30, b) 50, c) 70, and d) 90 sccm at a growth temperature of 640 °C, close to the optimal value. No significant change observed in the morphology above 50 sccm. | 54 |
| 3.9 | Variation of atomic percentages of In, N and O in nanostructures grown with different flow rates at 640 °C. | 55 |
| 3.10 | a) Graphical illustration of nucleation and growth rates which determine the morphology of nanostructures. b) Schematic of atomic plane arrangement of NR at different parts. The apex (nucleation part) of NR contains {10–12} semi-polar surfaces. These planes can have potential barriers for adatom diffusion because of the polarity. NRs grow along the [0001] direction such that surfaces have non-polar planes, i.e., {10–10} at high temperature (650 °C) where growth rate dominates. Diffusion of adatoms over the non-polar planes depends on temperature only. At high temperature, NRs grow with long-range atomic diffusion over non-polar surfaces. | 56 |
| 3.11 | Growth of InN with two different ramp schemes with the process steps inscribed in the insets. a) Scheme 1: no deposition observed. b) Scheme 2: successful deposition of InN observed involving four different process steps. AFM topography of the sapphire substrate c) prior to deposition and d) after process B showing uniform nucleation of the seed nanoparticles. | 62 |
| 3.12 | AFM topographical images of InN films grown at a) 560, b) 580, c) 600 and d) 650 °C showing a mosaic nature. | 63 |
| 3.13 | a) Raman spectra of InN films grown at different temperatures showing the symmetric and asymmetric nature of the A_1 (LO) mode along with other symmetry-allowed and non-zone centre phonon modes. The peaks represented by * symbols are correspond to sapphire phonon modes. b) E_2 (high) phonon mode (open circles) spectral region with the Lorentzian fit (solid red curve). c) Change in the E_2 (high) phonon mode frequency (right side scale) and its FWHM (left side scale) with respect to temperature. d) Calculated strain relaxation with the growth temperature. | 64 |
| 3.14 | a) The spectral region of the A_1 (LO) mode. b) Dependence of the A_1 (LO) mode frequency with temperature. Lines are to guide the eye. c) XRD pattern of samples grown at 580 and 650 °C (first three reflections shown here). | 67 |
| 3.15 | a) PL spectra, measured at 80 K, for the InN films grown at different temperatures. The spectra show the redshift of the emission line with the increase in temperature. (b)–(d) show the temperature-dependent PL | 71 |

| | | |
|------|--|----|
| | spectra of the 580, 600, and 650 °C grown samples with a Gaussian fit for b) and d). | |
| 3.16 | Temperature dependence of integrated PL intensity of sample grown at (a) 650 °C and (b) 580 °C. | 73 |
| 4.1 | FESEM micrographs of the InN nanostructures grown at different temperatures. (a) 580 (b) 600 °C: shows random nanostructures, (c) 620 °C: shows nanostructure with protruded hexagonal features, (d) 630 °C and (e) 650 °C: shows random nanostructures. (f)-(j) Raman spectra of InN nanostructures grown at 580, 600, 620, 630, and 650 °C. A low-frequency peak, which is attributed to the 2D plasmon excitation, is evolved in high-temperature grown samples (≥ 620 °C). The schematic of the scattering geometry is shown in the inset of the (j). | 80 |
| 4.2 | (a) Sheet carrier density-dependent 2D plasmon frequency of 2DEG corresponding to the SEA of InN and its (b) dispersion curve. (c) Variation of 2D plasmon peak frequency with increasing growth temperature. | 83 |
| 4.3 | PL spectra of the nanostructures grown at (a) 580 (b) 620, and (c) 630 °C. d) VB photoemission spectra of samples grown at 580, 620, and 630 °C. e) Pinning of Fermi level (E_F) into the conduction band shown increasing with increasing growth temperature. Line shown is a guide for the eyes. | 85 |
| 4.4 | Raman spectra collected for samples grown at different deposition temperatures with different laser excitations. a) 514.5 nm: with the higher temperature (620 and 650 °C) grown samples showing the asymmetric broadening of the $A_1(\text{LO})$ phonon mode because of Fano interference. b) 488 nm: showing similar features to the 514.5 nm excitation. c) 785 nm: a broad feature dominating in the range of 440–590 cm^{-1} with the signature of the symmetry allowed Raman modes at corresponding peak positions of α ($A_1(\text{TO})$), β ($E_2(\text{high})$), and γ ($A_1(\text{LO})$) in addition to the forbidden mode, represented by δ ($B_1(\text{high})$), dominating in the higher temperature grown samples. A dashed vertical line is indicated to show the red shift of the $B_1(\text{high})$ mode with increasing growth temperature. | 88 |
| 4.5 | Temperature-dependent Raman spectra of InN nanoparticles grown at 580 and 650 °C with Gaussian fitting. Raman spectra collected at (a) 80 K and (b) 373 K for sample grown at 580 °C with the frequency of the forbidden mode at 565 and 544 cm^{-1} respectively. Raman spectra collected at (c) 80 K and (d) 373 K for sample grown at 650 °C with the frequency of the forbidden mode at 552 and 536 cm^{-1} , respectively. | 89 |
| 4.6 | Temperature-dependent Raman spectra for (a) Sample grown at 580 °C, with the forbidden mode dominating over the $A_1(\text{LO})$ mode only at higher temperatures and for (b) Sample grown at 650 °C, with the forbidden mode dominating over $A_1(\text{LO})$ mode at all measurement temperatures. The $B_1(\text{high})$ and $A_1(\text{LO})$ phonon modes are indicated by dotted and dash-dotted lines in the both spectra, respectively, for guide to the eye. | 90 |
| 4.7 | a) PL spectrum of undoped InN NRs. Inset shows the NIR PL emission. b) PL spectrum of Si-doped InN NRs. c) Raman spectrum of the undoped InN NRs. d) Raman spectrum of the Si-doped InN NRs. Inset of the | 92 |

| | | |
|-----|---|-----|
| | figures (c) and (d) shows the morphology undoped and Si-doped InN NRs. | |
| 5.1 | (a), (b), (c) Topography of sample grown at 580 °C and the corresponding (d), (e), (f) NSOM images, respectively. c) Zoomed scan of Fig. b (Dashed area). Observed optical contrasts in the NSOM images attributed to variation in the carrier density of individual nanoparticles. | 101 |
| 5.2 | (a) Topography and corresponding (c) NSOM images of sample grown at 620 °C. NSOM images showing the strong extinction of the light at some of the nanoparticles and near-field enhancement around them. (b) Zoomed scan of (a) and (d) being the corresponding NSOM image showing similar kind of topography and optical images. Correlated particles in the topography and NSOM images are shown with circles and ellipses. (e) and (f) showing the line profile of scattered intensity across the nanoparticles indicated by the blue arrows. | 104 |
| 5.3 | (a) Topography and corresponding (b) NSOM images of sample grown at 630 °C. A similar kind of near-field enhancement around each nanoparticle, as in the case of sample grown at 620 °C, is observed in the NSOM image, except for a prominent absorption around the nanoparticles. | 105 |
| 5.4 | (a), (e) Topography and corresponding (b), (f) NSOM images, respectively, for sample grown at 630 °C. (e), (f) Zoomed-in scan of (a), (b); zoomed area is indicated by dashed lines. Periodic fringes are clearly observed because of the interference of the generated and reflected SPPs. (c), (g) Line profiles of the periodic fringes. Collected region is indicated by the blue arrows. (d), (h) 3D images corresponding to (b), (f). | 106 |
| 5.5 | (a) Topography and corresponding (b) NSOM images of the nanostructures of grown at 630 °C. Destructive interference of SPPs (in the dash-dotted area) generated by two adjacent InN nanoparticles is clearly observed. (c) Topography and corresponding (d) NSOM images show the zoomed image of the region revealing destructive interference (indicated by arrows). Corresponding 3D images are also shown in the (e) topography and (f) NSOM images. | 108 |
| 5.6 | a) SERS enhancement studies on InN nanostructures grown at 580 °C. Inset figure shows the optical images of R6G adsorbed substrate with the presence (continuous circle; Al ₂ O ₃ /InN/R6G) and the absence (dashed circle; Al ₂ O ₃ / R6G) of nanostructures where the Raman spectra were collected. b) Luminescence band of 10 ⁻³ M R6G in the presence and the absence of the InN nanostructures. | 110 |
| 5.7 | SERS and PL enhancement studies on InN nanostructures grown at 650 °C. a) Raman spectra collected in the presence (corresponding to the continuous circle) and the absence (corresponding to the dashed circle) of InN nanostructures. b) Luminescence of R6G molecules in the presence and the absence of InN nanostructures. Inset of (b) shows the area of collection of Raman and PL spectra. c) Intensity mapping of Raman mode $\nu_8 = 1651 \text{ cm}^{-1}$ showing the enhanced intensity in the presence of the InN nanostructures. | 111 |
| 5.8 | a) Normalized emission spectrum of the R6G adsorbed on the InN | 114 |

| | | |
|------|--|-----|
| | nanoparticles and R6G bulk crystals. b) and c) de-convoluted emission spectrum of adsorbed R6G on InN nanoparticles and R6G bulk crystals, respectively. The spectra were fitted with the Gaussian curves. d) Normalized emission spectrum of the R6G collected from scratch and nanoparticles area. | |
| 5.9 | SERS studies of InN nanostructures grown at 650 °C with excitation of 488 nm laser. | 115 |
| 5.10 | Near-field light-matter interaction of InN nanostructures grown at 580 and 650 °C. (a) Topography of InN nanostructures grown at 580 °C and (b) corresponding NSOM image. High magnification (c) topography and (d) NSOM image of InN nanostructures grown at 650 °C. | 117 |
| 6.1 | Raman spectra of (a) undoped and (b) Si-doped InN NRs. PL spectra of (c) undoped and (d) Si-doped InN NRs. Inset of (c) shows the NIR PL emission of the undoped InN NRs. e) and f) show the scanning electron microscopic images of undoped and Si-doped NRs. | 126 |
| 6.2 | Typical AFM topography images of undoped InN NRs and corresponding line profiles. | 127 |
| 6.3 | Topography and corresponding CPD maps of undoped NRs carried out at different areas of the substrates. | 128 |
| 6.4 | Size-dependent CPD values (right Y-axis) and corresponding calculated work function values (left Y-axis) for undoped InN NRs. | 128 |
| 6.5 | (a)-(d) Topographic images of the Si-doped InN NRs dispersed on the electron beam evaporated Au film and (e)-(h) are the corresponding CPD maps. | 129 |
| 6.6 | Size-dependent CPD values (right Y-axis) and corresponding calculated work function values (left Y-axis) for Si-doped InN NRs. | 130 |
| 6.7 | Band alignments of the coupled system of conducting AFM tip and InN NRs of sizes 50 nm (a) and 250 nm (b) before and after contact. | 131 |
| 6.8 | Photoluminescence spectra of isolated InN NRs. Inset figure shows the optical image of well dispersed NRs on SiO ₂ substrate and the scale in the figure is 10 μm. | 133 |

LIST OF TABLES

| Table No. | Title of Table | Page No. |
|-----------|---|----------|
| 1.1 | Experimental and calculated lattice parameters of the <i>wurtzite</i> structures of AlN, GaN and InN. | 3 |
| 1.2 | Experimental and calculated frequencies of symmetry allowed Raman modes. | 12 |

SYNOPSIS

Indium nitride (InN) is the member of III-nitride group along with the GaN and AlN. Among these, InN shows superior electronic properties such as high mobility and high drift velocity as compared to other nitrides because of its low effective electron mass. Because of these reasons, InN is considered as a future high-speed electronic device material. However, InN has been a less studied material as compared to other nitrides because of the difficulties in growing it as a high-quality crystalline material. Inherent properties of InN, namely, low decomposition temperature and high equilibrium pressure of N hinder the realization the high-quality material. Because of these reasons, the growth of InN is carried out using the controlled growth techniques like molecular beam epitaxy (MBE) and metal organic vapour phase epitaxy (MOVPE). However, it is essential to produce a high-quality InN phase using the atmospheric pressure chemical vapour deposition (APCVD) technique because of its capability for the synthesis at a large scale. In this thesis, optically high-quality InN material is grown using the APCVD technique, and their near-field optical properties are explored along with far-field measurements. Additionally, InN has been surrounded by the band gap controversy. In this context, a simultaneous effect of Burstein-Moss (BM) shift and residual strain on the optical emission properties of high optical quality InN films grown using the APCVD technique is studied. Moreover, InN possesses the surface electron accumulation (SEA) as a unique property. Thus, the thesis aims to explore the plasmonic properties of InN nanostructures. In addition, the effect of two-dimensional electron gas (2DEG) corresponding to the SEA in the plasmonic properties of InN and its applications in the surface-enhanced Raman spectroscopy (SERS) is explored. The

work function values of InN are estimated, and the influence of the SEA is also studied.

The crystal quality and basic phonon structure of InN are well studied using inelastic light scattering by means of Raman spectroscopy. However, the vibrational properties of InN studied using Raman spectroscopy are very much controversial despite the several reports. The controversies in the Raman spectroscopic studies of InN surround the phonon structure of the longitudinal optical ($A_1(\text{LO})$) mode. Being polar and degenerate semiconductor, the electric field associated with the LO phonons strongly interacts with the free carriers through the Fröhlich interaction, leading to the observation of plasmon-phonon coupling modes in the Raman spectrum. Additionally, InN is reported to have the widest phonon band gap and lowest photonic band gap, which prompts its application in hot carrier solar cells. Thus, carrier density and excitation dependent studies are inevitable for understanding the phonon structure of InN in near-resonance and off-resonance conditions.

The work function of semiconductors is dependent on the doping level. However, the reports on the work function values of InN are scarce. In addition, it is well known that InN possesses the SEA close to the surface region because of its narrow bandgap. As a result of the SEA, the downward band bending is observed close to the surface region. Thus, it is very important to estimate the work function values of the InN because of its degenerate nature and possession of the SEA.

The present thesis comprises the seven chapters, and the outline of each chapter is briefed in the following sections.

Chapter 1 introduces the III-nitrides with the emphasis on the InN. The basic physical properties of InN and its related materials are discussed. Difficulties in the

synthesis of InN phase are also discussed. As the InN nitride is well characterized by the optical techniques such as Raman and photoluminescence (PL) spectroscopies, more emphasis is given to its vibrational and optical properties. In addition, plasmonic materials are introduced, and the limitations of the metals are discussed. Status of degenerate semiconductors as an alternative to the metal plasmonic materials is discussed. The possibility of the degenerate InN as the plasmonic material and plasmonic nature 2DEG of the SEA is also discussed. Moreover, the importance of measurement of the work function values of InN is elaborated and the role of the SEA is discussed.

Chapter 2 details the development of the APCVD technique for the growth of InN nanostructures. The controlled growth of InN nanorods (NRs) is carried out using the plasma-assisted molecular beam epitaxy (PAMBE). Thus, PAMBE technique is also discussed in the growth techniques section. In addition, important characterization techniques such as near-field scanning optical microscopy (NSOM) and Kelvin probe force microscopy (KPFM) for studying the near-field optical properties and contact potential difference (CPD) measurements of InN nanostructures, respectively, are elaborately discussed. A short discussion is added on the UV photoemission spectroscopy (UPS) in characterization techniques, as it is used for the study of SEA properties of InN nanostructures. Finally, a brief discussion is devoted to the basic characterization techniques such as Raman spectroscopy, PL spectroscopy, scanning electron microscopy (SEM), transmission electron microscopy (TEM) and atomic force microscopy (AFM).

The growth of the InN phase is explained in **Chapter 3**. This chapter is categorized into two parts based on the source material used in the growth process. III-

nitrides have suffered from huge dislocation density in thin films because of the lack of native substrates. As a result, the crystalline quality of these materials reduces which renders the degradation in optical emission properties. Like other III-nitrides, InN also suffers from a lack of native substrates. However, nano-columns of these materials are almost free from dislocations because of their high aspect ratio and efficient strain relaxation through a nanoscale lateral dimension. Nevertheless, nano-columns also face a problem with the formation of threading dislocations near the interface due to the lattice mismatch with substrates. In the wake of these facts, the growth of the InN nanostructures is carried out using the In_2O_3 powder as a source material and NH_3 as the reactive gas in the temperature range of 550–700 °C. In this particular growth process, InN phase is formed without any substrate and catalyst material to avoid the threading dislocations. Morphology of the nanostructures solely depends on the growth temperature, evolving from the quantum dot (QD) sized nanoparticles to NRs. It is found that 630 °C is the threshold temperature for the growth of NRs. At 630 °C, nucleation starts with multifaceted particles having {10–12} surface planes. Subsequently, hexagonal polyhedral NRs are grown along the [0001] direction with non-polar surfaces of *m*-planes {10–10}. A comprehensive study is carried out to understand the evolution of nanorods as a function of growth parameters like temperature, time and gas flow rate. Temperature-dependent evolution of morphology was explained based on the competitive processes of nucleation and growth rates. QDs and nanoparticles, as a nucleation rate dominated process, are grown at relatively low temperatures. NRs are grown at high temperature due to long-range atomic diffusion through a non-polar surface where the growth rate dominates.

The crystallographic structural analysis is adapted to establish a growth mechanism for the temperature dependent morphology of nanostructures.

As mentioned earlier, the deposition and decomposition temperatures of the InN phase occur in the same range (500–650 °C), and it is comparatively easy to control such conditions with the vapour phase epitaxial techniques. As a result of it, there are hardly any reports on optical grade InN films grown APCVD technique even though it is a commercially viable technique for large-scale synthesis. For the first time, high optical quality InN films were grown on a sapphire substrate using the APCVD technique in the temperature range of 560–650 °C. The self-catalytic approach was adopted to overcome the nucleation barrier for depositing InN films. In this process, seeding of the nucleation sites and subsequent growth was performed in the presence of reactive NH₃. The simultaneous effect of strain and the BM shift on the optical emission properties of InN films is investigated using the Raman and PL spectroscopic studies. Raman spectroscopic analysis of the $E_2(\text{high})$ and $A_1(\text{LO})$ modes is carried out for the study of the strain and carrier density in these films. The existence of compressive strain in all films is revealed by Raman spectroscopic analysis and is found to relax with increasing growth temperature. Compressive strain, resulting from the lattice and thermal expansion mismatch, is relaxed at high temperature by hydrostatic tensile strain produced from the N vacancies. Strain relaxation at high temperature is further corroborated by the red shift in the optical emission line. A large blue shift of the band gap of InN (1.2 eV) is observed as a resultant effect of compressive strain in films as well as a BM shift.

In **Chapter 4**, the growth of InN nanostructures and their phonon structure is evaluated in near and off-resonance conditions. High-quality InN nanoparticles are

grown using an APCVD technique via a self-seeded catalytic approach in the temperature range of 580–650 °C. InN nanostructures are grown using the same method, which is followed for the growth of InN films. In this temperature region, the nucleation barrier of InN is overcome by seeding low density In nanoparticles before the introduction of reactive NH_3 . Samples with increasing carrier densities are grown, with the help of increasing growth temperature, to understand the role of carrier density in the optical phonon structure. The growth temperature dependent carrier density of the nanostructures and their corresponding SEA properties are studied using the Raman spectroscopy. The presence of SEA is confirmed by Raman studies, which is further corroborated by PL and UPS studies. The frequency of 2DEG corresponding to SEA is found to be in the THz region of $54\text{--}60\text{ cm}^{-1}$ ($\sim 1.6\text{--}1.8\text{ THz}$).

The excitation dependent vibrational properties of the InN nanostructures are studied using Raman spectroscopy with different laser sources. Instead of plasmon-phonon coupling, asymmetric broadening is observed in $A_1(\text{LO})$ phonon mode because of Fano interference. The Fano line shapes are observed only for the higher carrier concentration samples with the excitations of 514.5 and 488 nm. Near-resonance excitation (785 nm), invoking the possible breakdown of the selection rule, induces significant changes in the Raman spectra with the appearance of the forbidden mode $B_1(\text{high})$. The intensity and frequency of the $B_1(\text{high})$ mode are observed to be strongly dependent on the carrier concentration in the system. Thermal electrons also have an impression on the intensity of the $B_1(\text{high})$ mode along with the inherent carrier concentration. The intensity of the forbidden mode is correlated with the band filling effects by studying the luminescence properties of the InN nanostructures.

The plasmonic properties of InN nanostructures and its applications in SERS are explored in **Chapter 5**. Heavily doped semiconductors have been emerging as an alternative to low-loss plasmonic materials. Recently, two dimensional (2D) plasmons generated a lot of curiosity because of its terahertz (THz) resonance frequency. In case of 3D plasmonic material, the plasmon frequency (ω_p) is scaled with the square root of the carrier density of the system. On the other hand, in case of the 2D plasmonics ω_p depends on the in-plane wave vector as well as areal carrier density. In this context, graphene plasmonics are explored using the near-field techniques. However, the 2D plasmons can also be observed in the semiconductor inversion layers such as Si and GaAs. Moreover, materials like InAs and InN possess the inherent SEA, which can act as a 2DEG. In this chapter, the surface plasmon properties of InN nanoparticles originating from the SEA are demonstrated using the real-space mapping of the surface plasmon fields for the first time with the help of NSOM technique. The periodic fringes are observed in the NSOM images of InN nanostructures. The observed fringes are attributed to the interference of propagated and back-reflected surface plasmon polaritons (SPPs). The wavelength of the SPPs is estimated to be in the range of 274–500 nm. The observation of SPPs is solely attributed to the 2DEG corresponding to the SEA of InN. Moreover, a resonance kind of behavior with the enhancement of the near-field intensity is observed in the near-field images of InN nanostructures. Observation of SPPs indicates that InN with SEA can be a promising THz plasmonic material for light confinement.

The SEA dependent SERS activity of InN nanostructures is also explored using the Rhodamine 6G (R6G) molecules. The SERS enhancement is observed for the InN nanostructures which possess SEA. The enhancement factor of four orders

($\sim 1.4 \times 10^4$.) was calculated with the assumption of monolayer coverage of analyte molecule. The SERS enhancement of InN nanostructures is attributed to the 2D plasmonic nature of InN nanostructures invoking SEA, rather than the contributions from 3D surface plasmon resonance and chemical interaction. The role of 2D plasmon excitation in SERS enhancement is corroborated by the near-field light-matter interaction studies using NSOM.

In **Chapter 6**, CPD measurements are carried out on InN nanostructures using the KPFM in high vacuum conditions. The work function of the semiconductors is varied depending on the doping level. The CPD is measured using the KPFM to estimate the work function of the InN NRs. In order to avoid the influence of the surface adsorbed species, the KPFM measurements were carried out at high vacuum condition of $\sim 7.5 \times 10^{-7}$ mbar. The work function of doped InN NRs is found to depend on the size of NRs. Size-dependent work function of the InN NRs is attributed to the variation in the downward surface band bending caused by SEA rather than a change in the Fermi level position. The variation in the downward surface band bending of isolated NRs is confirmed from PL spectroscopic analysis.

Chapter 7 summarizes major findings of the present study. It also contains over all conclusions. In addition, the scope and direction of the future work are discussed.

CHAPTER 1

INTRODUCTION

1.1 Indium Nitride

Indium Nitride (InN) is one of the members of III-nitrides.¹ InN along with the other nitrides such as GaN and AlN are the focus of intense research because of their exceptional optoelectronic properties.²⁻⁸ III-nitrides possesses the direct band gap spanning from near infra-red (NIR) to deep ultra-violet (UV) region. At room temperature, the band gap of InN, GaN and AlN is 0.75, 3.47 and 6.2 eV, respectively.^{9,10} One can tune direct band gap from NIR to deep UV by varying composition of their ternary alloys such as InGaN, AlGaN, and InAlN.⁹ As a result, numerous optical devices like light emitting diodes (LEDs), and laser diodes (LDs) are developed based on the III-nitrides and their alloys.^{7,8,11,12} The technologically important blue LED is developed based on the InGaN alloy.¹³⁻¹⁵ The 2014 Nobel Prize in physics is awarded to the developers of blue LED for their groundbreaking breakthrough in the field of solid-state lighting. In addition to the unchallenged optical properties, III-nitrides also attracted for their electric properties.⁴ III-nitrides can also be utilized as high power electronic devices because of the wide direct band gap.⁴ The hetero-structures of the III-nitrides (GaN/AlGaN) can act as high electron mobility electron transistors (HEMT) by exploiting their inherent spontaneous and piezoelectric polarization.^{16,17}

InN has been a less studied material as compared to other nitrides because of the difficulties in growth of high-quality crystalline material.¹⁸ However, research interest in InN is not tarnished because of its superior electronic properties such as

high carrier mobility and low effective electron mass ($0.07m_e$).^{10,18,19} As a result, low field mobility of InN can reach up to $10,000 \text{ cm}^2\text{V}^{-1}\text{s}^{-1}$.¹⁹ After a decade-long debate, the band gap of InN has been settled in the NIR region ($\sim 0.75 \text{ eV}$) from 1.9 eV giving rise to its applicability in the near-infrared and terahertz (THz) region.²⁰⁻²⁶ Because of its inherent properties like, high equilibrium pressure of N over InN and low thermal stability, the formation of high-quality InN phase is difficult.^{18,27}

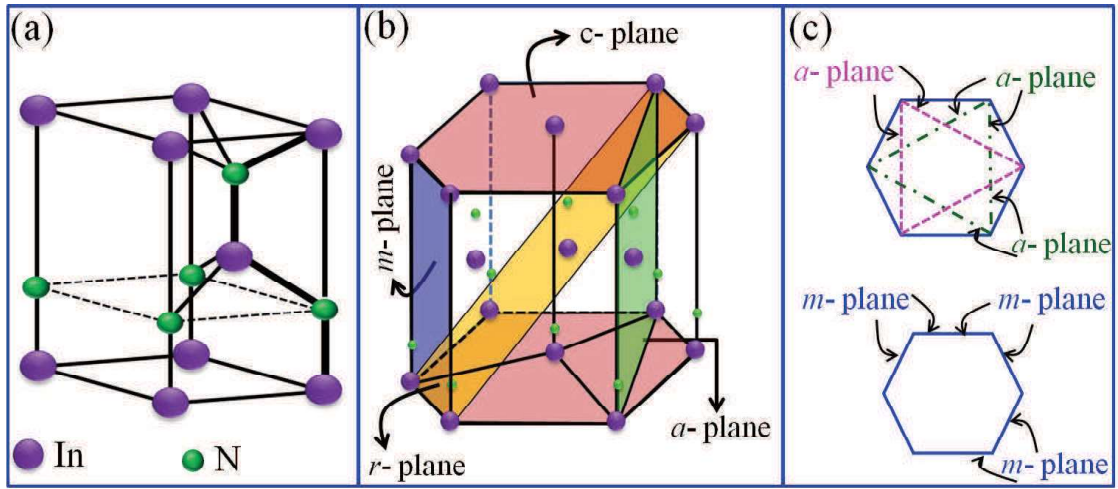


Figure 1.1. (a) Stick and ball representation of unit cell of the *wurtzite* InN structure. (b) Important crystal planes of the wurtzite hexagonal structure. (c) Top view of the crystal planes.

1.1.1 Crystal structure

InN exists in the three crystal structures such as *wurtzite*, *zinc blende* and *rock salt* or *NaCl* structure. Among these structures, *wurtzite* structure is a thermodynamically stable structure at ambient conditions. The *zinc blende* structure of InN and other nitrides is stabilized when the epitaxial growth carried out on $\{011\}$ crystal planes of the cubic structure substrates,¹ such as Si, MgO and GaAs or by ion implantation technique.²⁸ The *rock salt* structure is realized only under high pressure conditions, and the structural phase transition can be induced at 12.5 GPa .¹ The *wurtzite* structures involve two interpenetrated hexagonal unit cells (Fig. 1.1a) with two lattice constants such as a and c . Each unit cell contains six atoms of each type and displaced along the

c -axis by $5c/8$. The *wurtzite* structure has the space group symmetry of $P6_3mc$ (C_{6v}^4). The important crystal planes of the *wurtzite* structure are depicted in the Fig. 1.1b. The *wurtzite* structure does not have the inversion symmetry along the c -axis. Consequently, the basal plane or c -plane is terminated with either group III elemental atoms (0001) or N atoms (000 $\bar{1}$). As a result, the *wurtzite* crystal structure of III-nitrides provides the spontaneous polarization along the c -axis, $\langle 0001 \rangle$. Thus, c -plane has the polar nature. Among the other planes, a -plane (11 $\bar{2}0$) and m -plane (10 $\bar{1}0$) are the non-polar, whereas r -plane (1 $\bar{1}02$) is the semi-polar plane.¹ Top view of these a and m -planes are shown in the Fig. 1.1c. The lattice parameters of the *wurtzite* structures III-nitrides are tabulated in Table 1.1.

Table 1.1. Experimental and calculated lattice parameters of the *wurtzite* structures of AlN, GaN and InN.

| | a (Å) Experimental/Calculated | c (Å) Experimental/Calculated |
|------------|---|------------------------------------|
| AlN | 3.1106 ²⁹ / 3.060 ³⁰ | 7.9795/4.9100 |
| GaN | 3.1890 ³¹ / 3.1620 ³⁰ | 5.1864/5.1420 |
| InN | 3.5380 ³² / 3.5010 ³⁰ | 5.7030/5.669 |

The *zinc blende* structure has a cubic unit cell with the space group of $F\bar{4}3m$ (T_d^2). The position of the atoms within in the unit cell is identical with the diamond structure. The *zinc blende* structure has two interpenetrated face-centred cubic sublattices. These sublattices are displaced along the body diagonal by one-quarter of its length. The structures of the *wurtzite* and *zinc blende* are somewhat similar and yet different. In both cases, each III-atom is coordinated with the four N

atoms and vice versa. The difference in these two structures arises from their stacking sequence along (0001) and (111) planes of the *wurtzite* and *zinc blende* structures, respectively. In case of *wurtzite* structure, the stacking sequence is AaBb along the [0001] direction, whereas in the case of the *zinc blende* structure the stacking sequence is AaBbCc along the [111]. Lowercase and uppercase letters represent the two different kinds of constituents.¹

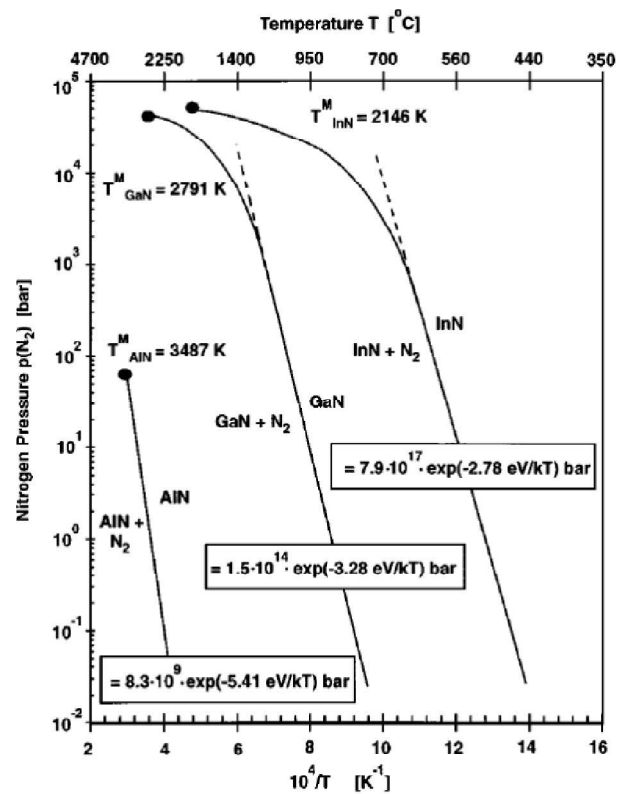


Figure 1.2. Melting points of III-nitrides and equilibrium N_2 pressure over the III-nitrides system from the high pressure experiments and theoretical calculation. *Reprinted with permission from Ref. 33, Copyright © 1996 American Institute of Physics*)

1.1.2 InN: Difficulties in the synthesis

Synthesis of InN phase is difficult because of the thermodynamic properties of its constituent atoms such as In and N_2 .^{18,22,27} High bonding energy of N_2 molecule as compared to the relatively low bonding energy of the InN makes the direct growth very difficult from the constituents (In and N_2).²⁷ As compared to other III-nitrides,

the growth of the InN phase is more difficult because of the equilibrium pressure of N₂ over InN is very high as compared to the AlN and GaN.³³ The equilibrium pressure of N₂ over III-nitrides along the melting point data is shown in Fig. 1.2. In addition, low dissociation temperature (~500 °C) of InN constraints on the growth temperature.¹⁸ As a result, the growth of InN should be carried out at the moderate temperatures (400–650 °C) as compared to those for GaN and AlN. For the growth of InN, most of the time reactive NH₃ gas was used for N source. The low growth temperature shortens the available N atoms, and it adversely affects the quality of the InN phase. Because of these inherent properties, it is very difficult to synthesis high-quality InN phase. Moreover, the large disparity in the atomic radii and electronegative values of N and In further hinders the growth of good quality InN.¹ Because of the low crystalline quality, as-grown InN always exhibits *n*-type conductivity, with unintentional free-electron concentrations as high as 10²¹ cm⁻³.¹⁸

Recently, the crystalline quality of InN phase is enormously improved with controlled growth techniques such as molecular beam epitaxy (MBE) and other techniques like chemical vapour deposition and metal organic vapour phase epitaxy (MOVPE).^{20-26,34-42} The deposition and decomposition temperatures of the InN phase occur in the same range (500–650 °C), and it is comparatively easy to control such conditions with the vapour phase epitaxial technique. As a consequence of this, one fails to find any reports on optical grade InN using the atmospheric pressure chemical vapour deposition (APCVD) technique even though it is a commercially viable technique for large-scale synthesis. Thus, it is inevitable to synthesis InN films and nanostructures using the APCVD technique.

1.1.3 InN nanostructures

As discussed in the previous section, the quality of the InN is low because of the inherent properties such as high equilibrium pressure of the N_2 over InN and low decomposition temperature. InN also suffers from a lack of a native substrate like other III-nitrides.⁴³⁻⁴⁵ Generally, foreign substrates are associated with lattice mismatch because of the difference in the lattice constants and the thermal expansion coefficients. Usually, III-nitrides are grown on sapphire substrate, which has 25% of lattice mismatch with the InN. The substrates like Si and GaAs are also used for the growth of InN with the lattice mismatch of 8% and 11.5%, respectively.¹⁸ Because of the lattice mismatch, the strain is developed in the grown material. However, the developed strain may relax by forming misfit and threading dislocations in the films,⁴³ leading to the degradation of the electronic and optical properties of the material. This phenomenon further reduces the quality of InN phase. In order to reduce the effect of lattice mismatch, usually, InN is grown on sapphire substrates with a buffer layer of GaN or AlN.

Lattice mismatch is the sole reason for the misfit dislocations, and the density of these dislocations can be reduced by restricting the contact area of grown material with the substrate. In this context, InN nanostructures serve as an alternate for the strain-free and defect free InN.⁴⁶ The high surface to volume ratio of the nanostructure, in addition to the single crystalline nature, enhances the ability for lateral elastic relaxation.⁴⁷ As a result, quality of InN phase is enormously increased by growing it as nanostructures.^{26,47-54} Recently, the growth of InN nanostructures is reported with improved quality. Subsequently, properties of InN are started establishing with improved InN phase. The growth of *p*-type InN is extremely difficult because of high

background carrier density and surface electron accumulation. Recently, the growth of *p*-type InN nanorods (NRs) is reported using the Mg doping.^{51, 52} In addition, surface charge properties of InN nanorods are precisely manipulated using the Mg doping.⁵⁰ However, the growth of optical grade InN nanostructures in APCVD technique is of paramount importance because of its commercially viable nature and high growth rate. The quality, morphology and carrier density are strongly dependent on the growth parameters like temperature, growth time, and flow rates of precursors. Thus, it is important to establish growth of InN nanostructures using the APCVD technique and study their properties.

1.1.4 Surface electron accumulation of InN

InN possesses the unique property such as surface electron accumulation (SEA), which is shown to be a universal feature of InN surface.⁵⁵⁻⁵⁹ The origin of the SEA is attributed to the location of the branch point energy (E_{BP}), which is the transition energy level of the donor to acceptor type states. In the case of InN, the E_{BP} is located significantly above the conduction band minima (CBM). Consequently, there can be donor-type surface states in the conduction band. These donor-type surface states discharge their electrons into the conduction band by acquiring a positive charge. In order to compensate this positive charge of the surface states, electrons are accumulated near surface region. Moreover, downward band bending takes place near the surface region because of the positive charge of surface states.⁵⁵⁻⁵⁹ The electrons in the SEA behaves like two-dimensional electron gas (2DEG) which is confined in the direction perpendicular to the surface and free to move along the surface.^{50,57} The sheet carrier density can be tuned using the growth parameters,⁵⁹ as well as external doping.⁵⁰

The presence of In-In adatoms on the surfaces of InN is the physical origin of the SEA. The surface states of In-In adatoms exist above the CBM owing to the narrow band gap of InN. These surface states donate the electron to conduction band acquiring the positive charge. However, the presence of the In-In adatoms at the surface depends on the growth conditions.⁶⁰ The SEA is also observed for the Si-doped InN NRs and the segregation of Si atoms on the surface is reason for SEA.⁵⁰ Such a naturally forming 2DEG on the InN surface provides a system to probe the interesting physics and new applications.

1.2 Optical Properties of InN

There was ambiguity around the fundamental band gap of InN. Earlier, the fundamental band gap was predicted to be in the energy range of the 1.8–2.0 eV.^{10,18,20,21} The band gap was estimated using the absorption studies for the samples grown as polycrystalline nature with a poor-crystalline quality. The photoluminescence (PL) emission from these materials was hardly observed. The single crystal InN films and nanostructures are realized using the improved growth techniques such as MBE and MOVPE. Subsequently, the fundamental band gap of InN is revised, which is significantly smaller than earlier predicted band gap. The revised band gap of InN is reported to be in the range of the 0.6-0.75 eV.²⁰⁻²⁶ The revised band gap of InN opened the applications in THz region. As a consequence of the narrow gap of InN, a strong nonparabolicity of the lowest conduction band prevails.^{10,61} Similar, kind of nonparabolicity is observed for the other narrow bandgap semiconductors such as InAs and InSb. The nonparabolicity is attributed the $\mathbf{k}\cdot\mathbf{p}$ repulsion across the narrow gap between conduction and valence bands. The calculated conduction and valence bands are shown (Fig. 1.3) using the $\mathbf{k}\cdot\mathbf{p}$ model.¹⁰

The observed large band gap of InN can be understood using the Burstein-Moss (BM) shift. In case of the degenerate semiconductors, optical absorption transitions forbidden below the Fermi surface. As a result, the onset of the absorption edge is

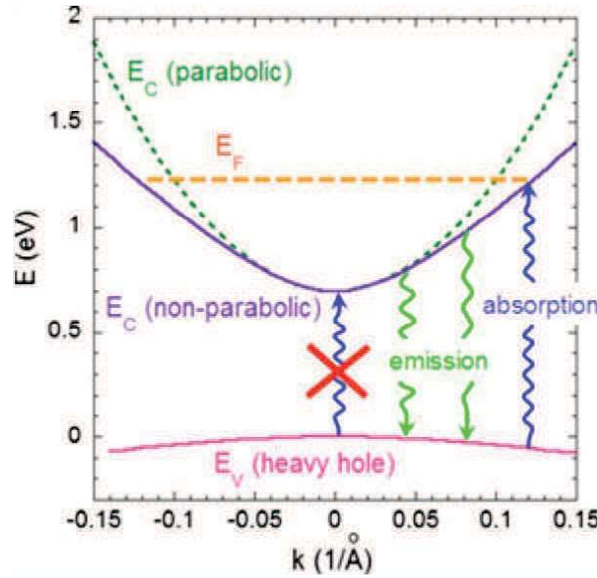


Figure 1.3. Calculated conduction and valence band dispersion of InN using the $k \cdot p$ model. *Reprinted with permission from Ref. 10, Copyright © 2009 American Institute of Physics)*

shifted to higher energy and subsequently overestimates the optical band gap. This phenomenon is called the BM effect. In contrast, in the case of PL, the transitions can be possible from the states below the Fermi level. However, PL emission, in this case, is broadened. The allowed and forbidden optical transitions are depicted in the Fig. 1.3. Because of poor crystal quality, InN is heavily or degenerately doped, and the band gap of InN is overestimated by the absorption studies. The optical absorption edge is dependent on the carrier density, and the relationship between carrier density and BM shift is given as⁶²

$$\Delta_{BM} = \frac{\hbar^2}{2m^*} (3\pi^2 n_e)^{2/3} \dots\dots\dots (1.1)$$

where m^* is the reduced mass of the electron-hole pair, Δ_{BM} is the energy shift from the original band gap and n_e is the carrier density in the system.

The strain in the system also influences the band gap of III-nitrides.⁴³ The major source of residual strain is lattice mismatch as the growth is carried out on a foreign substrate. Till now, there is no study regarding the simultaneous effect of BM shift and strain on the emission properties of InN. Thus, it is important to establish the effect of strain and BM shift on optical properties of InN.

1.3 Vibrational Properties of InN

The III-nitrides are well characterized using inelastic light scattering technique such as Raman spectroscopy. The *wurtzite* InN belongs to the space group $p6_3mc$ (C_{6v}^4) with four atoms in the primitive unit cell. In this structure, each atom occupies the C_{3v} sites. At the zone centre ($q = 0$), group theory predicted eight sets of phonon normal modes and the irreducible representation of these normal modes is given as $\Gamma = 2A_1 + 2E_1 + 2E_2 + 2B_1$.⁶³⁻⁶⁵ One set of $A_1 + E_1$ modes are acoustic phonon modes and while remaining, $A_1 + E_1 + 2E_2 + 2B_1$, are optical phonon modes. Among these, both the A_1 and E_1 phonon modes are IR and Raman active. In contrast to this, the E_2 phonon modes of $E_2(\text{high})$ and $E_2(\text{low})$ are exclusively Raman active. However, the B_1 phonon mode is neither Raman nor IR active and is termed as a forbidden mode. The A_1 and E_1 phonon modes are polar, and these vibrations polarize the unit cell leading to further split into the longitudinal optical ($A_1(\text{LO})$ and $E_1(\text{LO})$) and transverse optical ($A_1(\text{TO})$ and $E_1(\text{TO})$) modes. Consequently, the *wurtzite* phase of InN consists of six Raman active phonon modes namely, $2A_1$, $2E_1$, and $2E_2$ at the zone centre. The basic vibrational motions of atoms correspond to different phonon modes are schematically illustrated in Fig. 1.4. The experimental and calculated optical phonon mode frequencies of the *wurtzite* InN are listed in Table 1.2.

III-nitrides are polar semiconductors and the electric field associated with the LO phonon modes strongly interacts with the free carriers through the Fröhlich interaction, leading to the observation of LO plasmon-phonon coupling modes (LOPCs) in the Raman spectrum.^{41,66} The frequency of the coupled modes is approximated as

$$\omega_{\pm}^2 = \frac{1}{2} \left[(\omega_{LO}^2 + \omega_p^2) \pm \left[(\omega_{LO}^2 + \omega_p^2)^2 + 4\omega_p^2\omega_{LO}^2 \right]^{1/2} \right] \dots\dots\dots (1.2)$$

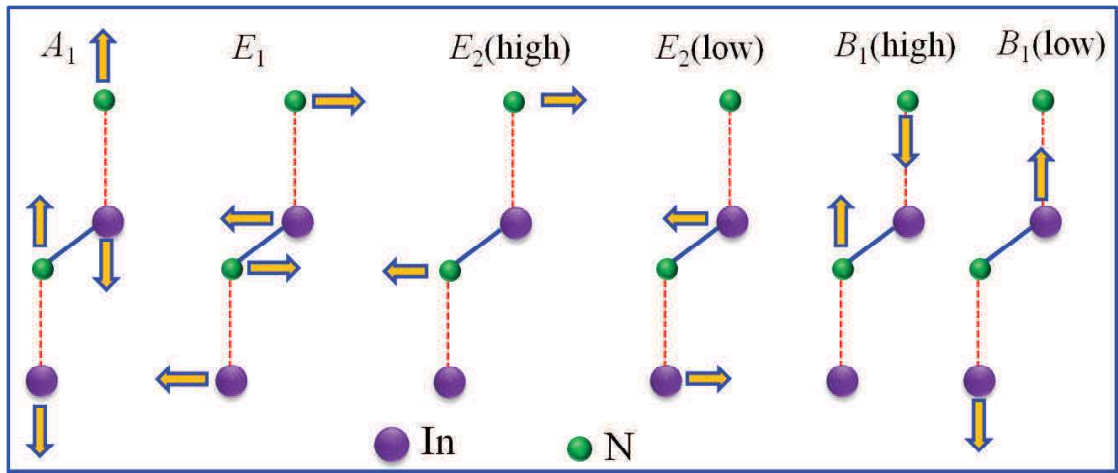


Figure 1.4. Schematic illustration of atomic motions corresponds to different optical phonon modes.

where ω_{LO} and ω_p are the LO phonon mode frequency and plasma frequency of charge carriers, respectively. The ω_+ and ω_- are the low-frequency and high-frequency modes of LOPCs (also known as L_+ and L_-). The plasma frequency is expressed as

$$\omega_p^2 = \frac{4\pi n e^2}{\epsilon^*} \dots\dots\dots (1.3)$$

where ϵ^* is the effective electron mass, ϵ_∞ is the high-frequency dielectric constant and e is the elementary charge. The equation (1.2) is not valid for overdamped plasma oscillations, and spectrum cannot be explained by the ω_{\pm} modes. Using equation (1.2), one can non-destructively estimate the carrier density in the system. However, in some

instants coupled modes are not observed, and interaction of the carrier density with LO phonon mode is manifested as the asymmetric broadening, Fano line shape.

Table 1.2. Experimental and calculated frequencies of symmetry allowed Raman modes.

| | Experimental (cm⁻¹)⁶³ | Calculated (cm⁻¹)⁶⁷ |
|-----------------------------------|--|--|
| <i>E</i>₂(low) | 87 | 93 |
| <i>A</i>₁(TO) | 447 | 443 |
| <i>E</i>₁(TO) | 476 | 470 |
| <i>E</i>₂(high) | 488 | 492 |
| <i>A</i>₁(LO) | 586 | 589 |
| <i>E</i>₁(LO) | 593 | 605 |

The *E*₂(high) phonon mode is the best measure of the strain and crystalline quality of the films. Because of non-polar nature, it is not affected by the carrier density in the material. Depending on the nature of strain in the films, either being compressive or tensile, a shift in the *E*₂(high) phonon mode frequency is observed with respect to strain-free values. A blue shift is observed for the compressive strain, and a red shift is observed for the tensile strain. Moreover, a broadened full width half maximum (FWHM) of the *E*₂(high) phonon mode reveals the possible presence of native defects.⁴³

InN is reported to have the widest phonon band gap and lowest photonic band gap, which prompts its application in hot carrier solar cells.^{10,68} Thus, it is inevitable to study the phonon structure of InN with the excitation in the IR as well as in the visible region for developing InN based devices.

1.4 Work Function of InN

The work function of semiconductors is dependent on the doping level.⁶⁹ However, the reports on the work function values of InN are scarce.⁷⁰⁻⁷² Moreover, it is well known that InN possesses the SEA close to the surface region because of its narrow band gap. As a result of the SEA, the downward band bending is observed close to the surface region. Because of downward surface band bending, the two-dimensional electron gas (2DEG) is formed along the surface.^{50,73-75} Thus, it is very important to study the work function values of the InN because of its degenerate nature and possession of the surface electron accumulation. The work function can be measured by various techniques such as Kelvin probe (KP), photoelectron spectroscopy (PES), and from the analysis of electron beam induced current (EBIC) in scanning electron microscopy (SEM). In KP method, contact potential difference (CPD) is measured by nullifying the current between the two periodically vibrating parallel plate capacitors. The measured CPD in KP method corresponds to the whole area of the sample. The spatial resolution of the KP method can be enormously increased using the Kelvin probe force microscopy (KPFM), where it exploits the atomic force microscopy (AFM) technique.

1.5 InN as Plasmonic Material

In the last decade, surface plasmons, categorized as plasmonics, have been widely studied because of their potentiality in the miniaturization of photonic devices and other widespread applications in multiple fields such as biological and chemical sensing.⁷⁶⁻⁷⁸ A surface plasmon is collective oscillations of conduction band electrons excited by electromagnetic (EM) waves. Surface plasmons have two fundamental

excitations, *i.e.* localized surface plasmon resonance (LSPR) and propagating surface plasmon polaritons (SPPs). The SPPs are propagating EM waves along the metal and dielectric interface, which are confined along the interface region. The most spectacular application of the SPP is its ability to confine and guide the light in the sub-wavelength structures by overcoming the Abbe diffraction limit.^{78,79} So far, the most studied plasmonic materials are Au and Ag, which show LSPR phenomenon in the infrared (IR) to the visible region.⁷⁷ Even though the major studied plasmonic materials are noble metals, the use of noble metal nanoparticles has its limitations because of the plasmonic losses. In this context, low-loss plasmonic metamaterials and semiconductors with sufficiently high carrier density can be the alternative to metallic nanostructures in the field of plasmonics.⁸⁰ In the case of semiconductors, the LSPR frequency can be achieved up to near IR range. Moreover, plasmonics based on metals is static in nature. The carrier concentration, and subsequently the plasmonic properties of semiconductors, can be readily altered with doping in semiconductors. Thus, the semiconductor nanoparticles with varying carrier concentration can offer dynamic plasmonic nature.⁸¹ Till now, metal chalcogenides and metal oxides have been studied for their plasmonic properties.⁸² Recently, 2D plasmons in graphene generated much curiosity because of their THz resonance frequency.⁸³ In the case of 3D plasmonic material, the plasmon frequency (ω_p) is scaled with the square root of the carrier density of the system (Equation (1.3)). On the other hand, ω_p depends on the in-plane wave vector as well as areal carrier density in the case of the 2D plasmonics.⁸⁴⁻⁸⁶ The plasmon frequency of 2DEGs is given as

$$\omega_p^2 = \frac{n_s e^2}{*} \frac{q}{\epsilon_1 + \epsilon_2 \coth(qd)} \dots\dots\dots (1.4)$$

where n_s is the areal carrier density of 2DEG, m^* the effective mass of electrons, ϵ_1 and ϵ_2 are the dielectric constants of the substrate and surrounding media, q is the in-plane wave vector and d is the thickness of the 2D electron system.

As discussed earlier, InN is a degenerate semiconductor, and it possesses the 2DEG. Thus, it is worth probing the plasmonic properties of 2DEG corresponding to InN SEA and its possible applications in the field of plasmonics.

1.6 Objective and Overview of the Thesis

The prime objective of the thesis is to grow the high-quality InN nanostructure using the commercially viable APCVD technique by overcoming the inherent difficulties in the synthesis of InN phase and study their optical and vibrational properties. Especially, it is important to establish the simultaneous effect of BM shift and residual strain on the emission properties of InN. In addition, it is important to study the excitation-dependent phonon properties of InN because of its applications in hot carrier solar cells. Moreover, the thesis aims to explore the plasmonic properties of InN nanostructures. In this context, it is worth probe the effect of 2DEG corresponding to the SEA in plasmonic properties of InN and its applications in the surface-enhanced Raman spectroscopy (SERS). The present thesis comprises the seven chapters, and a brief discussion about each chapter is provided below.

Chapter 1 introduces the InN and its basic properties. Here, difficulty in the synthesis and the role of crystal quality in optical properties are elaborated. The unique property of InN such as SEA and its physical origin is discussed. The controversy surrounding the optical band gap is elaborately discussed. The reason for the earlier predicted large band gap is explained based on the BM effect. Because of polar and degenerate nature of InN, the vibrational properties and its coupling modes

are elaborated. The possibility of the degenerate InN as the plasmonic material and plasmonic nature 2DEG of the SEA is also discussed.

Chapter 2 details the development of the APCVD technique for the growth of the InN nanostructures. Additionally, setting up of the important characterization techniques such as near-field scanning optical microscopy (NSOM) for studying the near-field optical properties of InN nanostructures and KPFM for the surface potential measurements of InN nanostructures are discussed.

Chapter 3 presents the growth of InN nanostructures using the In_2O_3 powder as source material. Evaluation of the nanorod growth and optimization of the nanorod growth using the growth temperature, growth time and flow rates of precursors are discussed. Morphology of the nanostructures solely depends on the growth temperature, evolving from quantum dot sized nanoparticles to NRs. It is found that 630 °C is the threshold temperature for nanorod growth. The change in the morphology of nanostructures is explained based on the nucleation and the growth rates during the phase formation. In addition, high optical quality InN films were grown on a sapphire substrate using the APCVD technique in the temperature range of 560–650 °C. The self-catalytic approach was adopted to overcome the nucleation barrier for depositing InN films. The simultaneous effect of strain and the BM energy shift on the optical properties of InN films is studied using Raman and PL spectroscopy. The existence of compressive strain in all films is revealed by Raman spectroscopic analysis and is found to relax with increasing growth temperature. A large blue shift of the band gap of InN (1.2 eV) is observed as a collective result of compressive strain in films as well as a BM shift.

In Chapter 4, vibrational properties of InN nanostructures grown via self-seeded catalytic approach are discussed. Samples with increasing carrier densities are grown, with the help of increasing growth temperature, to understand the role of carrier density in the optical phonon structure. It was found that nanostructures grown ≥ 620 °C possess the SEA. The presence of the SEA was confirmed by Raman studies, which was further corroborated by PL and ultra-violet photoelectron spectroscopy (UPS) studies. The frequency of 2DEG corresponding to the SEA was found to be in the THz region of $54\text{--}60\text{ cm}^{-1}$ ($\sim 1.6\text{--}1.8$ THz). A Raman forbidden mode of $B_1(\text{high})$, because of the possible breakdown of selection rules in the near-resonance conditions, is invoked for the first time. The intensity and frequency of this mode strongly depend on the carrier concentration in the sample. In off-resonance conditions, the $A_1(\text{LO})$ mode for the sample with higher carrier concentration is dominated by Fano interference rather than plasmon-phonon coupling.

In Chapter 5, the plasmonic properties of InN nanostructures are explored using the NSOM technique. The role of 2DEG corresponding to the SEA in the generation SPPs is discussed. The periodic fringes are observed in the near-field scanning optical microscopic images of InN nanostructures. The observed fringes are attributed to the interference of propagated and back-reflected SPPs. The observation of SPPs is solely attributed to the 2DEG corresponding to the SEA of InN. Additionally, SERS activity of the InN nanostructures is explored using the Rhodamine 6G (R6G) molecules. SERS enhancement is observed for the InN nanostructures which possess SEA. The enhancement factor of four orders was calculated with the assumption of monolayer coverage of analyte molecule. SERS enhancement of InN nanostructures is attributed to the 2D plasmonic nature of InN

nanostructures invoking SEA, rather than the contributions from 3D surface plasmon resonance and chemical interaction.

Chapter 6 details the work function measurements of InN nanostructures grown via plasma assisted molecular beam epitaxy (PAMBE). CPD is measured using the KPFM to estimate the work function of the InN NRs. In order to avoid the influence of the surface adsorbed species, KPFM measurements were carried out at high vacuum condition of $\sim 7.5 \times 10^{-7}$ mbar. The work function of InN NRs is found to depend on the size of NRs. Size-dependent work function of the InN NRs is attributed to the variation in the downward surface band bending caused by SEA rather than a change in the Fermi level position.

Chapter 7 summarizes major findings of the present study. It also contains overall conclusions. In addition, the scope and direction of the future work are discussed.

1.7 References

1. H. Morkoç, *Handbook of nitride semiconductors and devices, Materials Properties, Physics and Growth* (John Wiley & Sons, **2009**).
2. P. J. Pauzauskie and P. Yang, *Mater. Today* **2006**, 9, 36.
3. A. Khan, K. Balakrishnan and T. Katona, *Nat. Photonics* **2008**, 2, 77.
4. R. Quay, *Gallium nitride electronics*. (Springer Science & Business Media, **2008**).
5. H. Yoshida, Y. Yamashita, M. Kuwabara and H. Kan, *Nat. Photonics* **2008**, 2, 551.
6. R. Yan, D. Gargas and P. Yang, *Nat. Photonics* **2009**, 3, 569.
7. S. Zhao, H. P. Nguyen, M. G. Kibria and Z. Mi, *Prog. Quantum Electron.* **2015**, 44, 14.
8. A. Patsha, S. Dhara, S. Chattopadhyay, K.-H. Chen and L.-C. Chen, *J. Mater. NanoScience* **2018**, 5, 1.
9. T. Kuykendall, P. Ulrich, S. Aloni and P. Yang, *Nat. Mater.* **2007**, 6, 951.
10. J. Wu, *J. Appl. Phys.* **2009**, 106, 5.

11. S. P. DenBaars, D. Feezell, K. Kelchner, S. Pimputkar, C.-C. Pan, C.-C. Yen, S. Tanaka, Y. Zhao, N. Pfaff and R. Farrell, *Acta Mater.* **2013**, 61, 945.
12. Q. Wang, A. Connie, H. Nguyen, M. Kibria, S. Zhao, S. Sharif, I. Shih and Z. Mi, *Nanotechnology* **2013**, 24, 345201.
13. S. Nakamura, M. Senoh and T. Mukai, *Appl. Phys. Lett.* **1993**, 62, 2390.
14. S. Nakamura, T. Mukai and M. Senoh, *Appl. Phys. Lett.* **1994**, 64, 1687.
15. S. Nakamura, *Science* **1998**, 281, 956.
16. O. Ambacher, J. Smart, J. Shealy, N. Weimann, K. Chu, M. Murphy, W. Schaff, L. Eastman, R. Dimitrov and L. Wittmer, *J. Appl. Phys.* **1999**, 85, 3222.
17. O. Ambacher, B. Foutz, J. Smart, J. Shealy, N. Weimann, K. Chu, M. Murphy, A. Sierakowski, W. Schaff and L. Eastman, *J. Appl. Phys.* **2000**, 87, 334.
18. A. G. Bhuiyan, A. Hashimoto and A. Yamamoto, *J. Appl. Phys.* **2003**, 94, 2779.
19. V. M. Polyakov and F. Schwierz, *Appl. Phys. Lett.* **2006**, 88, 032101.
20. V. Y. Davydov, A. Klochikhin, R. Seisyan, V. Emtsev, S. Ivanov, F. Bechstedt, J. Furthmüller, H. Harima, A. Mudryi and J. Aderhold, *Phys. status solidi (b)* **2002**, 229, 1.
21. T. Matsuoka, H. Okamoto, M. Nakao, H. Harima and E. Kurimoto, *Appl. Phys. Lett.* **2002**, 81, 1246.
22. M.-S. Hu, W.-M. Wang, T. T. Chen, L.-S. Hong, C.-W. Chen, C.-C. Chen, Y.-F. Chen, K.-H. Chen and L.-C. Chen, *Adv. Funct. Mater.* **2006**, 16, 537.
23. C.-H. Shen, H.-Y. Chen, H.-W. Lin, S. Gwo, A. Klochikhin and V. Y. Davydov, *Appl. Phys. Lett.* **2006**, 88, 253104.
24. T. Stoica, R. J. Meijers, R. Calarco, T. Richter, E. Sutter and H. Lüth, *Nano Lett.* **2006**, 6, 1541.
25. J. Segura-Ruiz, N. Garro, A. Cantarero, C. Denker, J. Malindretos and A. Rizzi, *Phys. Rev. B* **2009**, 79, 115305.
26. S. Zhao, Z. Mi, M. Kibria, Q. Li and G. Wang, *Phys. Rev. B* **2012**, 85, 245313.
27. A. K. Murali, A. D. Barve and S. H. Risbud, *Mater. Sci. and Eng.: B* **2002**, 96, 111.
28. S. Dhara, A. Datta, C. Wu, Z. Lan, K. Chen, Y. Wang, C. Hsu, C. Shen, L. Chen and C. C. Chen, *Appl. Phys. Lett.* **2004**, 84, 5473.
29. M. Tanaka, S. Nakahata, K. Sogabe, H. Nakata and M. Tobioka, *Jpn. J. Appl. Phys.* **1997**, 36, L1062.
30. K. Kim, W. R. Lambrecht and B. Segall, *Phys. Rev. B* **1996**, 53, 16310.
31. M. Leszczynski, H. Teisseyre, T. Suski, I. Grzegory, M. Bockowski, J. Jun, S. Porowski, K. Pakula, J. Baranowski and C. Foxon, *Appl. Phys. Lett.* **1996**, 69, 73.

32. W. Paszkowicz, *Powder Diffr.* **1999**, 14, 258.
33. O. Ambacher, M. Brandt, R. Dimitrov, T. Metzger, M. Stutzmann, R. Fischer, A. Miehr, A. Bergmaier and G. Dollinger, *J. Vac. Sci. Technol., B: Microelectron. Nanometer Struct.-- Process., Meas., Phenom.* **1996**, 14, 3532.
34. M. Tangi, J. Kuyyalil and S. Shivaprasad, *J. Appl. Phys.* **2013**, 114, 153501.
35. J. Kamimura, K. Kishino and A. Kikuchi, *J. Appl. Phys.* **2015**, 117, 084314.
36. M. A. Mayer, S. Choi, O. Bierwagen, H. M. Smith III, E. E. Haller, J. S. Speck and W. Walukiewicz, *J. Appl. Phys.* **2011**, 110, 123707.
37. K. Wang, T. Araki, M. Takeuchi, E. Yoon and Y. Nanishi, *Appl. Phys. Lett.* **2014**, 104, 032108.
38. J. Kamimura, M. Ramsteiner, U. Jahn, C.-Y. J. Lu, A. Kikuchi, K. Kishino and H. Riechert, *J. Phys. D: Appl. Phys.* **2016**, 49, 155106.
39. V. Darakchieva, P. Paskov, E. Valcheva, T. Paskova, B. Monemar, M. Schubert, H. Lu and W. Schaff, *Appl. Phys. Lett.* **2004**, 84, 3636.
40. F. Demangeot, C. Piquier, J. Frandon, M. Gaio, O. Briot, B. Maleyre, S. Ruffenach and B. Gil, *Phys. Rev. B* **2005**, 71, 104305.
41. J. Thakur, D. Haddad, V. Naik, R. Naik, G. Auner, H. Lu and W. Schaff, *Phys. Rev. B* **2005**, 71, 115203.
42. R. Cuscó, J. Ibáñez, E. Alarcón-Lladó, L. Artús, T. Yamaguchi and Y. Nanishi, *Phys. Rev. B* **2009**, 79, 155210.
43. C. Kisielowski, J. Krüger, S. Ruvimov, T. Suski, J. Ager III, E. Jones, Z. Liliental-Weber, M. Rubin, E. Weber and M. Bremser, *Phys. Rev. B* **1996**, 54, 17745.
44. F. Demangeot, J. Frandon, C. Piquier, M. Caumont, O. Briot, B. Maleyre, S. Clur-Ruffenach and B. Gil, *Phys. Rev. B* **2003**, 68, 245308.
45. Q. Yan, P. Rinke, M. Scheffler and C. G. Van de Walle, *Appl. Phys. Lett.* **2009**, 95, 121111.
46. S. D. Hersee, X. Sun and X. Wang, *Nano Lett.* **2006**, 6, 1808.
47. E. Schäfer-Nolte, T. Stoica, T. Gotschke, F. Limbach, E. Sutter, P. Sutter, D. Grützmacher and R. Calarco, *Nanotechnology* **2010**, 21, 315702.
48. J. Segura-Ruiz, A. Molina-Sanchez, N. Garro, A. García-Cristóbal, A. Cantarero, F. Iikawa, C. Denker, J. Malindretos and A. Rizzi, *Phys. Rev. B* **2010**, 82, 125319.
49. G. Wu, G. Du, F. Gao, H. Wang, C. Shen and W. Li, *J. Phys. D: Appl. Phys.* **2012**, 45, 215102.
50. S. Zhao, S. Fatholouloumi, K. Bevan, D. Liu, M. G. Kibria, Q. Li, G. Wang, H. Guo and Z. Mi, *Nano Lett.* **2012**, 12, 2877.

51. S. Zhao, B. Le, D. Liu, X. Liu, M. Kibria, T. Szkopek, H. Guo and Z. Mi, *Nano Lett.* **2013**, 13, 5509.
52. S. Zhao, X. Liu and Z. Mi, *Appl. Phys. Lett.* **2013**, 103, 203113.
53. D. Bayerl and E. Kioupakis, *Nano Lett.* **2014**, 14, 3709.
54. E. B. Quddus, A. Wilson, R. A. Webb and G. Koley, *Nanoscale* **2014**, 6, 1166.
55. I. Mahboob, T. Veal, C. McConville, H. Lu and W. Schaff, *Phys. Rev. Lett.* **2004**, 92, 036804.
56. I. Mahboob, T. Veal, L. Piper, C. McConville, H. Lu, W. Schaff, J. Furthmüller and F. Bechstedt, *Phys. Rev. B* **2004**, 69, 201307.
57. L. Colakerol, T. D. Veal, H.-K. Jeong, L. Plucinski, A. DeMasi, T. Learmonth, P.-A. Glans, S. Wang, Y. Zhang and L. Piper, *Phys. Rev. Lett.* **2006**, 97, 237601.
58. P. King, T. D. Veal, C. F. McConville, F. Fuchs, J. Furthmüller, F. Bechstedt, P. Schley, R. Goldhahn, J. Schörmann and D. As, *Appl. Phys. Lett.* **2007**, 91, 092101.
59. W. Linhart, J. Chai, R. J. Morris, M. Dowsett, C. F. McConville, S. Durbin and T. D. Veal, *Phys. Rev. Lett.* **2012**, 109, 247605.
60. C. G. Van de Walle and D. Segev, *J. Appl. Phys.* **2007**, 101, 081704.
61. J. Wu, W. Walukiewicz, W. Shan, K. Yu, J. Ager III, E. Haller, H. Lu and W. J. Schaff, *Phys. Rev. B* **2002**, 66, 201403.
62. A. Walsh, J. L. Da Silva and S.-H. Wei, *Phys. Rev. B* **2008**, 78, 075211.
63. V. Y. Davydov, V. V. Emtsev, I. N. Goncharuk, A. N. Smirnov, V. D. Petrikov, V. V. Mamutin, V. A. Vekshin, S. V. Ivanov, M. B. Smirnov and T. Inushima, *Appl. Phys. Lett.* **1999**, 75, 3297.
64. H. Hiroshi, *J. Phys: Condens. Matter* **2002**, 14, R967.
65. X. Wang, S.-B. Che, Y. Ishitani and A. Yoshikawa, *Appl. Phys. Lett.* **2006**, 89, 171907.
66. S. Lazi, J. Gallardo, J. Calleja, F. Agulló-Rueda, J. Grandal, M. Sánchez-García, E. Calleja, E. Luna and A. Trampert, *Phys. Rev. B* **2007**, 76, 205319.
67. G. Kaczmarczyk, A. Kaschner, S. Reich, A. Hoffmann, C. Thomsen, D. As, A. Lima, D. Schikora, K. Lischka and R. Averbeck, *Appl. Phys. Lett.* **2000**, 76, 2122.
68. G. Conibeer, D. König, M. Green and J. Guillemoles, *Thin Solid Films* **2008**, 516, 6948.
69. M. Noe, C. er, M. o' o le d . . ic r i e, *Appl. Phys. Lett.* **1991**, 58, 2921.
70. C. Shih, N. Chen, P. Chang and K. Liu, *J. Cryst. Growth* **2005**, 281, 328.
71. C.-F. Shih, N. Chen and C. Tseng, *Thin Solid Films* **2008**, 516, 5016.

72. W. Liu, Y. Luo, Y. Sang, J. Bian, Y. Zhao, Y. Liu and F. Qin, *Mater. Lett.* **2013**, 95, 135.
73. L. Colakerol, T. Veal, H.-K. Jeong, L. Plucinski, A. DeMasi, T. Learmonth, P.-A. Glans, S. Wang, Y. Zhang, L. Piper, P. Jefferson, A. Fedorov, T.-C. Chen, T. Moustakas, C. McConville and K. Smith, *Phys. Rev. Lett.* **2006**, 97, 237601.
74. K. K. Madapu and S. Dhara, *Appl. Phys. A* **2018**, 124, 435.
75. K. K. Madapu, A. Sivadasan, M. Baral and S. Dhara, *Nanotechnology* **2018**, 29, 275707.
76. W. L. Barnes, A. Dereux and T. W. Ebbesen, *Nature* **2003**, 424, 824.
77. S. A. Maier, *Plasmonics: fundamentals and applications*. (Springer Science & Business Media, **2007**).
78. D. K. Gramotnev and S. I. Bozhevolnyi, *Nat. Photonics* **2010**, 4, 83.
79. J. A. Schuller, E. S. Barnard, W. Cai, Y. C. Jun, J. S. White and M. L. Brongersma, *Nat. Mater.* **2010**, 9, 193.
80. A. Boltasseva and H. A. Atwater, *Science* **2011**, 331, 290.
81. J. A. Fauchaux, A. L. Stanton and P. K. Jain, *J. Phys. Chem. Lett.* **2014**, 5, 976.
82. T. M. Mattox, X. Ye, K. Manthiram, P. J. Schuck, A. P. Alivisatos and J. J. Urban, *Adv. Mater.* **2015**, 27, 5830.
83. A. Grigorenko, M. Polini and K. Novoselov, *Nat. Photonics* **2012**, 6, 749.
84. S. Allen Jr, D. Tsui and R. Logan, *Phys. Rev. Lett.* **1977**, 38, 980.
85. D. Olego, A. Pinczuk, A. Gossard and W. Wiegmann, *Phys. Rev. B* **1982**, 25, 7867.
86. G. Fasol, N. Mestres, H. Hughes, A. Fischer and K. Ploog, *Phys. Rev. Lett.* **1986**, 56, 2517.

CHAPTER 2

GROWTH AND EXPERIMENTAL TECHNIQUES

In this chapter, the techniques used for the growth and characterization of InN nanostructures are discussed. As the InN nanostructures were grown using the atmospheric pressure chemical vapour deposition (APCVD), the chemical vapour deposition (CVD) technique is elaborately discussed. In addition, a brief discussion is added on the plasma-assisted molecular beam epitaxy (PAMBE) technique, which is used for the growth of undoped and doped InN nanorods. In the characterization section, the near-field scanning optical microscopy (NSOM), Kelvin probe force microscopy (KPFM) and UV photoemission spectroscopy techniques are explicitly discussed. In addition, a short discussion is devoted to the basic characterization techniques such as Raman spectroscopy, photoluminescence (PL) spectroscopy, scanning electron microscopy (SEM), transmission electron microscopy (TEM) and atomic force microscopy (AFM).

2.1 Growth Techniques

2.1.1 Atmospheric pressure chemical vapour deposition

Practically, the CVD is defined as the deposition of solid materials at high temperature using the chemical reactions. Usually, the deposited material in the CVD technique is crystalline as the growth occurs in the thermodynamic equilibrium condition. The CVD method can be classified and categorized based on different parameters. The main parameters are pressure, wall and substrate temperatures, nature of precursor, and gas flow state and activation process. If the chamber is maintained at atmospheric pressure during the deposition, the deposition method is called the APCVD. However,

CVD is significantly different from the physical vapour deposition (PVD) techniques such as sputtering and thermal evaporation. The CVD is relied on the chemical reactions between precursor materials at high temperature, whereas PVD deposits the pre-existed material. In addition, CVD has the several advantages over the PVD. The CVD is a non-line of site process and because of this reason conformality in deposited films is improved as compared to that by the PVD, which is a line of site process. Because of the flexibility in the precursor materials, 70% of the elements in the periodic table can be deposited using the CVD technique. The stoichiometry, crystal structure, surface morphology, and growth rate can be readily varied in CVD technique using the growth parameters. The CVD is industrially viable technique because of large area synthesis possibilities.¹ The following important sequences are involved in the deposition of materials in the CVD technique.

- Mass transport of the reactants close to the substrate.
- Adsorption of reactants or intermediates on the substrate. Intermediates forms via homogeneous chemical reactions.
- Deposition of material with surface migration and the heterogeneous reaction of reactants.
- Formation of by-product species.
- Diffusion of by-product species to the bulk gas and transport of by-product gaseous species away from the substrate (exhaust).

The CVD system had five major components. Details of each component, used in the present experimental setup, are provided below.

i) Energy source (Horizontal tube furnace)

The energy source is required to initiate the chemical reactions in the chamber. In the present study, the horizontal tube furnace was used for the energy source. The important parameters of the tube furnace are listed below.

- Make: Zhengzhou Brother Furnace (Model No. XD-1200NT)
- Maximum temperature: 1400 °C
- Operating temperature: 500-1300 °C
- Temperature Controlling: PID automatic control via SCR (Silicon Controlled Rectifier) power control with phase angle fired, current limiting resistor
- Temperature accuracy: ± 1 °C
- Heating element: SiC heating elements
- Thermocouple: S type

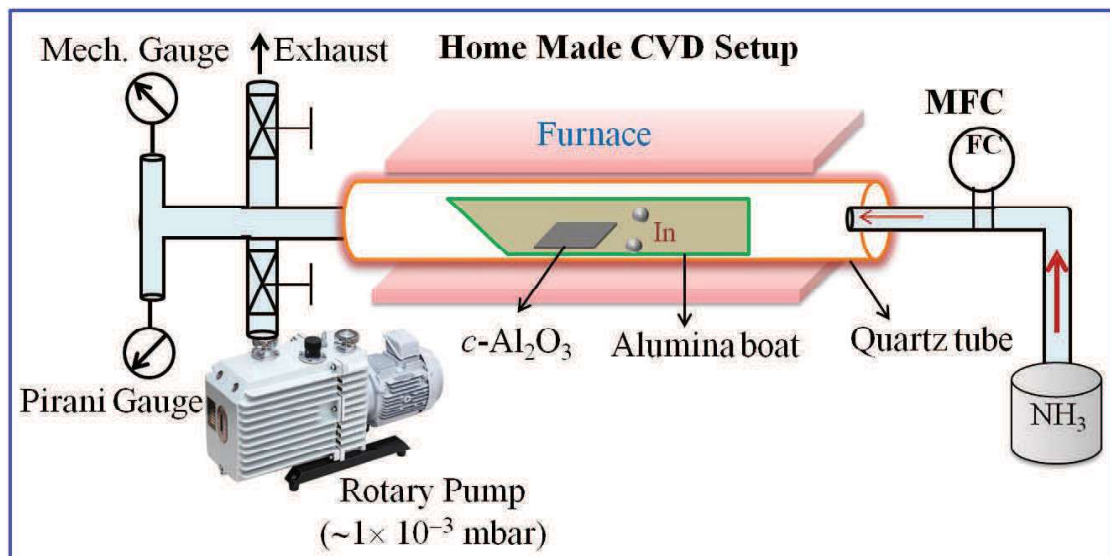


Figure 2.1. Schematic of the home made APCVD experimental setup.

ii) Reaction chamber

The quartz tube was used as the reaction chamber. The dimensions of the quartz tube were 2.7 cm (diameter), ~110 cm (length) and ~1 cm (thickness).

iii) Vacuum system

The reaction chamber (schematic in Fig. 2.1) was pre-evacuated before introducing the reactant gases. The chamber was evacuated up to $\sim 1 \times 10^{-3}$ mbar using the mechanical rotary pump. The chamber pressure was measured using the Pirani gauge and mechanical gauge for the low and high-pressure regimes, respectively.

iv) Delivery and control system

It is very important to transport the precursors to the reaction chamber. The delivery system also includes the transport of the carrier and diluting gases along with the precursors. The selection criteria of the delivery system are dependent on the nature of the precursors such as gas, liquid, and solid. Delivery and control are easy for the gaseous precursors. However, liquid and solids are vaporized before transporting to the reaction chamber. In the present study, reactive NH_3 (99.999%) was used as the precursor gas for N source. The gas flow was controlled using the mass flow controller (MFC, GFC 17, AALBORG). InN was synthesized with two different source materials such as In_2O_3 (99.999%) powder and metallic In (99.999%, Sigma Aldrich) shots. In the former case, InN was synthesized via nitridation of In_2O_3 powder using the reactive NH_3 gas in the temperature range 550-700 °C and the prepared InN phase was also in the powder form. In case of later, InN was deposited on the sapphire substrate using metallic In shots as the source material in the temperature range of 570-650 °C (Fig. 2.1). The source materials, In_2O_3 and In shots, were pre-loaded along with the substrate in both cases.²

v) Removal of the by-products

The conversion efficiency of the CVD system is less than 10%. In the wake of this, the proper exhaust system is required for the safe handling of the un-reacted precursor gases, by-products, and intermediate gases. Ammonia (NH_3) is a hazardous gas. In addition, NH_3 is highly corrosive in the presence of the moisture. Adequate precautions were taken in order to handle the NH_3 gas and its by-products. Stainless steel and Teflon pipes were used for the pressurized piping lines and other lines, respectively. Teflon tape was used on all the joints for the effective leak proof connections. The chamber and exhaust line was separated by the ball valve which had a stainless steel internal surface. The chamber pressure was measured using diaphragm gauge which was compatible with the NH_3 gas. The un-reacted NH_3 and its by-product were forced to flow through NH_3 absorption system (scrubber) such as water solution before entering into the atmosphere. In the present experimental setup, adequate precautions were taken to handle the by-products.

2.1.2 Plasma-assisted molecular beam epitaxy

The MBE is one of the PVD techniques for the growth of epitaxial films. The deposition was carried out under an ultra-high vacuum environment ($\sim 10^{-9}$ mbar). As a result, the transport of the materials from the source to the substrate occurred in the molecular flow regime. The atomically clean substrate surface was possible because of the oil-free and ultra-high vacuum environment. These conditions enabled the control of the composition and doping of deposited film at monolayer level. In addition, the low growth temperature and low deposition rates ensured the abruptness and control over interfaces. The source materials were heated in the effusion cells or Knudsen's cells and which were transported towards the substrates in the form of

atoms or cluster of atoms.³ The reflection high energy electron diffraction (RHEED) is standard instrumentation associated with the MBE technique. The real-time analysis of diffraction pattern provided the information about the native oxide on the substrate, surface crystal structure, surface reconstructions, surface morphology and growth rates. The surface analytical instruments were also incorporated in the deposition chamber for the in-situ measurements of the physical and chemical properties of grown films. The typical surface analytical instruments are Auger electron spectrometer or X-ray photoelectron spectroscopy (XPS). Schematic of the MBE chamber is shown in Fig. 2.2.³

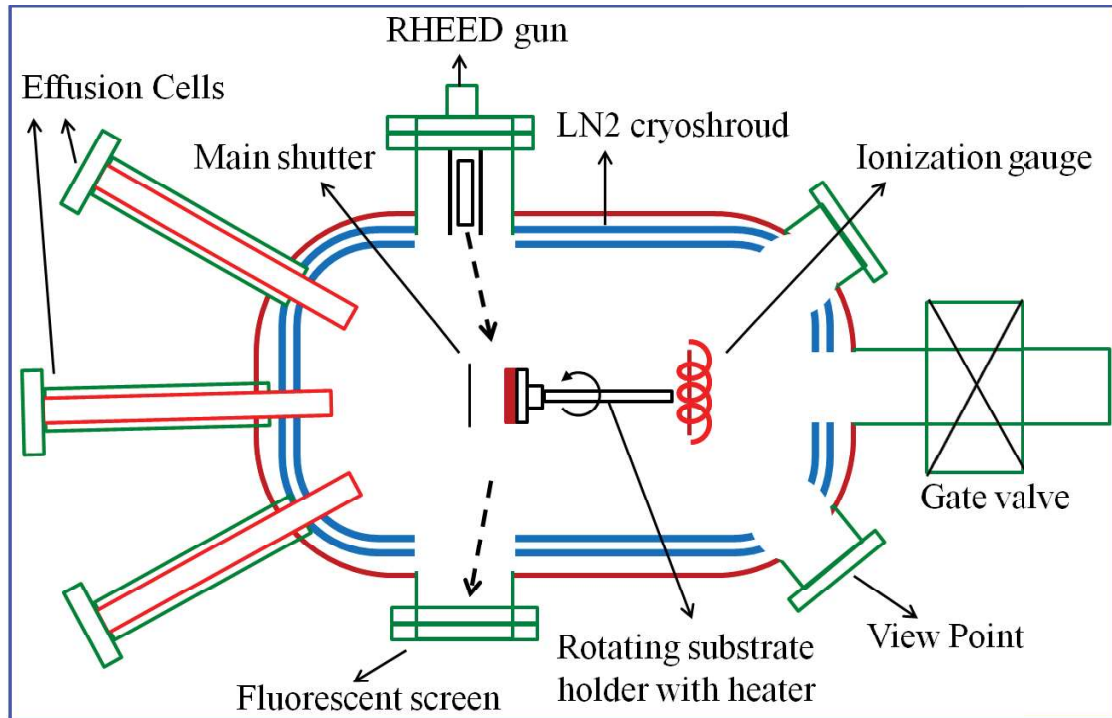


Figure 2.2. Schematic of a typical cross-sectional view of MBE chamber.

Usually, InN is grown as a heavily doped *n*-type material because of its inherent properties. Moreover, it possesses the surface electron accumulation (SEA). As a result, *p*-type doping and control over the *n*-type doping are difficult. Recently, *p*-type doping is achieved using the MBE techniques. In the present thesis, undoped

and *n*-type doped InN nanorods were grown using the PAMBE.⁴ The growth was carried out under N rich conditions to obtain the columnar morphology. In-situ cleaned crystalline Si (111) was used as the substrate, and the substrate temperature was maintained at 475 °C. Atomic N source is generated using the radio-frequency plasma with nitrogen flux of 4.0 sccm. Si flux is used for the *n*-type doping with the beam equivalent pressure $\sim 5.8 \times 10^{-8}$ mbar. The In effusion cell temperature is maintained at 817 °C. The growth time for the undoped and *n*-type doped InN nanorods was 2 and 4 hr, respectively.⁴

2.2. Near-Field Light-Matter Interaction

2.2.1 Near-field scanning optical microscopy

The conventional optical microscopy is limited by the diffraction limit. The maximum spatial resolution that can be achieved by an optical microscope is $\geq \lambda/2$ with a highest available numerical aperture (N.A.) (1.3-1.4), where λ is the wavelength of light. In other words, spatial resolution achieved by the typical green light is not more than the 250 nm. Nanotechnology, however, with its spectacular applications and fundamental research interest, deals with the nanostructures which are having the feature sizes ≤ 100 nm. As a consequence, conventional optical microscopy is handicapped to resolve these nanostructures.⁵ Moreover, the inherent capabilities of optical microscopy like spectroscopic information, temporal resolution, and polarization capabilities cannot be utilized because of the diffraction limit, and subsequently, vast information obtained from the optical microscopy cannot be retrieved.⁵

The limitation of the optical microscopy can be understood from Abbe's diffraction theory. The light spot formed by the objective lens impose the limitations

on the spatial resolution achieved by the optical microscopy. At the focal point, lens system forms symmetric concentric rings with central maxima, Airy disk pattern. According to Abbe, the distance between the center of the central maxima and the first node of the diffraction is given by

$$d = \frac{0.61\lambda}{n \sin \theta} \dots\dots\dots (2.1)$$

where λ is the free-space wavelength, n is the refractive index of the medium and θ is the light converging angle of the objective lens. According to the Rayleigh criterion, the minimum resolvable distance between the two objects must be equal to the distance given by the equation 2.1. Thus, the maximum achievable spatial resolution is $\sim \lambda/2$ with the N.A. ($n \sin \theta$) of 1.3-1.4.^{5,6}

The NSOM is a prominent technique for improving the spatial resolution of optical microscopy by breaking the diffraction limit.^{5, 6} The modern-day NSOM is

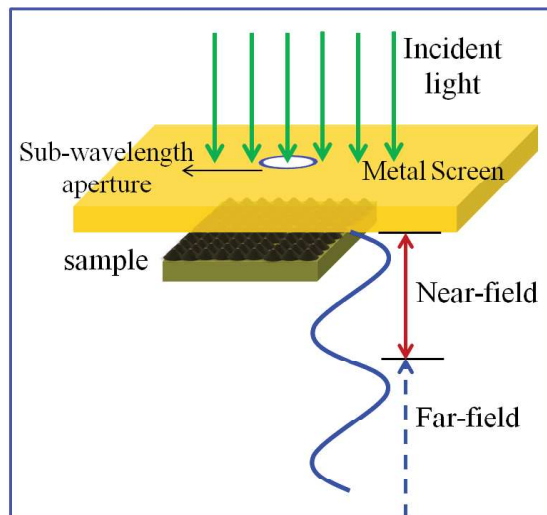


Figure 2.3. Schematic of Syngé proposal to overcome the diffraction limit.

developed based on the visionary papers published by the Syngé in the early 20th century.⁷⁻⁹ Syngé proposed that the diffraction limit can be overcome by using the aperture size of less than the wavelength of the excitation. The schematic of the

original idea of Synge is shown in the Fig. 2.3. The high-intensity light illuminates the backside of the opaque metal screen with aperture size less than the wavelength of the illuminated light. The illuminated light is confined in the aperture, which is used to image the sample surface point by point in the proximity of sample surface. In this case, the spatial resolution is dependent on the size of aperture rather than the wavelength of the illuminated light. The experimental condition to get the high spatial resolution is that the aperture must be scanned in a near-field regime. The NSOM technique utilizes the AFM feedback mechanism to control the distance between the aperture and sample surface in a near-field regime.^{5,10-12}

The role of NSOM in improving the spatial resolution can be understood using the equation 2.1. It shows that the spatial resolution can be increased by reducing the wavelength of the light. In other words, using the shorter wavelength electromagnetic (EM) waves such as UV light one can improve the resolution. However, optical microscopy has the limitations to use the UV light. In another way, the wavelength of light can be reduced using the evanescent waves. The evanescent wave is imaginary or non-propagating EM wave which is confined to the surface.¹¹ The propagating EM wave is given by

$$\mathbf{E} = E_0 \exp[i(\mathbf{k} \cdot \mathbf{r} - \omega t)] \dots\dots\dots (2.2)$$

where \mathbf{k} is the wave vector of the propagating EM wave and is given by,

$$\mathbf{k} = k_x \mathbf{i} + k_y \mathbf{j} + k_z \mathbf{k} \dots\dots\dots (2.3)$$

The magnitude of the \mathbf{k} is given by $|\mathbf{k}| = 2\pi/\lambda$. Since the evanescent wave is imaginary, the evanescent wave is given by

$$\mathbf{E} = E_0 \exp[i(k_x \mathbf{i} + k_y \mathbf{j} - \omega t)] \exp[-k_z \mathbf{k}] \dots\dots\dots (2.4)$$

Equation 2.4 indicates that the evanescent wave is exponentially decaying in the z -direction. As a consequence, the evanescent wave is a non-propagating wave and existed only in the near-field region. The magnitude of the \mathbf{k} vector of the propagating EM wave is given by,

$$k^2 = k_{\parallel}^2 + k_z^2 \dots\dots\dots (2.5)$$

where $k_{\parallel}^2 = k^2 + k_y^2$. If light passes through the aperture of size 'a', k_{\parallel} and k_z describes the EM wave properties of the field just after the aperture which constitutes the plane and evanescent waves. The magnitude of the k_z has the two possibilities depending on the magnitude of the k_{\parallel} . Thus, the k_z has the two following solutions,

$$k_z = \sqrt{k^2 - k_{\parallel}^2} \text{ for } k_{\parallel} \leq k, \text{ and } k_z = i\sqrt{k^2 - k_{\parallel}^2} \text{ for } k_{\parallel} > k.$$

As the aperture size is 'a', the angular spectrum of the aperture contains the k_{\parallel} which falls in the range of $2\pi/a$ to $2\pi/\lambda$. For $k_{\parallel} = 2\pi/a$, the amplitude of the k_z is given by,

$$k_z = \sqrt{\left(\frac{2\pi}{\lambda}\right)^2 - \left(\frac{2\pi}{a}\right)^2} \dots\dots\dots (2.6).$$

when ' $a < \lambda$ ', and the propagating vector in the z -direction is imaginary. In other words, the field transmitted through this aperture is an evanescent field. As a result, the EM field is strongly confined to the aperture and has the non-propagative nature. Because of the strong confinement of light, the NSOM technique provides the improved resolution.¹¹ In case of $a > \lambda$, the $k_{\parallel} \sim 0$ and $k_z \sim k$, the transmitted wave is a propagating wave.

The near-field light-matter interaction of InN nanostructures was studied with the aid of NSOM technique (MultiView 4000, Nanonics Imaging Ltd., Israel). In the

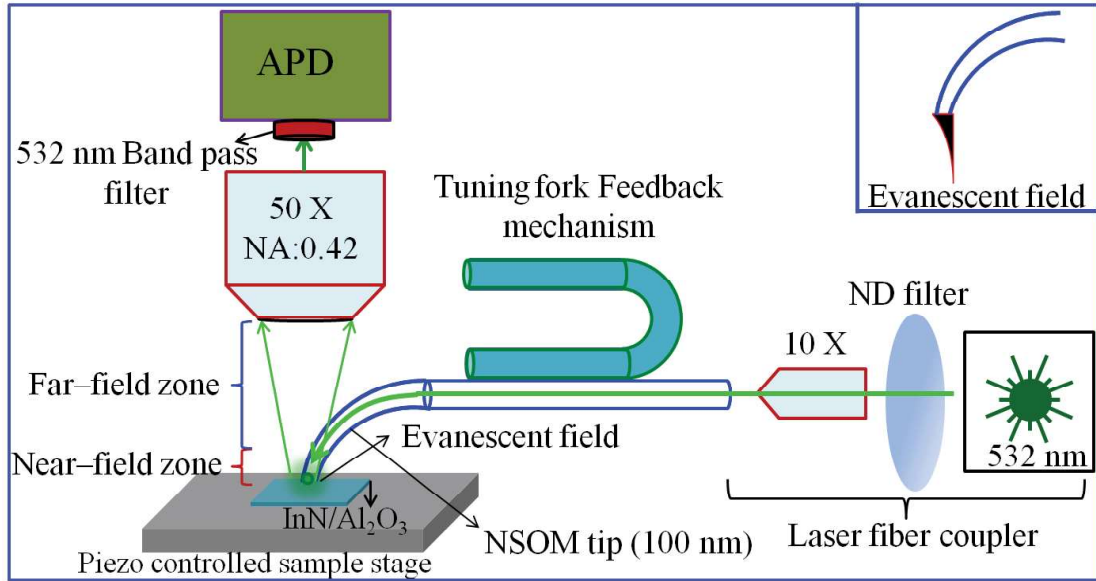


Figure 2.4. Schematic of NSOM technique used for the study of near-field optical properties of InN nanostructures. Inset of the figure shows the schematic of the evanescent field at the end of the aperture.

present study, NSOM imaging was carried out using the apertured probe in the reflection mode (schematic in Fig. 2.4). In this particular study, 532 nm laser excitation and a ~100 nm Cr-Au metal coated apertured tip was used in the near-field. The MultiView 4000 uses normal force tuning fork technology with a high Q factor and phase feedback to control the probe to sample separation. Scattered light was collected with confocal detection using 50 X objective lens of the N.A. ~ 0.42. The collected light was directed towards the avalanche photodiode (APD) single photon counter (Sens-Tech, Model DM0087C). The AFM scanning was carried in the intermittent (tapping) mode with the raster scanning using the fast and slow axis movements. In the present report, all scans were carried out with a scan rate of 20 ms/point and the integration time of the photon counter was 20 ms. Thus, the simultaneous topographic image was also acquired along with the intensity distribution of surface plasmon scattering. As a result of slow scan rates of 20 ms/point, artifacts could be observed in AFM and NSOM images because of the

sample drift. However, the scan rate was limited by the integration time of the photon counter. The scan rate should be greater than or equal to the photon counter integration time for a meaningful measurement.

2.2.2 Surface plasmon polaritons: Role of NSOM

The surface plasmon polaritons (SPPs) are propagating EM waves along the metal and dielectric interface, which are confined along the interface region.¹³⁻¹⁵ The SPPs are evanescent in nature, which means that the field strength is decreased exponentially perpendicular to the surface. The most spectacular application of SPP is its ability to confine and guide the light in the sub-wavelength structures by overcoming the Abbe's diffraction limit. The propagation of light in sub-wavelength nanostructures is reported to be utilized for the realization of nano-phonic devices as well as optical nano-connectors. However, it is well known that the propagating EM waves and the SPPs always have momentum (k) mismatch in their dispersion curves (Equation 2.7). The SPP dispersion relation is given by,¹³

$$k_{SPP} = k \sqrt{\frac{\epsilon_1 \epsilon_2}{\epsilon_1 + \epsilon_2}} \dots\dots\dots (2.7)$$

Here, k_{SPP} is the wave vector of SPP; k is the wave vector of the free-space propagating EM wave; ϵ_1 and ϵ_2 are the dielectric functions of conducting medium and surrounding medium (non-absorbing), respectively. In the present study, in order to excite the SPPs, apertured NSOM probe is used to overcome the momentum mismatch. The light passing through the sub-wavelength aperture possesses higher spatial frequencies, required to excite SPPs, which are not present in the propagating light. Higher spatial frequencies at the aperture are the consequences of confinement of light in the sub-wavelength aperture, which emit the combination of the evanescent

and propagating waves. The range of spatial frequencies ($1/a$ to $1/\lambda$), available at the aperture, depends on the size of the aperture (a) and distance from it.

2.3 Work Function Measurements: Kelvin Probe Force Microscopy

The work function of semiconductors is dependent on the doping level. The work function can be measured by various techniques such as Kelvin probe (KP), photoelectron spectroscopy (PES), and from the analysis of electron beam induced current (EBIC) in scanning electron microscopy (SEM). The KP method measures the contact potential difference (CPD) between the sample and conducting probe which is dependent on the work function of the sample and conducting probe.¹⁶⁻¹⁸ However, CPD is strongly dependent on the various surface parameters such as adsorption layers, oxide layers, and surface contamination.¹⁶ In KP method, CPD is measured by nullifying the current between the two periodically vibrating parallel plate capacitor. The measured CPD in KP method corresponds to the whole area of the sample. The spatial resolution of the KP method can be enormously increased using the KPFM, where it exploits the AFM technique. The KPFM measures the CPD between the conducting AFM tip and the sample surface, and is expressed by,¹⁸

$$CPD(V) = \frac{\phi_{tip} - \phi_s}{-e} \dots\dots\dots (2.8)$$

where ϕ_{tip} and ϕ_s are the work functions of the tip and sample, respectively; e is the elementary charge. The generation of CPD and subsequent development of electrical force between the tip and sample is schematically depicted in the Fig. 2.5a. When the sample and tip is electrically connected, marked as step (2), the charge transfer takes place because of the difference in the Fermi level (E_F) position. As a consequence, the vacuum level is misaligned with the generation of the CPD between sample and tip.

Because of the charged surface, there is an electrical force between the sample and tip along with the van der Waals forces. This electrical force can be nullified using the external bias, which is equal to the V_{CPD} . Subsequently, the work function values are estimated by measuring the CPD values.

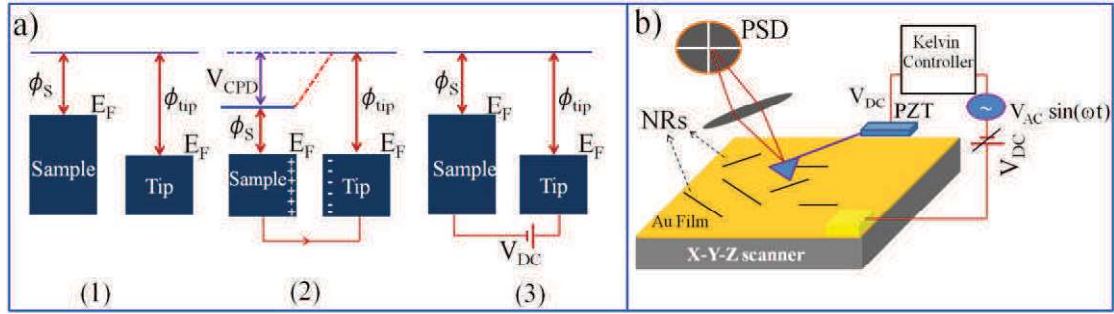


Figure 2.5. a) Schematic band diagram illustrating the principle of KPFM technique. b) Schematic of an experimental technique of KPFM.

The KPFM technique measures the work function by applying the *ac* voltage (V_{ac}) and *dc* voltage (V_{dc}) to the conducting AFM tip. It is assumed that the tip and the sample behave as the capacitor. The V_{ac} generates the oscillating electrical force (F_{EF}) between tip and sample, whereas V_{dc} nullifies F_{EF} caused by the CPD. The F_{EF} between the capacitor plates is given by,

$$F_{EF} = -\frac{\partial U}{\partial z} \dots\dots\dots (2.9)$$

where U is the potential energy and the z is the distance between the tip and sample surface. The F_{EF} can be written as,

$$F_{EF} = -\frac{1}{2} \frac{\partial C}{\partial z} (\Delta V)^2 \dots\dots\dots (2.10)$$

where $\partial C/\partial z$ is the gradient capacitance and the ΔV is the difference in the V_{CPD} and applied voltage. The F_{EF} further can be written as,

$$F_{EF} = -\frac{1}{2} \frac{\partial C}{\partial z} [(V_{CPD} \pm V_{dc}) + V_{ac} \sin(\omega t)]^2 \dots\dots\dots (2.11)$$

The \pm symbol depends on the whether V_{dc} is applied to the sample (+) or AFM tip (-).

The equation 2.11 can be simplified with the following three terms:

$$F_{DC} = -\frac{1}{2} \frac{\partial C}{\partial z} (V_{CPD} - V_{dc})^2 \dots\dots\dots (2.12)$$

$$F_{\omega} = -\frac{\partial C}{\partial z} (V_{CPD} - V_{dc}) V_{ac} \sin(\omega t) \dots\dots\dots (2.13)$$

$$F_{2\omega} = \frac{1}{4} \frac{\partial C}{\partial z} V_{ac}^2 [\cos(2\omega t) - 1] \dots\dots\dots (2.14)$$

A static deflection in the AFM is caused by the F_{DC} . The F_{EF} components can be effectively measured at ω and 2ω by a lock-in amplifier (LIA).¹⁸ As the F_{ω} term is linearly varied with the $V_{CPD} - V_{dc}$, it can be used to measure the V_{CPD} . The electrical force becomes zero when V_{dc} is equal to the V_{CPD} .

The Kelvin measurements were carried out using single pass KPFM technique (MultiView 4000, Nanonics Imaging Ltd., Israel). Two LIA's were employed to get the simultaneous topography and CPD measurements. First LIA was used for the topography measurements, whereas the second LIA was used to measure the electrical force. This electric force was feed to Kelvin controller where it was nullified with an applied dc voltage, which is equal to the CPD. In the present study, Pt/Ir coated Si cantilever tip with a resonance frequency in the range of 36-98 kHz was used for the KPFM measurements. The work function of the tip was calibrated using electron beam evaporated Au film, and the work function of the Pt/Ir tip was estimated as 4.95 eV. The schematic of the experimental setup is shown in Fig. 2.5b. The KPFM studies were carried out at high vacuum ($\sim 7.5 \times 10^{-7}$ mbar) with the help of an ion pump in order to avoid the effect of surface adsorbents.

2.4 Surface Electron Accumulation: UV Photoemission Spectroscopy

The working principle of UV photoemission spectroscopy (UPS) is similar to the X-ray photoemission spectroscopy (XPS). The major difference between these two techniques is the energy of the photons utilized for the ejection of electrons. In the case of UPS, UV light is employed to eject the electrons from the solid surface. Usually, rare gas discharge spectral lines are used as the source of UV light. The commonly used spectral lines are He-I and He-II, and their line energies are 21.22 eV and 40.82 eV, respectively. In contrast to this, XPS employs the very high energy X-ray photons to eject the electrons. The Al K_{α} line (1486.6 eV) is the most commonly used X-ray source in XPS measurements. These techniques have a difference in spectral resolution. Usually, the specified spectral resolution of the UPS and XPS are 1 meV and 1 eV, respectively. In addition, the energy of the photoelectrons emitted in the UPS falls in the low energy region. As a result, the collected photoelectrons must be originated from the depth of 5 Å from the surface. In the case of XPS, the collected electrons can originate from the depth of 40 Å from the surface. As a result, the UPS is more surface sensitive than XPS.¹⁹

The electrons are ejected from an atom when a high-intensity EM wave strikes it showing photoelectric effect. The kinetic energy ($E_{K.E}$) of photoelectrons is dependent on the energy of the incident photons ($h\nu$) and threshold energy (E_0) of material (Equation 2.15).

$$E_{K.E} = h\nu - E_0 \dots\dots\dots (2.15)$$

The peaks in the energy spectrum of the photoemitted electrons correspond to the binding energy of core-level electrons. The binding energy (E_B) of the core level electrons is given by,

$$E_B = h\nu - E_{K.E} - W \dots\dots\dots (2.16)$$

where W is the work function which depends on the spectrometer and the material of interest.

The existence of SEA can be analyzed using the valence band spectra (VBS).²⁰⁻²² From VBS one can estimate the position of the E_F with respect to the valence band maximum.²³ In the present study, VBS were recorded using a PHOIBOS 150 hemispherical analyzer with a monochromatic He-I source (21.218 eV). During the experiment, the vacuum inside the analysis chamber was 8×10^{-11} mbar. Samples were sputtered in situ by Ar^+ with beam energy of 500 eV for different duration of times depending on the sample.

2.5 Other Characterization Techniques

In addition to the above-mentioned techniques, basic characterization techniques were also utilized to study the structural and morphological properties of InN nanostructures. The brief description of techniques used in the present thesis is given below.

2.5.1 Raman and photoluminescence spectroscopy

III-nitrides are well characterized using the inelastic light scattering experiments. Raman spectroscopy (Renishaw, inVia)) was extensively used in the present thesis to study the vibrational properties. Raman studies were carried out in the backscattering geometry. The scattered light was monochromatized using 1800 gr/mm, 2400 gr/mm and 3000 gr/mm grating. The monochromatized light was collected using the thermoelectric cooled charge-coupled device (CCD) detector. An objective lens of 100X with an N.A. of 0.90 was used for all Raman measurements. Variation of the

sample temperature was carried out using a liquid N₂ cooled low-temperature stage (Linkam T95, UK). The temperature was varied in the range of 80–373 K. For the low-temperature measurements, long working distance 50X lens was used. The behavior of the phonon structure is explored in the near and off-resonance conditions. For this purpose, different laser sources were used with the wavelengths of 785, 514.5, and 488 nm.

The photoluminescence (PL) spectra were also collected in the backscattering geometry with the same system (Renishaw, inVia). The PL was acquired with two laser excitations of 514.5 and 785 nm. The PL spectra excited with 514.5 nm laser were collected using a CCD detector through 1800 gr/mm grating. The PL spectra in the NIR region were excited with the 785 nm laser, and the luminescence was collected using the InGaAs detector with a 600 gr/mm grating as a monochromator. The 20X objective lens was used for NIR PL measurements.

To avoid the laser heating, Raman measurements were carried out with a low laser power of 3 mW. However, the SERS measurements were carried out with even less laser power of 3 μ W. The spectral resolution of the Raman measurement using 3000 gr/mm grating and 514.5 nm excitation was 0.5 cm^{-1} . Near infra-red (NIR) PL was collected with a spectral resolution of 1 meV.

2.5.2 Morphological studies and structural analysis

The morphological studies of the grown material were carried out using two different techniques such as field-emission scanning electron microscopy (FESEM; Zeiss, SUPRA 55) and AFM (Mutiview 4000, Nanonics). The MultiView 4000 uses the normal force tuning fork technology with a high Q factor and phase feedback to allow control of the probe to sample separation. Tuning forks in normal force mode with

phase or amplitude feedback permit high performance and ease operation for AFM imaging.

Structural properties of the grown material were carried out using X-ray diffraction (XRD, Brucker, D8 Discover) and high-resolution transmission electron microscopy (HRTEM; Libra 200 Zeiss) along with the selected area electron diffraction (SAED) analyses. In addition, elemental analysis was carried out using energy dispersive X-ray spectroscopy (EDS), which was equipped with the FESEM and HRTEM techniques.

2.6 Conclusion

Present chapter details the development of the APCVD technique for the growth of InN nanostructures. PAMBE technique is also discussed in the growth techniques section. In addition, important characterization techniques such as NSOM and KPFM for studying the near-field optical properties and the CPD measurements of InN nanostructures, respectively, are elaborately discussed. A short discussion is added on the UPS in characterization techniques, as it is used for the study of SEA properties of InN nanostructures. Finally, a brief discussion is devoted for the details of basic characterization techniques such as Raman spectroscopy, PL spectroscopy, SEM, TEM and AFM.

2.7 References

1. X.-T. Yan and Y. Xu, *Chemical vapour deposition: an integrated engineering design for advanced materials*. (Springer Science & Business Media, **2010**).
2. K. K. Madapu, S. Dhara, S. Amirthapandian, S. Polaki and A. Tyagi, *J. Phys. Chem. C* **2013**, 117, 21930.
3. K. S. Harsha, *Principles of vapor deposition of thin films*. (Elsevier, **2005**).

4. T. Gotschke, E. Schäfer-Nolte, R. Caterino, F. Limbach, T. Stoica, E. Sutter, K. Jeganathan and R. Cialenco, *Nanotechnology* **2011**, 22, 125704.
5. R. C. Dunn, *Chem. Rev.* **1999**, 99, 2891.
6. L. Novotny and B. Hecht, *Principles of nano-optics*. (Cambridge university press, **2012**).
7. E. Synge, *Philos. Mag.* **1928**, 6, 356.
8. E. H. Synge, *Philos. Mag.* **1931**, 11, 65.
9. E. H. Synge, *Philos. Mag.* **1932**, 13, 297.
10. A. Lewis, M. Isaacson, A. Harootunian and A. Muray, *Ultramicroscopy* **1984**, 13, 227.
11. E. Betzig and J. K. Trautman, *Science* **1992**, 257, 189.
12. B. Hecht, B. Sick, U. P. Wild, V. Deckert, R. Zenobi, O. J. Martin and D. W. Pohl, *J. Phys. Chem. C* **2000**, 112, 7761.
13. S. A. Maier, *Plasmonics: fundamentals and applications*. (Springer Science & Business Media, **2007**).
14. S. Kawata, Y. Inouye and P. Verma, *Nat. Photonics* **2009**, 3, 388.
15. D. K. Gramotnev and S. I. Bozhevolnyi, *Nat. Photonics* **2010**, 4, 83.
16. M. Nonnenmacher, M. o'Boyle and H. K. Wickramasinghe, *Appl. Phys. Lett.* **1991**, 58, 2921.
17. Y. Rosenwaks, R. Shikler, T. Glatzel and S. Sadewasser, *Phys. Rev. B* **2004**, 70, 085320.
18. W. Melitz, J. Shen, A. C. Kummel and S. Lee, *Surf. Sci. Rep.* **2011**, 66, 1.
19. P. Y. Yu and M. Cardona, *Fundamentals of semiconductors: physics and materials properties*. (Springer, **1996**).
20. C.-L. Wu, H.-M. Lee, C.-T. Kuo, C.-H. Chen and S. Gwo, *Phys. Rev. Lett.* **2008**, 101, 106803.
21. W. Linhart, J. Chai, R. Morris, M. Dowsett, C. McConville, S. Durbin and T. Veal, *Phys. Rev. Lett.* **2012**, 109, 247605.
22. S. Zhao, S. Fatholouloumi, K. Bevan, D. Liu, M. G. Kibria, Q. Li, G. Wang, H. Guo and Z. Mi, *Nano Lett.* **2012**, 12, 2877.
23. S. A. Chambers, T. Droubay, T. C. Kaspar and M. Gutowski, *J. Vac. Sci. Technol., B: Microelectron. Nanometer Struct.--Process., Meas., Phenom.* **2004**, 22, 2205.

CHAPTER 3

GROWTH OF InN NANOSTRUCTURES AND FILMS

3.1 Introduction

InN has superior electronic properties like high mobility and drift velocity as compared to other semiconductor materials because of its low effective electron mass.¹⁻³ Despite its attractive properties, it is a less studied material as compared to other nitrides because of the difficulty in the synthesis of high-quality material. The difficulty in synthesis of high crystalline InN arises because of its inherent properties like low dissociation temperature and high equilibrium pressure of N over InN.^{1,4,5} The deposition and decomposition temperatures of the InN phase occur in the same range (500–650 °C) and it is comparatively easy to control such conditions with the vapour phase epitaxial techniques. As a result, one fails to find any reports on optical grade InN with the atmospheric pressure chemical vapour deposition (APCVD) technique even though it is a commercially viable technique for large-scale synthesis. III-nitrides along with the InN suffered from huge dislocation density in thin films because of the lack of native substrates.^{1,6} As a result, the crystalline quality of these materials further reduces which renders the degradation in optical emission properties. Nevertheless, nanostructures, especially nanowires, alleviate the strain and dislocation effects because of their effective strain relaxation in the presence of a high surface-to-volume ratio.^{7,8} Thus, it is inevitable to synthesis InN films and nanostructures using the APCVD technique because of its commercial viability. However, it is essential to establish the growth mechanism to overcome the nucleation barrier of the InN in APCVD technique and study its optical properties.

This chapter discusses the two prominent approaches for the growth of InN in APCVD technique by overcoming its inherent difficulties. The growth of InN is subdivided into the two parts based on the source material and nature of grown InN phase. In the first part, the growth of a large amount of InN nanostructures in different morphologies is discussed. The growth is carried out via a nearly homogeneous nucleation growth mechanism without using any substrate for the dislocation-free growth. The growth mechanism of nanorods (NRs) is established by varying the growth parameters in close steps such as temperature, time and gas flow rate. The crystallographic structural analysis is adapted to establish a growth mechanism for the temperature dependent evolution of morphology in these nanostructures from quantum dots (QDs) to one-dimensional NRs. In the second part, the successful deposition of InN film on the sapphire substrate is reported using the self-catalytic approach to overcome the difficulties in the synthesis of InN. The effects of growth temperature on the strain and carrier density of the InN films are studied by analyzing the phonon modes using Raman spectroscopy. Subsequently, the simultaneous effect of the residual strain and Burstein-Moss (BM) shift on optical emission properties are studied using photoluminescence (PL) spectroscopy.

3.2 Growth of InN Nanostructures and Nanorods Using In₂O₃

A customized CVD setup with a horizontal tube furnace was used to perform the growth of InN nanostructures via a catalyst-free vapour-solid (VS) mechanism.^{9,10} The growth of InN nanostructures was carried out by the nitridation of In₂O₃ powder (purity 99.999%, Sigma Aldrich) using reactive ultra high pure NH₃ (99.999%) gas in the temperature range of 550-700 °C. A 40 mg of In₂O₃ powder was kept in a ceramic (Al₂O₃) boat as source and was transferred to a 25 mm diameter quartz tube, which

was pre-evacuated to the base pressure of $\sim 10^{-3}$ mbar using the mechanical rotary pump. The temperature of the furnace was increased at a rate of 20 °C per minute. Reactive NH₃ gas was introduced at a temperature of 400 °C with constant flow rates. After the reaction, the furnace was cooled to room temperature under an NH₃ atmosphere.

3.2.1 Morphological and structural studies

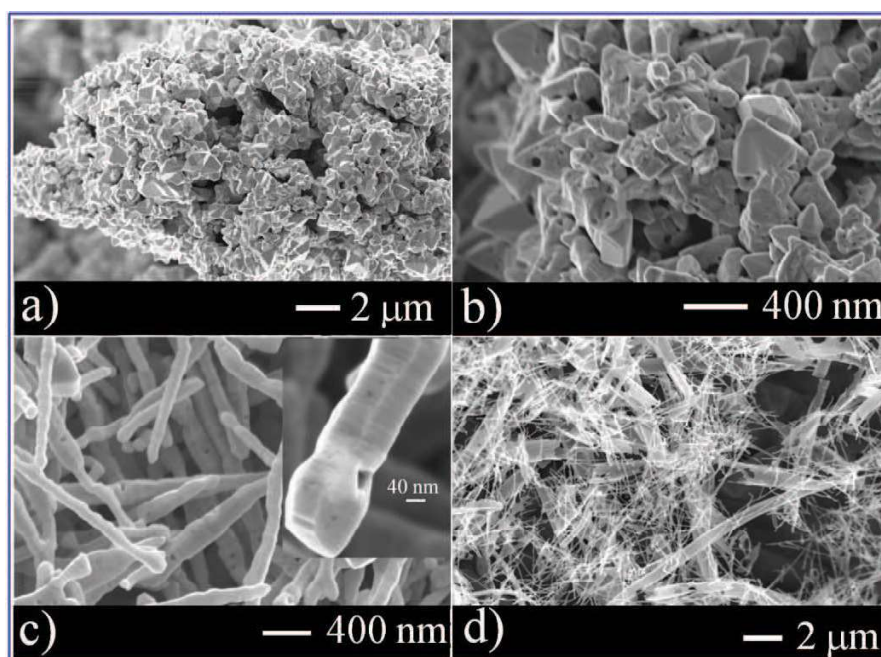


Figure 3.1. Morphology of InN nanostructures grown at different temperatures a) 550, b) 600, c) 650 and d) 700 °C.

The growth of nanostructures was carried out in the temperature range of 550–700 °C with a step of 50 °C for 4 hr each at atmospheric pressure with a NH₃ flow rate of 100 sccm. Morphological features of grown material are depicted in the FESEM (FESEM; Zeiss, SUPRA 55) images (Fig. 3.1). It is found that the morphology of InN nanostructures is strongly dependent on the growth temperature. The multi-faceted nanoparticles were grown at the temperatures of 550 °C (Fig. 3.1a) and 600 °C (Fig. 3.1b). The morphology of nanostructures was changed to NRs as the growth

temperature was increased to 650 °C (Fig. 3.1c). The diameter of these NRs was found to be ~100 nm and the length was up to several micrometers. The presence of micro-tubular and NR structures were observed for the material grown at 700 °C (Fig. 3.1d).¹⁰

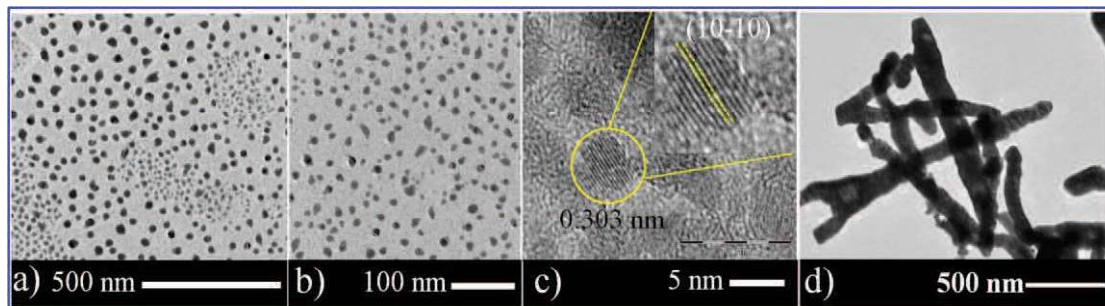


Figure 3.2. Low and high-resolution TEM images of nanostructures grown at 550 and 650 °C. (a)–(c) The size distribution of nanoparticles grown at 550 °C. d) Low magnification image of NRs grown at 650 °C.

Figure 3.2 shows the typical TEM (HRTEM; Libra 200 Zeiss) images of nanostructures grown at 550 and 650 °C. Samples grown at 550 °C were comprised of nanoparticles with a size less than 8 nm. However, large-sized particles were also observed in the FESEM studies (Figs. 3.1a and 3.1b). In addition, the HRTEM image of nanoparticles is provided in Fig. 3.2c. The exciton Bohr radius of InN is reported to be ~8 nm.¹¹ However, in the literature InN nanoparticles below 30 nm are also considered as QDs.^{12,13} The measured lattice spacing of the QD is 0.303 nm, which corresponds to d spacing of the (10–10) plane of wurtzite InN (inset of Fig.3.2c). In addition, the TEM image of NRs grown at 650 °C is shown in Fig. 3.2d. The contrast variation in the TEM image of NR is attributed to the variation of thicknesses along the NRs rather than extended defects. The growth direction of NRs was established with the help of HRTEM analysis (Fig. 3.3). The FESEM (Fig. 3.1c and its inset) and TEM (Fig. 3.3a) micrographs reveal that the NRs are bounded by hexagonal surface

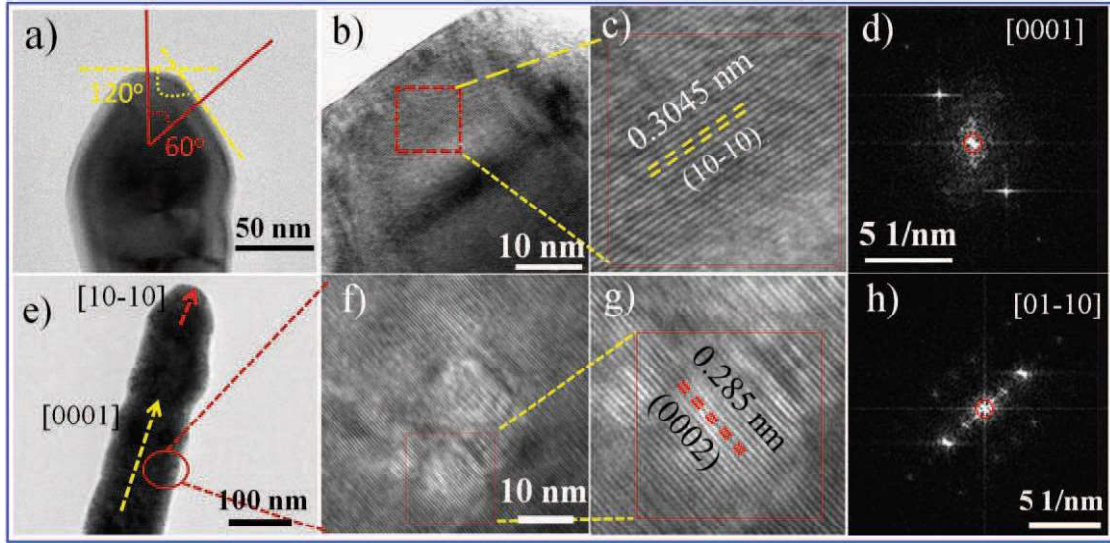


Figure 3.3. Detailed HRTEM analysis of NR grown at 650 °C. a) Low magnification image of apex part of NR which shows that the angle between growth direction and surface facet planes is 60°. b) and c) HRTEM images of apex part of NR and its enlarged view, respectively, showing the (10–10) lattice fringes. d) FFT of apex part of the NR (area is indicated by red square in (c)). e) Low magnification image of NR shows the growth direction of middle part. f) and g) High-resolution images of middle part of the NR and its enlarged view, respectively, showing the lattice fringes of (0002) planes. h) FFT of middle part of the NR (area indicated by red square in (g)).

planes. The surface planes are running parallel to the NR growth direction (Fig. 3.3e). However, the surface planes are inclined with an angle of $120 \pm 2^\circ$ at the apex part of the NR (Fig. 3.3a). The HRTEM images of the apex part of the NR and its enlarged views are shown in Figs. 3.3b and 3.3c, respectively. The lattice spacing of these fringes is found to be 0.304 nm, which corresponds to the (10–10) or $\bar{1}0\bar{1}0$ planes of the InN hexagonal structure. By measuring the angle between the normal to the top and inclined planes of the apex part (Fig. 3.3a), one can rationalize the crystalline plane of the inclined facets. These surface planes are inclined with respect to the [10–10] (Fig. 3.3a). So one can assume that the inclined surface planes can be indexed as $\{10\bar{1}n\}$. The value of n can be derived by measuring the angle between the NR growth direction of [10–10] and the corresponding surface planes. The measured angle

between the surface facet plane and $[10\bar{1}0]$ is found to be $60^\circ \pm 2^\circ$ (Fig. 3.3a). The angle is closely matched with the calculated value between the $\{10\bar{1}0\}$ and $\{10\bar{1}2\}$. Thus, it was assumed that nucleation started in the $[10\bar{1}0]$ growth direction and was bounded by $\{10\bar{1}2\}$ inclined surface planes. The fast Fourier transform (FFT) pattern (Fig. 3.3d) of the corresponding HRTEM images (indicated by the red square in Fig. 3.3c) shows the zone axes along $[0001]$. An enlarged view of the HRTEM image (Fig. 3.3e) of the middle part of the NR is shown in Fig. 3.3f. Lattice spacing between these fringes in the magnified image (Fig. 3.3g) is measured to be 0.285 nm, which corresponds to the (0002) planes. It implies that the growth of NRs is carried over the $[0001]$ or the c -axis. As already reported, nano-columns grown along the c -axis is bounded by hexagonal non-polar $\{10\bar{1}0\}$ surface planes (π -planes).¹⁴ The results imply that the nucleation starts in the $[10\bar{1}0]$ direction and the growth is carried over $[0001]$ direction, as indicated earlier in Fig. 3.3d. The FFT pattern of different regions of the head (Fig. 3.3d) and middle (Fig. 3.3h) parts of NR clearly show different orientations of the crystalline planes with zone axes of $[0001]$ and $[01\bar{1}0]$, respectively. Thus the presence of different crystalline planes at different stages of growth divulges the fact that the nucleation and growth process may entail different surface planes.

The powder XRD (XRD, Bruker, D8 Discover) patterns of nanoparticles grown at 550 °C and NRs grown at 650 °C are shown in Figs. 3.4a and 3.4b, respectively. The observed 2 θ positions were matched with the hexagonal wurtzite phase of InN (JCPDS: 00-050-1239). The diffraction peaks corresponding to (10 $\bar{1}0$), (0002), (10 $\bar{1}1$), (10 $\bar{1}2$), (11 $\bar{1}0$), (10 $\bar{1}3$), (20 $\bar{2}0$), (11 $\bar{1}2$), (20 $\bar{2}1$), (0004), (20 $\bar{2}2$) and (10 $\bar{1}4$) crystalline planes were observed. The XRD pattern of nanoparticles

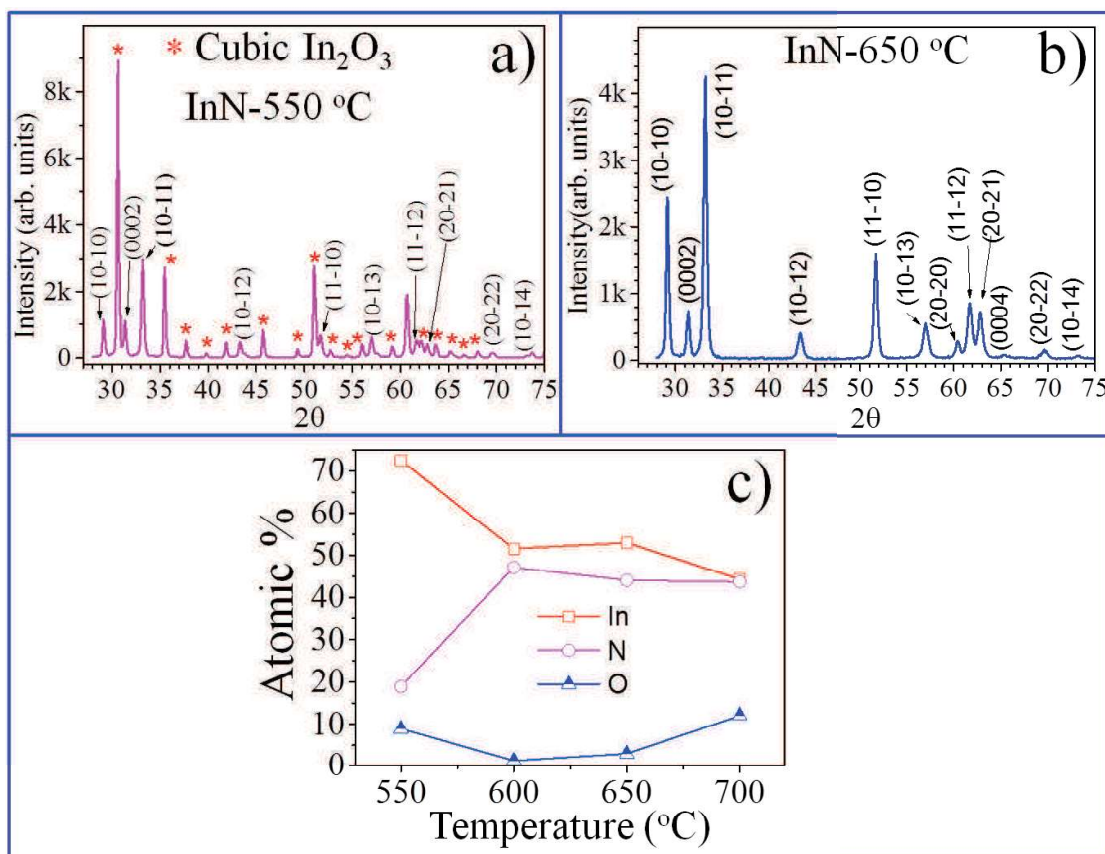


Figure 3.4. XRD pattern of a) nanoparticles grown at 550 °C along with the substantial presence of cubic In₂O₃ and b) NRs grown at 650 °C (JCPDS # 50–1239). c) Variation of atomic percentages of In, N and O in nanostructures grown at different temperatures.

grown at 550 °C showed the hexagonal wurtzite InN phase along with the presence of cubic In₂O₃ phase. The oxide phase is observed because of the presence of ~ 10% O in the samples grown at 550 °C. The presence of O was confirmed by the HRTEM assisted EDS study (Fig. 3.4c). However, substantial changes in the peak positions were not observed in the diffraction patterns of nanoparticles and NRs. From the XRD card (JCPDS: 00-050-1239), the (10–11) plane is found to be the high-intensity reflection plane of the hexagonal InN phase. The intensity (*I*) ratio of the peaks $I_{(10-10)}/I_{(10-11)}$ and $I_{(0002)}/I_{(10-11)}$ was compared in both cases. In the case of nanoparticles, these ratios were observed with values of 0.38 and 0.37, respectively, which were close enough to the reported values (0.44 and 0.41) for InN. However, in the case of

NRs, increase in the $I_{(10-10)}/I_{(10-11)}$ ratio was observed for a value of 0.57 as compared to the $I_{(0002)}/I_{(10-11)}$ ratio of 0.17. A five times increase in the intensity of m -plane (10-10) reveals that NR growth is along the c -axis, which is bounded by six polyhedral surfaces of the m -planes. Thus, the intensity of the m -plane is increased because of the NRs grown along the c -axis are lying along the substrate whereas m -planes with six polyhedral surfaces are exposed to the X-ray beam. Here, m -planes act as a textured surface. So it is obvious that the XRD intensity will be high for the m -planes.

The HRTEM assisted EDS analysis shows the presence of off-stoichiometry in InN nanostructures grown at 550 and 700 °C (Fig. 3.4c). The presence of O was noticeable in nanostructures grown at low and high temperatures of 550 °C and 700 °C, respectively. This may be possible because of the inefficient conversion of In_2O_3 to InN at 550 °C, and dissociation of InN and re-oxidation at 700 °C.¹ In the intermediate temperatures, a negligible amount of O around 1.26 and 2.95 atomic % for samples grown at 600 °C and 650 °C, respectively, were recorded.

3.2.2 Raman spectroscopic studies

Raman spectral acquisition was performed at room temperature using a 100× microscopic objective with N.A. value of 0.90. The un-polarized Raman spectra (Fig. 3.5a) of nanostructures show three prominent symmetry allowed Raman modes in ranges of 83–88, 485–489 and 581–593 cm^{-1} , which may be designated as $E_2(\text{low})$, $E_2(\text{high})$ and $A_1(\text{LO})$ phonon modes, respectively.¹⁵ One can expect all the possible Raman active modes because of the random orientation of nanostructures with respect to the incident laser. A tiny peak is also observed at the shoulder of $E_2(\text{high})$ mode in the range of 471–477 cm^{-1} (Fig. 3.5a, marked by *), which can be assigned as $E_1(\text{TO})$ mode. One cannot distinguish $A_1(\text{LO})$ and $E_1(\text{LO})$ modes, as they are in the same

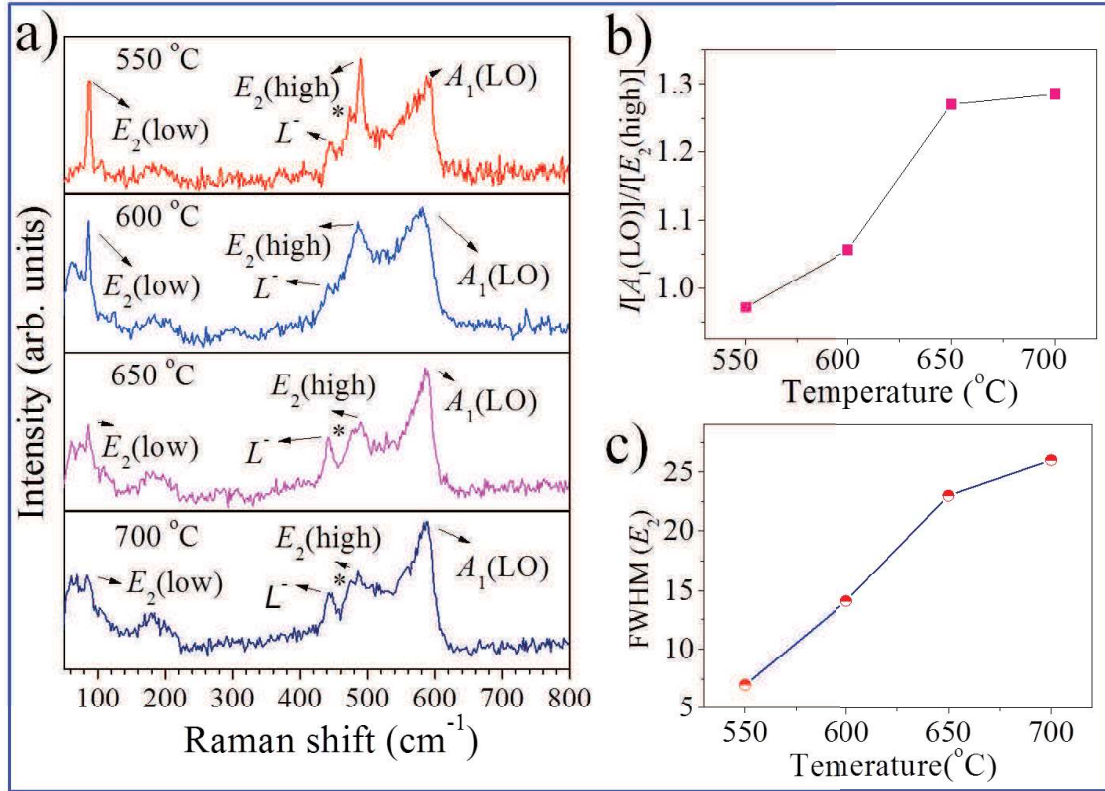


Figure 3.5. Raman spectra of nanostructures grown at temperatures of (a) 550–700 °C. (b) $I(A_1(\text{LO}))/I(E_2(\text{high}))$ at different growth temperatures. Lines are drawn as a guide to the eye. (c) Variation of E_2 mode FWHM with respect to growth temperature. A tiny peak at the shoulder of $E_2(\text{high})$ mode in the range of 471–477 cm^{-1} is assigned to the $E_1(\text{TO})$ (marked by *). L^- is denoted as one of the LOPC modes.

range of 580–596 cm^{-1} . However, the observed peak in the range of 580–596 cm^{-1} may be assigned as the $A_1(\text{LO})$ mode because of its asymmetric broadening, which is attributed to the coupling of LO-phonons with plasma oscillations of free charge carriers of InN.¹⁶ Moreover, the $E_2(\text{high})$ mode is found to be broadened as the growth temperature of nanostructures increases (Fig. 3.5c). A sharp $E_2(\text{high})$ mode with full-width half maxima (FWHM) of 7 cm^{-1} in the Raman spectrum of nanostructures grown at 550 °C indicates high crystallinity in the sample. However, broadening of the $E_2(\text{high})$ mode was observed as the growth temperature was increased. It elucidates the fact that there is a degradation of crystallinity with increasing

temperature. A peak observed in the range of 441–443 cm^{-1} is assigned to the low-frequency plasmon coupled LO phonon mode (L^-).¹⁷ The LO phonons are strongly coupled with the plasmon via a microscopic electric field in polar semiconductors. Coupling of the LO phonons with plasmon leads to the observation of additional modes. The low frequency and high-frequency modes of the LO phonon-plasmon coupled (LOPC) modes are designated as L^- and L^+ , respectively. The frequencies and line shapes of the LOPC modes are sensitive to the electron density and mobility of carriers in the system.¹⁸ In our study, sharp L^- peaks are observed for all the nanostructures. In addition, there was a continuous increase in the intensity (I) ratio of $A_1(\text{LO})$ to $E_2(\text{high})$ peak with increasing growth temperature (Fig. 3.5b). A sharp increase in the $I[A_1(\text{LO})]/I[E_2(\text{high})]$ is observed from 600 to 650 °C. This increase in the intensity ratio may be attributed to the polarization of LO mode in the A_1 symmetry along the c -axis, which is favored in the case of a wurtzite unit cell.¹⁹ HRTEM studies also substantiate that these NRs are grown along the c -axis at an optimal temperature of 650 °C (Fig. 3.3).

3.2.3 Evolution of nanorod growth and optimization

The morphology of the nanostructures is changed significantly from multifaceted nanoparticles to NRs when the growth temperature increases to 650 °C. In order to understand the morphology variation with temperature, the growth was further carried out in the temperature range of 610–640 °C with an interval of 10 °C. Other growth parameters, namely, gas flow rate and growth time were kept constant. The morphology of nanostructures grown in the temperature range of 610–640 °C is shown in Fig. 3.6. However, the morphology of nanostructures grown at 610 °C

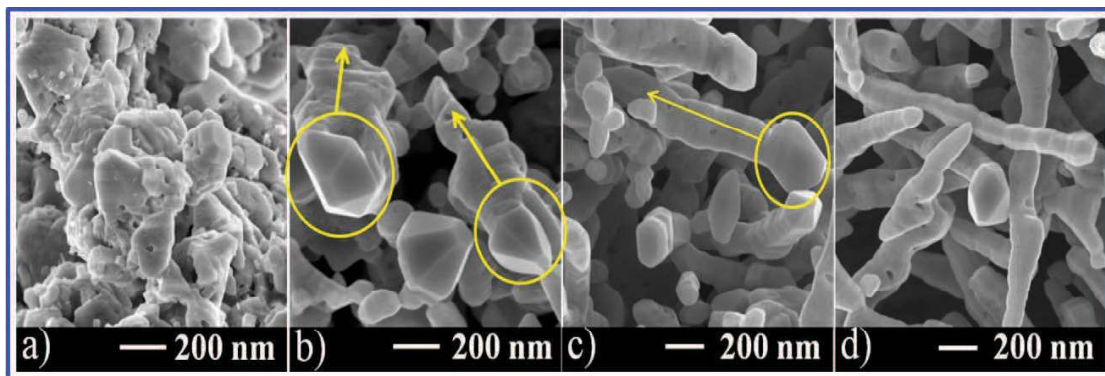


Figure 3.6. Evolution of NRs with increase in growth temperatures a) 610 °C, b) 620 °C, c) 630 °C, and d) 640 °C.

shows the similar growth pattern of multi-faceted nanoparticles as observed for the nanostructures growth at 600 °C (Fig. 3.1b). The agglomeration of nanoparticles started at the growth temperature of 620 °C (Fig. 3.6b). As indicated by arrows in Fig. 3.6b, the agglomeration is headed by one of the multifaceted particles. However, the nanostructures showed a corrugated surface. The growth of NRs with faceted particles at the head (Fig. 3.6c) was prominent at a threshold temperature of 630 °C. The aspect ratio of NRs was found to be increased as the growth temperature was increased to 640 °C (Fig. 3.6d).

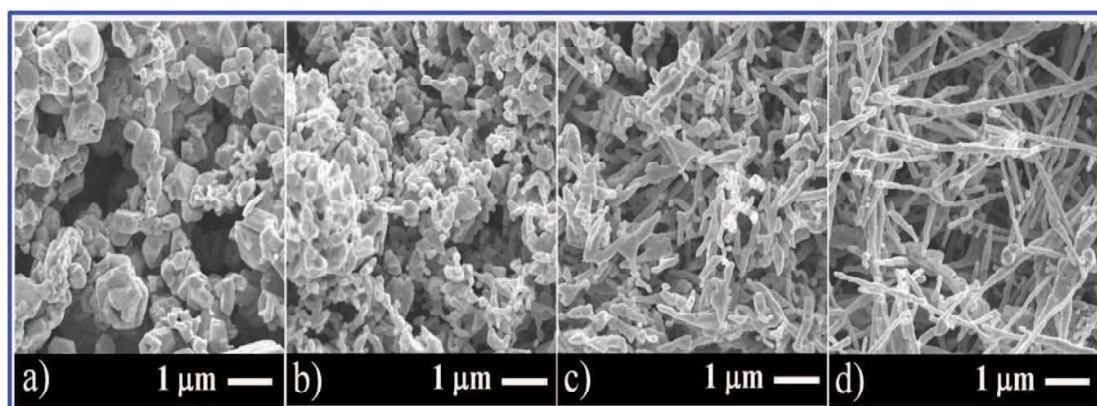


Figure 3.7. Morphology variation with growth times of a) 1, b) 2, c) 3, and d) 4 hr at the optimized growth temperature of 650 °C.

Additionally, the growth time was optimized at the optimized growth temperature of 650 °C. The growth of NRs was not induced with 1 hr of growth time (Fig. 3.7a). However, NRs with small lengths were observed with 2 hr of growth time (Fig. 3.7b). As the growth time was increased to 3 hr (Fig. 3.7c) and further to 4 hr (Fig. 3.7d), the lengths of NRs were found to be gradually increased.

Finally, the effect of NH_3 flow rate was studied at a constant growth temperature of 640 °C and for a growth time of 4 hr. The growth of nanostructures was carried out with different flow rates of 30, 50, 70, and 90 sccm of NH_3 . The morphology of nanostructures with different flow rates is shown in Fig. 3.8. The conversion of In_2O_3 to InN was found to be dependent on the flow rates of NH_3 using the EDS analysis. A large amount of O (~ 55%) was observed for the samples grown

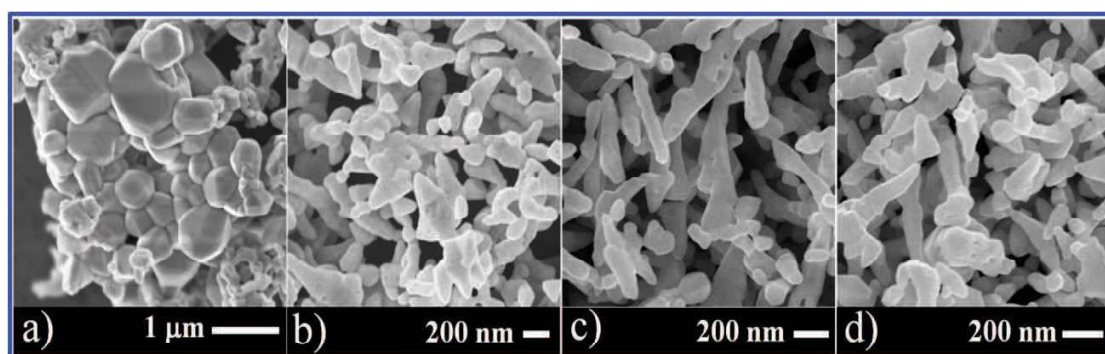


Figure 3.8. Optimization of flow rates a) 30, b) 50, c) 70, and d) 90 sccm at a growth temperature of 640 °C, close to the optimal value. No significant change observed in the morphology above 50 sccm.

with 30 sccm flow rate (Fig. 3.9) showing incomplete conversion of In_2O_3 to InN . In contrast, a negligible amount of O around 1.61 and 1.03 atomic % were observed for the nanostructures grown with flow rates of 50 sccm and 70 sccm, respectively, as found in the EDS analysis (Fig. 3.9). Indium atomic percentage was also found to be increased when the flow rate changes from 50 to 70 sccm (Fig. 3.9). Moreover, the metallic In was found to segregate at the bottom of the ceramic boat when

nanostructures were grown with 50 and 70 sccm of NH_3 (not shown in the figure). In contrast, there was no trace of In on the boat during the growth at 90 sccm and above.

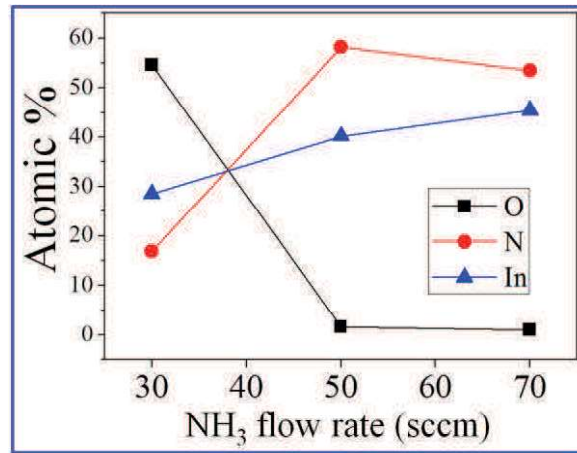


Figure 3.9. Variation of atomic percentages of In, N and O in nanostructures grown with different flow rates at 640 °C.

This observation suggests that because of the lack of N in the reaction chamber, some of the metallic In is left out without forming the InN for growth carried out at low flow rates ≤ 70 sccm. Thus, 100 sccm of NH_3 flow rate is found to be a reasonable value for converting a total amount of In_2O_3 to stoichiometric InN. In a previous study, the morphology of GaN nanostructures grown from Ga_2O_3 was reported to be dependent on the NH_3 flow rate.¹⁴ However, in the present study with In_2O_3 , significant morphological changes are not observed with the flow rates above 50 sccm (Figs. 3.8b–d).

3.2.4 Growth mechanism of nanorods

Evolution of NRs may be realized by observing two simultaneous processes of 1) transformation of In_2O_3 to InN phase and 2) the temperature dependent nucleation and growth rates. The growth mechanism of InN nanostructures from In_2O_3 powder is understood based on the VS mechanism. The variation in the morphology can be associated with the nucleation (\dot{N}) and growth rates (\dot{G}) of the newly grown phase

during the conversion of In_2O_3 to InN phase at a given temperature. Nucleation and growth are two important steps during the phase formation. The \dot{N} and \dot{G} are strongly dependent on the reaction temperature and diffusion of atomic species, which are eventually dependent on the growth temperature. These two rates are competitive when the phase transformation takes place, and the transformation temperature decides the domination of one above the other. In the case of solidification, nucleation and growth rate dependence on the temperature is schematically shown in Fig. 3.10a. At a lower temperature, the nucleation rate dominates over the growth

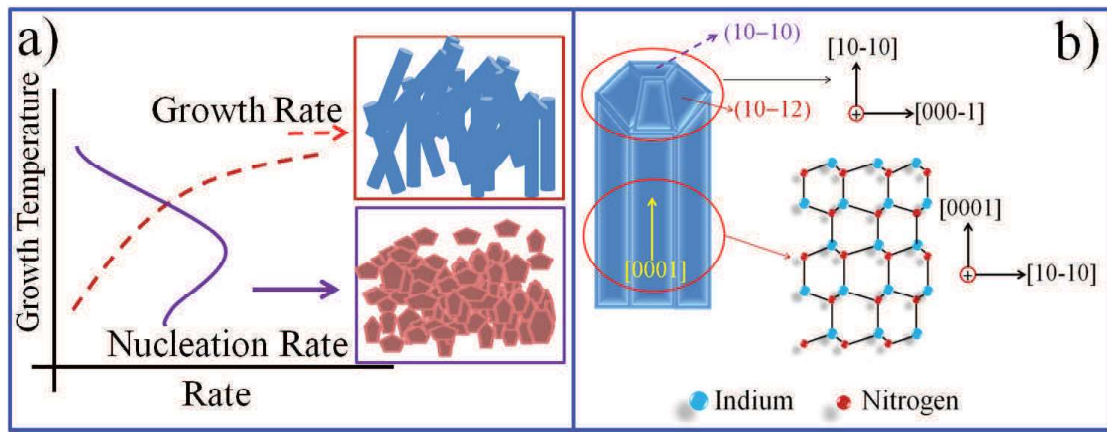


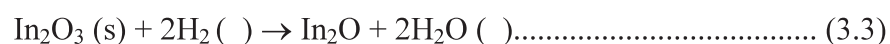
Figure 3.10 a) Graphical illustration of nucleation and growth rates which determine the morphology of nanostructures. b) Schematic of atomic plane arrangement of NR at different parts. The apex (nucleation part) of NR contains $\{10\text{--}12\}$ semi-polar surfaces. These planes can have potential barriers for adatom diffusion because of the polarity. NRs grow along the $[0001]$ direction such that surfaces have non-polar planes, i.e., $\{10\text{--}10\}$ at high temperature ($650\text{ }^{\circ}\text{C}$) where growth rate dominates. Diffusion of adatoms over the non-polar planes depends on temperature only. At high temperature, NRs grow with long-range atomic diffusion over non-polar surfaces.

rate. In contrast, the growth rate dominates at high temperatures. The nucleation rate and growth rates in the case of solidification are expressed by the following equations,²⁰

$$\dot{N} = K_1 K_2 K_3 \left[\exp\left(-\frac{\Delta G^*}{kT}\right) \exp\left(-\frac{Q_d}{kT}\right) \right] \dots\dots\dots (3.1)$$

$$\dot{G} = C \exp\left(-\frac{Q}{kT}\right) \dots\dots\dots (3.2)$$

where K_1 , K_2 and K_3 are related to the number of nuclei in the solid phase, the temperature independent constant and the number of atoms on the nucleus surface, respectively. Q is the activation energy, and C is the temperature independent pre-exponential constant. The equations (3.1) and (3.2) can also be applied to the vapour to solid transformation. According to the equation (3.1), nucleation rate is high at low temperatures with a short-range atomic diffusion. Thus, the diffusion rate at low temperatures limits the growth rate. On the contrary, the growth rate is dominated by a long-range atomic diffusion at high temperature. At given reaction temperature, phase transformation is known to depend on the product of the nucleation rate and the growth rate. All physical phenomena, *e. .*, grain growth and particle size growth, can eventually be explained based on the competitive nature of these two rates. In the present study, the same mechanism was adopted to realize the temperature-dependent evolution of the morphology of InN nanostructures. Usually, nanostructures show a thin sheath of an oxide layer on the surface for an oxide-assisted growth (OAG).²¹ The oxide layer on the NRs surface, however, was not observed in the HRTEM images (Fig. 3.3). Moreover, NRs showed abrupt edges of atomic planes ruling out the OAG of NRs. The possible chemical reactions which may take place in the reaction chamber are expressed by reaction equations (3.3) and (3.4). The reactions take place for the conversion of In₂O₃ to InN without any intermediate phase formation.²² H₂ was present in the chamber as NH₃ was cracked above 450 °C.^{9,10} At elevated temperature and for long growth time, InN can be dissociated to In droplets and N₂ according to the reaction equation (3.5).





The growth temperature is found to play the key role in deciding of the morphology of nanostructures. However, no appreciable change was reported in the morphology of GaN nanostructures with the change in growth temperature using Ga_2O_3 as a precursor.¹⁴ In the present case, even a 10 °C difference in growth temperature shows a significant change in the morphology of InN nanostructures (Fig. 3.6). At low temperatures, low atomic diffusion rates prevent the grain growth. Thus, the nucleation rate dominates at low growth temperatures of 550 and 650 °C. As a consequence, with a dominating nucleation rate, there can be an increased number of nucleation sites as discussed while describing the equation (3.1). In the TEM study, InN nanoparticles are observed with sizes even less than 8 nm (Fig. 3.2). Thus, it demonstrates that the phase conversion from In_2O_3 to InN at temperatures 550 and 600 °C is dominated by the nucleation rate. Had it been a simple conversion of oxide to nitride phase then we would not have observed nanostructures of InN using the commercially procured In_2O_3 powder as a precursor with the size of few tens of micrometer. The dominating nucleation rate and short range atomic diffusion are the reasons for the nanoparticles nature of grown InN phase with a size distribution grown at 550 and 600 °C. However, the formation of InN NRs was observed at the growth temperature of 650 °C. Domination of the growth rate over the nucleation rate at high temperature might be the reason for the growth of NRs. Formation of fewer nucleus sites takes place with increased growth rate, and the nucleated clusters grow to large grain sizes with increasing time. As mentioned previously, NR growth is initiated with the agglomeration of small particles at a temperature of 630 °C with corrugated

surface morphology (Fig. 3.6). Multi-faceted nanoparticles, however, play the critical role in the growth of NRs. At a given temperature, growth starts heterogeneously at certain nucleation sites and does not occur simultaneously throughout the material.²³ The energy provided by the temperatures at 620 and 630 °C is just sufficient for the agglomeration of particles under one of the multi-faceted nucleating particles. A long-range atomic diffusion is dominated for the growth of one-dimensional NRs above the threshold temperature of 630 °C. Thus, the NR growth is achieved by the agglomeration of particles, which are headed by a few of the multi-faceted nanoparticles (Fig. 3.6). HRTEM analysis showed that the multi-faceted nanoparticles, grown at 550 °C (Fig. 3.2c) and the head region of NRs grown at 650 °C (Fig. 3.3c), were both composed of the same (10–10) plane. Nonetheless, NRs are grown along the direction of [0001] or the *c*-axis having a set of polar (0002) planes. Thus, nucleation and growth took place with different planes of the wurtzite InN phase. The head of the NR is also composed of the semi-polar *r*-planes and the surface containing non-polar \bar{r} -planes along the NRs (schematic in Fig. 3.10b). Diffusion over non-polar planes is exclusively dependent on the temperature with an insignificant chemical affinity of the reacting elements over the saturated InN bond.¹⁰ However, growth is favoured in the polar planes of the nanostructures. Thus, increasing the aspect ratio with increasing growth temperature (Figs. 3.1 and 3.6) defines the formation of NRs with growth taking place on the (0001) plane. Two types of morphology are observed in the 700 °C grown samples, namely, NRs and micro-tubes. Micro-tubes may have formed because of the agglomeration of a large number of particles and subsequent growth. Presence of oxygen in the 700 °C grown sample (Fig. 3.4) may also play a significant role in the growth of micro-tubular structures.

3.3 Growth of InN Thin Films

InN films were deposited using the APCVD technique in the temperature range of 560–650 °C. Growth was carried out in a custom-designed CVD set up with a horizontal tube furnace.^{9,10,24} Metallic In (99.999%) shots as the source material and ultra-high purity reactive gas of NH₃ (99.9999%) were used for the growth on single crystalline Al₂O₃(0001) substrates of dimension 5 × 5 mm² without any buffer layer. An alumina boat (99.95%) was used for keeping both the source and substrates. The growth and decomposition temperatures for InN were in the same range. Thus, for effective deposition, special arrangements of the source material and substrate were adopted such that the substrate was surrounded by four In shots at its corner with 5 mm separation. Subsequently, the ceramic boat with the source and substrate was kept inside a 25 mm diameter quartz tube for the deposition. Two different schemes were executed to reach the growth temperature: in one, case (1), the temperature was directly increased with a ramp rate of 20 °C min⁻¹ till it reached the growth temperature and in another, case (2), the temperature was first increased to 500 °C to stay for 30 min before reaching the growth temperature with the same ramp rate of 20 °C min⁻¹. Until the growth temperature was reached, the reaction chamber was maintained at the base pressure of ~10⁻³ mbar using a rotary pump evacuation. Growth was carried out with a NH₃ flow rate of 100 sccm for 2 hr. While maintaining the NH₃ atmosphere up to 400 °C, the furnace was cooled to room temperature after the growth. Successful deposition of the InN films, however, was observed only in the second scheme of temperature ramping.²⁴

3.3.1 Growth mechanism of InN films

As mentioned earlier, deposition of high-quality InN material is difficult in the CVD technique because of the formation and decomposition temperatures of InN fall in the same range (550–650 °C). Nucleation of the InN phase at these temperatures is very difficult because of the occurrence of a simultaneous reversible reaction ($\text{InN} \leftrightarrow \text{In(s)} + \text{N}_2(\text{g})$). The growth scheme carried out using the first kind of ramp rate is shown in Fig. 3.11a. InN deposition was not observed in this scheme, as the nucleation barrier hinders the subsequent growth. It means the simultaneous introduction of reactants and nucleation of InN is impossible in the same range of temperature. In overcoming the nucleation barrier, however, the nucleation sites can be self-seeded using In before introducing the reactive NH_3 . Four processes represented by steps A to D are followed to achieve InN deposition (Fig. 3.11b). Process A involves ramping of the temperature 500 °C, as a first step. Step B comprises seeding of the nucleation sites using In for 30 min. Process C includes the introduction of reactive NH_3 , which is decomposed into atomic N and H_2 . Subsequently, nucleation of InN is initiated at the pre-nucleated In sites. The growth of InN is observed with grain growth over time till process D is completed. This growth mechanism typically follows the Volmer–Weber island growth mechanism followed by coalescence of islands with the possible occurrence of the Ostwald ripening process. Even though the nucleation sites seeded, however, deposition of InN is not observed above the growth temperature of 650 °C, as dissociation of InN takes place at high temperature. On the other hand, the poor crystallinity of the grown material is anticipated in the case of a growth temperature below 560 °C, as the compositional homogeneity may not be achieved at this temperature of the early nucleation stage. To substantiate our growth mechanism,

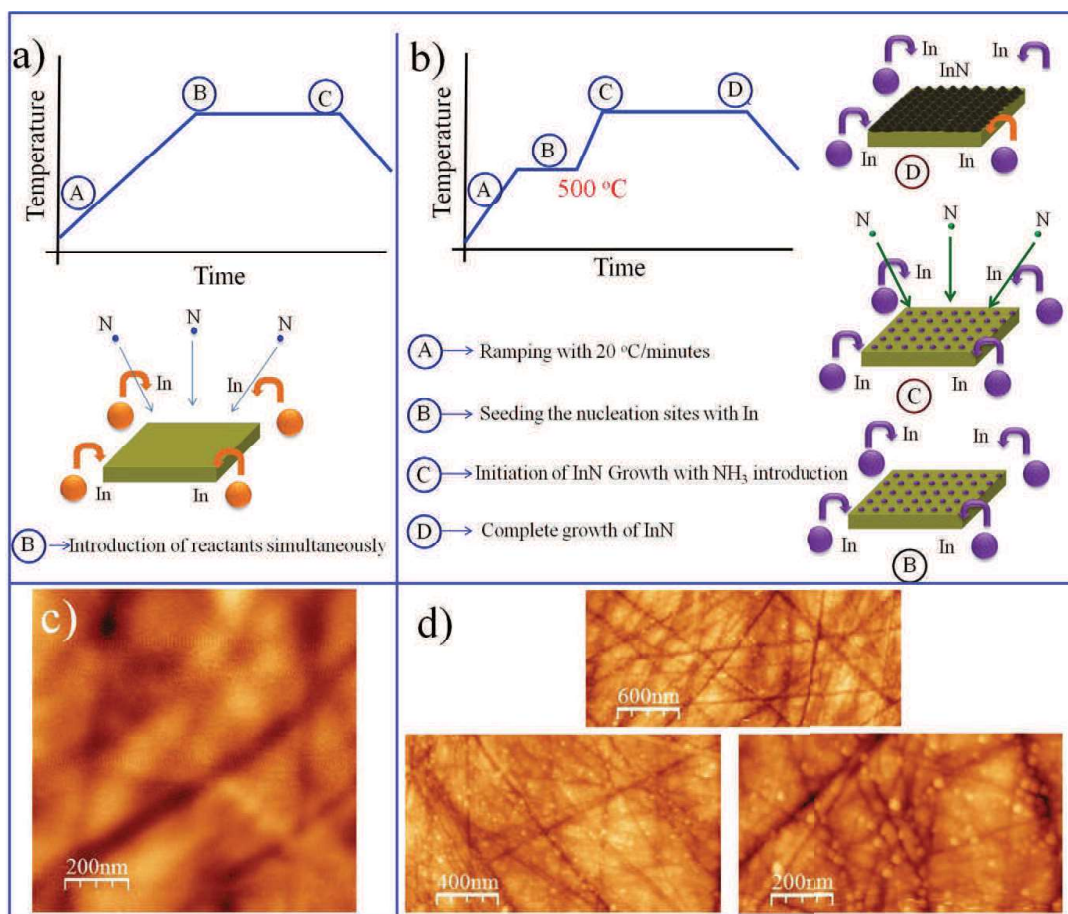


Figure 3.11. Growth of InN with two different ramp schemes with the process steps inscribed in the insets. a) Scheme 1: no deposition observed. b) Scheme 2: successful deposition of InN observed involving four different process steps. AFM topography of the sapphire substrate c) prior to deposition and d) after process B showing uniform nucleation of the seed nanoparticles.

substrate was taken out after process B to study its topography. The morphology of the sapphire substrates before the deposition is shown in Fig. 3.11c. The sapphire substrate after process B shows (Fig. 3.11d) the presence of tiny particles uniformly over the substrates as a result of seeding of the In nucleation sites.

3.3.2 Morphology and structural studies

The typical topography of the nanocrystalline films grown, using the second scheme, in the range of 560–650 °C is shown in Figs. 3.12a–d. The topographic images show

mosaic nature in the grown InN films. III-nitride thin films, grown using the MOCVD technique on the *c*-axis oriented sapphire substrate, is reported to possess a mosaic structure.²⁵ The thicknesses of the grown samples in the present study are in the range of 0.5–0.7 μ . Atomic root mean square (*r_s*) roughness value of 17 nm is observed for the 560 °C grown sample. The *r_s* roughness was found to be 44 and 43 nm for the 580 and 600 °C grown samples, respectively. The high temperature grown sample at 650 °C shows a larger grain size with an *rms* roughness of 35 nm.

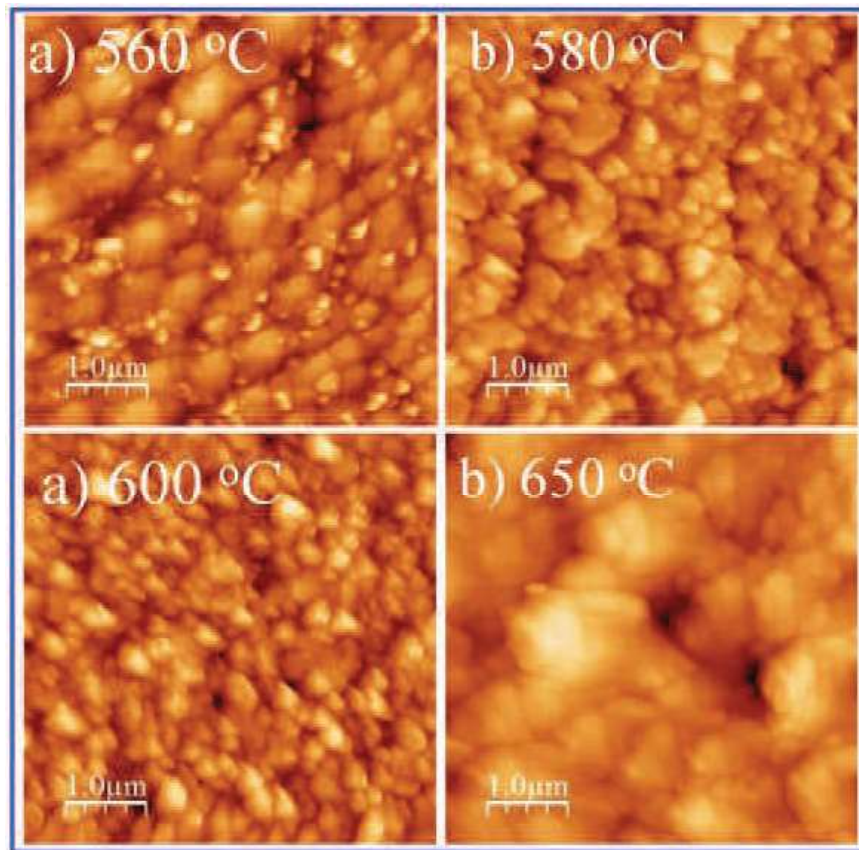


Figure 3.12. AFM topographical images of InN films grown at a) 560, b) 580, c) 600 and d) 650 °C showing a mosaic nature.

3.3.3 Raman spectroscopic studies: Effect of strain and carrier density

Typical Raman spectra, without any background correction, for InN films grown at different temperatures are shown in Fig. 3.13a. In wurtzite crystal, the only allowed

Raman modes in the backscattering configuration of $Z(X-)\bar{Z}$ and $Z(Y-)\bar{Z}$ are E_2 and $A_1(\text{LO})$. The Raman spectra show distinct peaks in the ranges of $84\text{--}85\text{ cm}^{-1}$, 490--

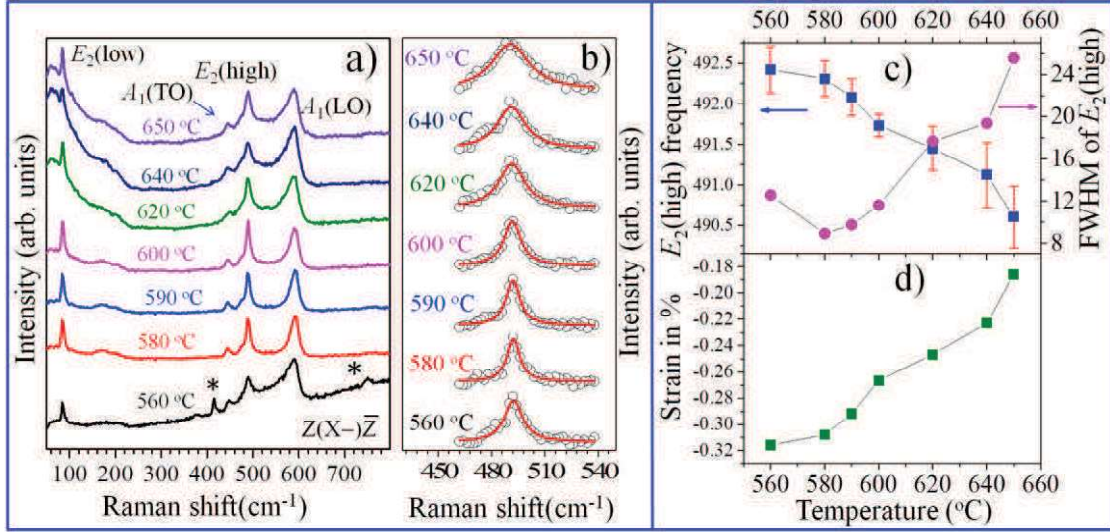


Figure 3.13 a) Raman spectra of InN films grown at different temperatures showing the symmetric and asymmetric nature of the $A_1(\text{LO})$ mode along with other symmetry-allowed and non-zone centre phonon modes. The peaks represented by * symbols are correspond to sapphire phonon modes. b) $E_2(\text{high})$ phonon mode (open circles) spectral region with the Lorentzian fit (solid red curve). c) Change in the $E_2(\text{high})$ phonon mode frequency (right side scale) and its FWHM (left side scale) with respect to temperature. d) Calculated strain relaxation with the growth temperature.

493 cm^{-1} and $589\text{--}593\text{ cm}^{-1}$, which correspond to the $E_2(\text{low})$, $E_2(\text{high})$ and $A_1(\text{LO})$ phonon modes, respectively. The $E_2(\text{high})$ phonon mode is the reliable measure of the strain and crystalline quality of the films, as it is not affected by the carrier density in the material for its non-polar nature.⁶ Moreover, a broadened FWHM of the $E_2(\text{high})$ phonon mode reveals the possible presence of native defects in the crystal.²⁶ The spectral region of the $E_2(\text{high})$ phonon mode of InN films, grown at different temperatures, is shown in Fig. 3.13b. The accurate spectral frequency and FWHM corresponding to the $E_2(\text{high})$ phonon mode were determined by fitting with the Lorentzian function. The frequency of the $E_2(\text{high})$ phonon mode is reported to be

blue-shifted in all films with respect to the strain-free films grown on sapphire in the MBE technique.²⁹ A blue shift of the $E_2(\text{high})$ phonon mode with respect to strain-free value revealed the presence of compressive strain in the films. The compressive strain in the films is attributed to large mismatches of the lattice and thermal expansion coefficients of the substrate and films (lattice parameters: $a_{\text{InN}} = 3.54 \text{ \AA}$, $c_{\text{InN}} = 5.70 \text{ \AA}$, $a_{\text{sapphire}} = 4.758 \text{ \AA}$, $c_{\text{sapphire}} = 12.991 \text{ \AA}$; thermal expansion coefficient in the a plane: $\alpha_{\perp} = 4 \times 10^{-6}$ and $7.5 \times 10^{-6} \text{ K}^{-1}$ for InN and sapphire, respectively) which is biaxial in nature.²⁷ In the present report, however, a red shift in the $E_2(\text{high})$ phonon mode frequency is observed for the increasing growth temperature (Fig. 3.13c, right side scale). In addition, the FWHM of the $E_2(\text{high})$ phonon mode is also increased with the increasing growth temperatures (Fig. 3.13c, left side scale). The film grown at $560 \text{ }^{\circ}\text{C}$, however, has shown the opposite trend for the variation of the FWHM. It may be because of low crystalline quality in samples grown at relatively low temperature. The tiny peak observed in the range of $471\text{-}475 \text{ cm}^{-1}$ is symmetry allowed Raman mode of $E_1(\text{TO})$. The peaks indicated by * symbol in Raman spectrum of $580 \text{ }^{\circ}\text{C}$ grown sample corresponds to the substrate (sapphire) phonon modes.

As the growth temperature increases from 560 to $650 \text{ }^{\circ}\text{C}$, the $E_2(\text{high})$ mode frequency is ultimately red-shifted by 1.82 cm^{-1} . In the case of biaxial strain, according to the symmetry considerations, there are only three non-vanishing strain components which are given by:

$$\varepsilon_{xx} = \varepsilon_{yy} = \left(\frac{a - a_0}{a_0} \right) \dots\dots\dots (3.6)$$

$$\varepsilon_{zz} = \left(\frac{c - c_0}{c_0} \right) = -\frac{C_{13}}{C_{33}} (\varepsilon_{xx} + \varepsilon_{yy}) \dots\dots\dots (3.7)$$

$$\varepsilon_{zz} = -2 \frac{C_{13}}{C_{33}} (\varepsilon_{xx}) \dots\dots\dots (3.8)$$

where C_{ij} is the stiffness coefficient. The strain-induced phonon shift within the limit of Hooke's law is expressed by:

$$\Delta\omega = \omega - \omega_0 = 2a_{E_2} \varepsilon_{xx} + b_{E_2} \varepsilon_{zz} = 2 \left[a_{E_2} - b_{E_2} \frac{C_{13}}{C_{33}} \right] (\varepsilon_{xx}) \dots\dots\dots (3.9)$$

where the coefficients a_{E_2} and b_{E_2} are the phonon deformation potentials in the equation (3.9). However, the deformation potential of InN is reported with scattered values in the literature to a great extent.^{18,28,32} In the present study, the strain was calculated by considering the deformation potentials values as reported by Kim *et al.*,²⁹ $a_{E_2} = -998 \text{ cm}^{-1}$ and $b_{E_2} = -635 \text{ cm}^{-1}$, with the stiffness coefficients of $C_{13} = 124$, and $C_{33} = 200$. Variation of strain with respect to the growth temperature is shown in Fig. 3.13d. The strain is observed to decrease with the increasing growth temperature. In other words, the compressive strain, produced by thermal and lattice mismatch, is found to be relaxed at higher growth temperatures. Moreover, except for films grown at 560 °C, the FWHM of $E_2(\text{high})$ phonon mode is also found to increase with the increasing growth temperature (Fig. 3.13c, left side scale). This observation unambiguously implies that the defect density is increased with the increased growth temperature. The strain produced from the point defects is hydrostatic in nature for the high temperature grown sample, which is either compressive or tensile depending on the involved atom sizes. In the present study, the partial decomposition of InN is more likely to happen at high growth temperatures.¹⁰ As a result of the decomposition, the nucleation of defects may be expected for the films grown at a relatively high temperature leading to the supersaturation of In and formation of In_N anti-site defects

with higher concentration.⁶ Assisted with the structural imperfections, subsequently, strain relaxation takes place which is confirmed with the red shift of the $E_2(\text{high})$

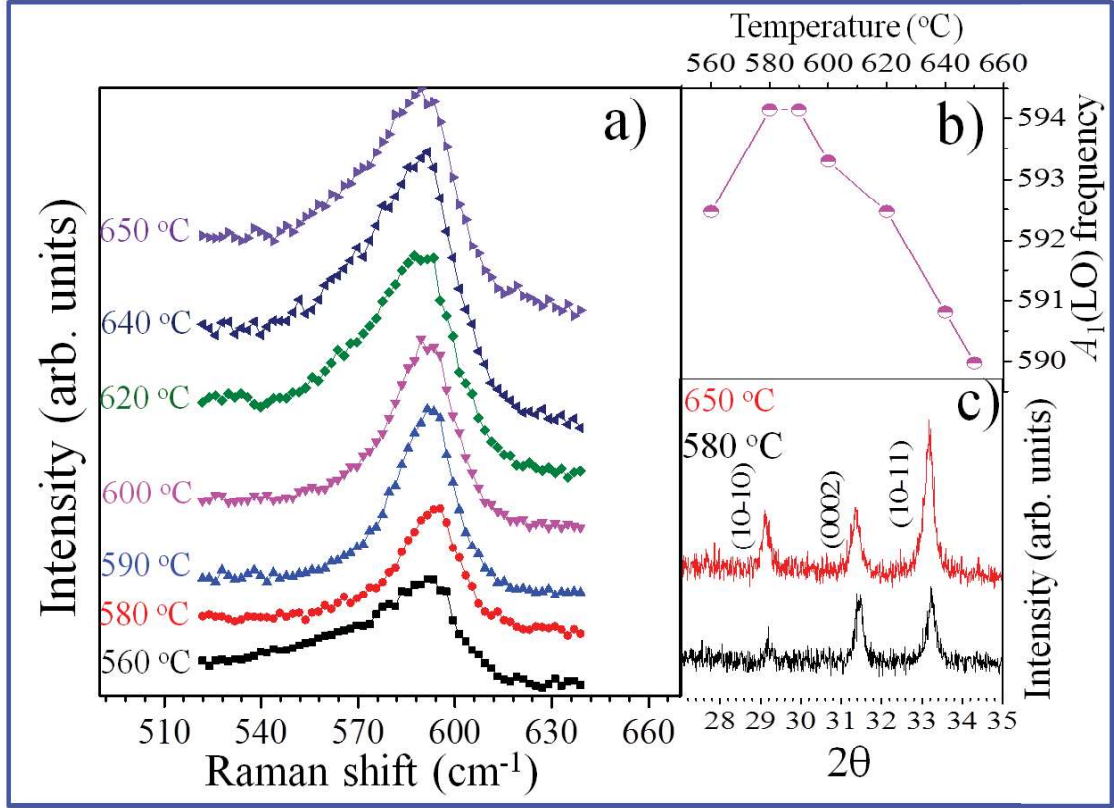


Figure 3.14. a) The spectral region of the $A_1(\text{LO})$ mode. b) Dependence of the $A_1(\text{LO})$ mode frequency with temperature. Lines are to guide the eye. c) XRD pattern of samples grown at 580 and 650 °C (first three reflections shown here).

phonon mode along with the broadening of the FWHM with increasing growth temperature. For the dissociation with the increase in growth temperature, the number of N vacancies (V_N) is increased resulting in the creation of point defects in the grown films. This possible presence of V_N is substantiated with the observed increase in the carrier density for the high temperature grown InN samples.¹ The increase in carrier density in our sample is supported by Raman spectroscopic analysis of the $A_1(\text{LO})$ phonon mode of the films grown at a high temperature, as discussed in the subsequent paragraph. In the present study, the hydrostatic strain originating in the presence of V_N is found to be tensile in nature. Consequently, a compressive strain induced by the

foreign substrate is relaxed by the tensile strain produced by V_N . As a net result, the $E_2(\text{high})$ phonon mode is found to be red-shifted along with an increase in the FWHM for the films grown at high temperatures.

With no visible change in the intensity, the peak observed at 445 cm^{-1} (Fig. 3.13a) is assigned as the $A_1(\text{TO})$ phonon mode, as it is not affected by the carrier concentration of the samples.³⁰ Being forbidden in the backscattering configuration, the appearance of the $A_1(\text{TO})$ mode is attributed to the breakdown of the polarization selection rules due to the misorientation of the crystal with respect to the laser direction. The line shape of the unscreened LO phonon mode, however, is observed to depend on the charge carrier density.^{16,31} The asymmetric broadening of the $A_1(\text{LO})$ phonon mode in InN is a prominent signature for the high carrier density. The $A_1(\text{LO})$ phonon mode, which is observed in the frequency range of $589\text{--}594\text{ cm}^{-1}$ shows that the samples were grown at $580\text{--}600\text{ }^\circ\text{C}$ have the symmetric behavior of the $A_1(\text{LO})$ mode (Fig. 3.13a). On the other hand, an asymmetric broadening of the $A_1(\text{LO})$ phonon mode was found for samples grown at $620\text{ }^\circ\text{C}$ and above. Hence, it is established that a strong coupling of the carrier with the LO phonon is observed for samples grown above $620\text{ }^\circ\text{C}$ because of the possible presence of high carrier density in these samples. The origin of the high carrier density is attributed to the presence of a large number of V_N as a result of partial decomposition of InN at high temperatures, and we have already discussed it earlier. The spectral region of the $A_1(\text{LO})$ phonon mode (Fig. 3.14a) illustrates the symmetric and asymmetric behavior of the mode for samples grown in the temperature ranges of $580\text{--}600\text{ }^\circ\text{C}$ and $620\text{--}650\text{ }^\circ\text{C}$, respectively. The film is grown at $560\text{ }^\circ\text{C}$ also shows the asymmetric behavior of the $A_1(\text{LO})$ mode. However, unlike high temperature grown samples, it may be because of

a poor crystalline quality. Usually, strain in the films is calculated from the shift of the $E_2(\text{high})$ phonon mode with the known influence of $A_1(\text{LO})$ mode on carrier concentration. The $A_1(\text{LO})$ mode is reported to blue shift with increasing carrier density.³² Interestingly, we observed a red shift for the $A_1(\text{LO})$ phonon mode with increasing growth temperature even though the carrier concentration was increased. The $A_1(\text{LO})$ mode is red-shifted by 4.2 cm^{-1} from 580 to 650 °C (Fig. 3.14b) and the value is greater than the shift (1.8 cm^{-1}) measured for the $E_2(\text{high})$ phonon mode (Fig. 3.13a). Thus, it can be inferred that the peak position of the $A_1(\text{LO})$ mode is more subjective to the relaxation of strain rather than that with the carrier density.

Information obtained from Raman spectroscopic analysis is localized because of the laser spot size. XRD patterns of InN films grown at two extreme growth conditions of 580 and 650 °C are shown in Fig. 3.14c. The value of d with three strong reflections of (10–10), (0002), and (10–11) only. All diffraction peaks are well matched with the wurtzite InN phase (JCPDS card 00-050-1239). However, as compared to the strain-free values of InN, the d value is shifted towards the higher side in the case of the 580 °C grown sample. Moreover, the d value is red shifted towards the lower side in the case of the 650 °C grown samples as compared to that for the 580 °C grown sample elucidating the fact that the compressive strain exists in the film grown at 580 °C. The relation occurred led to the lower d values i.e., an increase in the d value with increasing growth temperature. In the case of biaxial strain relaxation, the (10–10) and (0002) reflections must show the opposite trend in the shift of d value. However, the identical shift of the d value is observed for all reflections (Fig. 3.14c) emphasizing the fact that the strain relaxation takes place through a different mechanism being hydrostatic in nature. Hence, the

XRD studies also strongly substantiate the observation made in the Raman spectroscopic analysis.

3.3.4 Photoluminescence spectroscopic studies: Effect of strain and Burstein-Moss shift

The optical band gap of InN has been established in the near-IR region (~0.75 eV).³³ There are only a few reports of optical emission from the CVD grown InN phase. The band gap, observed in the high energy range of 1.9 eV, was related to the energy shift due to the BM effect. From the free electron theory, the magnitude of the energy shift (Δ_{BM}) due to the BM effect is defined as:³⁴

$$\Delta_{BM} = \frac{\hbar^2}{2} \frac{(3\pi^2 n_e)^{2/3}}{m^*} \dots\dots\dots (3.10)$$

where n_e is the carrier density and m^* is the reduced mass of the electron-hole pair. The PL spectra measured at 80K for the InN films grown at different temperatures in the range of 580– 650 °C in shown in Fig. 3.15a. InN films grown using the APCVD technique, for the first time to the best our knowledge, have shown optical emission which requires high crystalline quality. The InN film grown at 560 °C does not show any distinct emission other than mere background, which is attributed to its poor crystalline quality (not shown in the figure). The PL peak is observed at 1.2 eV for the 580 °C grown sample (Fig. 3.15a). The band edge emission is largely blue-shifted as compared to the reported band gap value of 0.75 eV.³³ The observed blue shift of 0.45 eV is attributed to the combined effect of compressive strain as well as the BM shift owing to the considerably high carrier density in the films. With increasing growth temperature, the carrier density is observed to increase as revealed by the asymmetric broadening of the $A_1(\text{LO})$ mode (Fig. 3.14a). However, the red shift in the PL

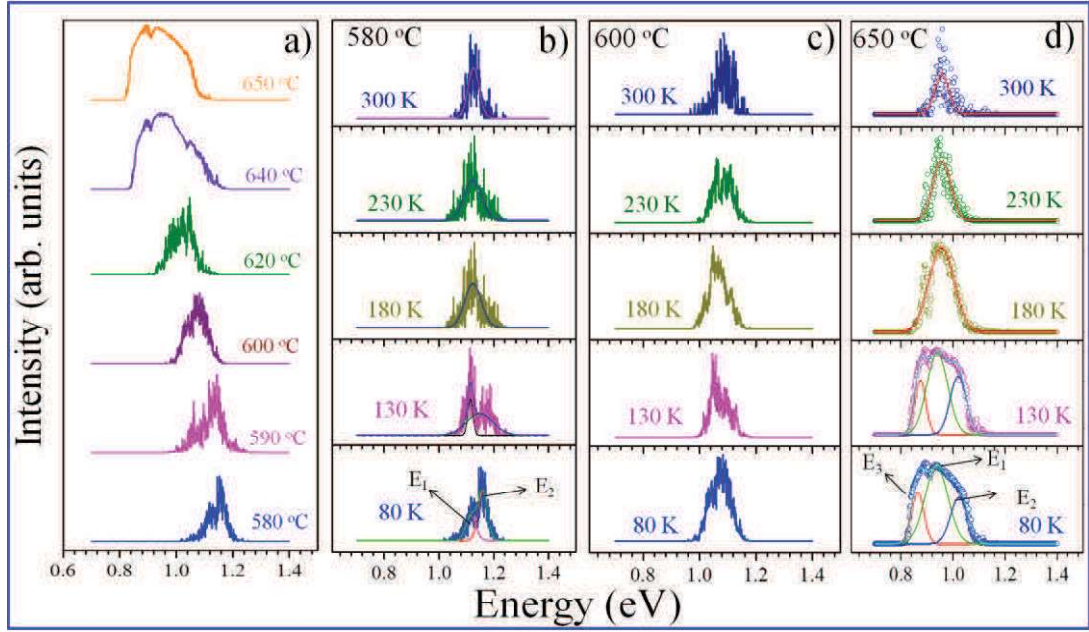


Figure 3.15. a) PL spectra, measured at 80 K, for the InN films grown at different temperatures. The spectra show the redshift of the emission line with the increase in temperature. (b)–(d) show the temperature-dependent PL spectra of the 580, 600, and 650 °C grown samples with a Gaussian fit for b) and d).

emission was observed for the high temperature grown samples instead of blue shift. The observed red shift is attributed to the relaxation of compressive strain in high temperature grown samples. One has to discard the strain effects in the films in order to find the actual shift due to the BM effect. As discussed earlier, one can neglect the strain-related shift in the band edge emission of high temperature grown samples which are the most relaxed films. The band edge peaked is at 0.89 eV for samples grown at 650 °C (Fig. 3.15a) showing a shift of 0.14 eV in the band gap due to the BM effect. Thus, assuming an insignificant contribution of strain in the final blue shift of the PL emission for the sample grown at 650 °C, the approximate carrier density can be calculated as $\sim 4.49 \times 10^{18} \text{ cm}^{-3}$. The band edge is further blue-shifted in the case of the low temperature grown sample even though these samples have a low carrier density. A blue shift in the band edge may be the consequence of the

compressive strain existing in the films. Thus, a compressive strain in the films dominates over the BM shift in the case of the low carrier density samples grown at low temperatures. Moreover, the FWHM of the band edge emission was found to be lower in the case of the low temperature grown samples than that for the high temperature grown samples (Fig. 3.15a). The increase in the FWHM with the increasing growth temperature is attributed to the increased amount of V_N -related defects contributing to the carrier density. An increase in the carrier density eventually results in the band filling effect leading to the broadening of the optical emission lines. From this observation, one can restate that residual strain also plays a crucial role in deciding the band gap of InN along with the shift because of the BM effect. The temperature dependent PL spectra of the samples grown at 580, 600, and 650 °C are shown in Figs. 3.15b-d, respectively. The PL spectra were fitted with the Gaussian function. The 580 °C grown sample (Fig. 3.15b) shows two prominent peaks with energies of E_1 at 1.15 eV and E_2 at 1.16 eV. Interestingly, the intensity of E_2 is diminished with increasing temperature even though it is stronger than the intensity of E_1 at low temperatures. This observation suggests that the origin of E_2 peak may correspond to the free exciton of the wurtzite InN phase.³⁵ In the other hand, the E_1 peak may originate owing to the band edge emission of InN. The peak position of E_1 does not, however, show any variation with temperature indicating degenerate nature of the band edge peak in InN.³⁶ A similar kind of trend is also observed in the case of the samples grown at 600 °C (Fig. 3.15c). The 650 °C grown sample shows a similar PL emission with an increased amount of integrated intensity (Fig. 3.15d). An additional peak, represented by E_3 is also observed in the low energy range. The intensity of the E_3 peak decreases with increasing temperature, and only the band edge

emission is found to dominate at high temperatures. It suggests that the E_3 peak is because of the presence of point defects and may be associated to the presence of V_N acting as a shallow donor as in the case of GaN.³⁷ The disappearance of the E_3 peak at high temperature is recognized with the complete excitation of all carriers to the conduction band from shallow donors. The presence of V_N in the high temperature grown InN samples with high carrier concentration is already discussed in the previous section. Interestingly, the integrated PL intensity is found to reduce

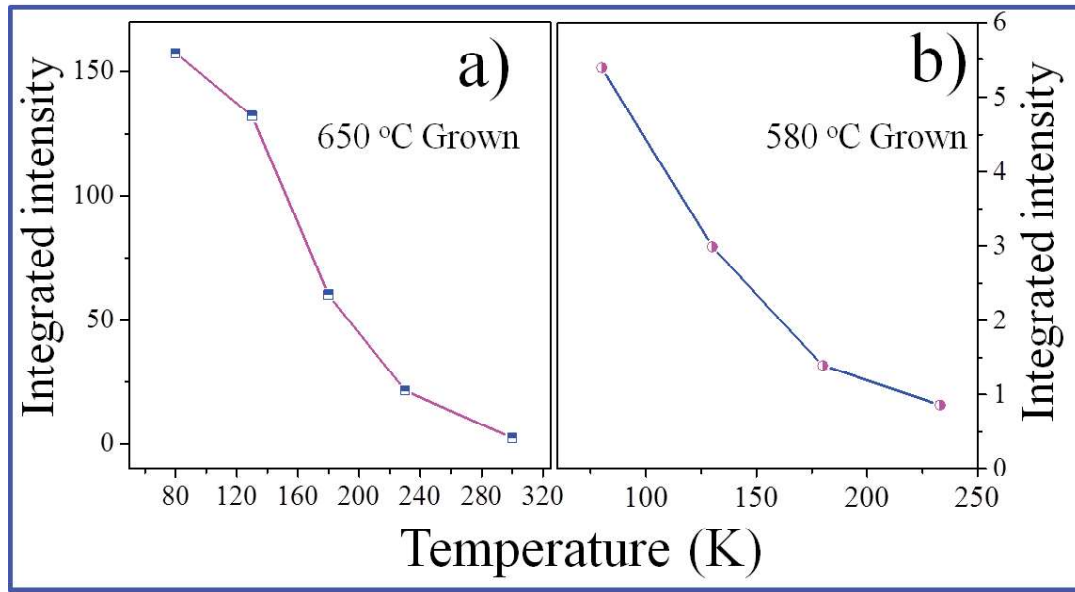


Figure 3.16. Temperature dependence of integrated PL intensity of sample grown at (a) 650 °C and (b) 580 °C.

drastically for all the samples with increasing temperature (Fig. 3.16). The rate of decrease in the integrated PL intensity, however, is more in the case of the high temperature (650 °C) grown samples (Fig. 3.16a) than that for the low temperature (580 °C) grown samples (Fig. 3.16b). The higher rate of decrease in the integrated PL intensity may be ascribed to the increase in Auger recombination in the samples with high carrier density or as a result of surface electron accumulation (SEA).³⁸ In the case of the SEA; localized holes move towards the surface where they recombine non-

radiatively with a large number of electrons. This observation suggests that the effect of the SEA is prominent in the case of the high temperature grown samples.

3.4 Conclusion

In the first part, InN nanostructures are reported to grow by nitridation of In_2O_3 powder in the catalyst-free vapour-solid process. The morphology of these nanostructures was found to vary from QDs to nanorods depending on the growth temperature. Temperature-dependent morphology was explained based on the competitive processes of nucleation rate and growth rates. As a nucleation rate dominated process, QDs and nanoparticles are grown at relatively low temperatures. Nanorods are grown at high temperature due to long-range atomic diffusion through a non-polar surface where the growth rate dominates. Nucleation starts with multifaceted particles having polar surface planes, and growth is carried over non-polar surface planes.

In the second part, the growth of optically high-quality InN films is reported. A novel method of self-seeded catalytic approach was adopted to surmount the difficulties in the synthesis of InN using the APCVD technique. Raman spectroscopic analyses of the $E_2(\text{high})$ and $A_1(\text{LO})$ modes are carried out for the study of the strain and carrier density in these films. Compressive strain, resulting from the lattice and thermal expansion mismatch, is found to be relaxed at high temperature by hydrostatic tensile strain introduced by the V_N . Strain relaxation at high temperature is further supported by the observed red shift in the optical emission line. Finally, the blue shift in the band edge emission of InN cannot be attributed solely to the BM effect. The presence of compressive strain in the films should be considered along with the BM effect.

3.5 References

1. A. G. Bhuiyan, A. Hashimoto and A. Yamamoto, *J. Appl. Phys.* **2003**, 94, 2779.
2. V. M. Polyakov and F. Schwierz, *Appl. Phys. Lett.* **2006**, 88, 032101.
3. B. E. Foutz, S. K. O'Leary, M. S. Shur and L. F. Eastman, *J. Appl. Phys.* **1999**, 85, 7727.
4. O. Ambacher, M. Brandt, R. Dimitrov, T. Metzger, M. Stutzmann, R. Fischer, A. Miehr, A. Bergmaier and G. Dollinger, *J. Vac. Sci. Technol., B: Microelectron. Nanometer Struct.--Process., Meas., Phenom.* **1996**, 14, 3532.
5. A. K. Murali, A. D. Barve and S. H. Risbud, *Mater. Sci. and Eng.: B* **2002**, 96, 111.
6. C. Kisielowski, J. Krüger, S. Ruvimov, T. Suski, J. Ager III, E. Jones, Z. Liliental-Weber, M. Rubin, E. Weber and M. Bremser, *Phys. Rev. B* **1996**, 54, 17745.
7. S. Dhara, A. Datta, C. Wu, Z. Lan, K. Chen, Y. Wang, C. Hsu, C. Shen, L. Chen and C. C. Chen, *Appl. Phys. Lett.* **2004**, 84, 5473.
8. S. D. Hersee, X. Sun and X. Wang, *Nano Lett.* **2006**, 6, 1808.
9. K. K. Madapu, S. Dhara, S. Amirthapandian, S. Polaki and A. Tyagi, *J. Phys. Chem. C* **2013**, 117, 21930.
10. K. K. Madapu, S. Dhara, S. Polaki, S. Amirthapandian and A. Tyagi, *CrystEngComm* **2015**, 17, 3139.
11. P. K. Palomaki, E. M. Miller and N. R. Neale, *J. Am. Chem. Soc.* **2013**, 135, 14142.
12. O. Briot, B. Maleyre and S. Ruffenach, *Appl. Phys. Lett.* **2003**, 83, 2919.
13. B. Maleyre, O. Briot and S. Ruffenach, *J. Cryst. Growth* **2004**, 269, 15.
14. C. Y. Nam, D. Tham and J. E. Fischer, *Appl. Phys. Lett.* **2004**, 85, 5676.
15. K. K. Madapu, N. R. Ku, S. Dhara, C. P. Liu and A. K. Tyagi, *J. Raman Spectrosc.* **2013**, 44, 791.
16. T. Kozawa, T. Kachi, H. Kano, Y. Taga, M. Hashimoto, N. Koide and K. Manabe, *J. Appl. Phys.* **1994**, 75, 1098.
17. Y. Cho, M. Ramsteiner and O. Brandt, *Phys. Rev. B* **2012**, 85, 195209.
18. D. Wang, C. C. Tin, J. R. Williams, M. Park, Y. S. Park, C. M. Park, T. W. Kang and W. C. Yang, *Appl. Phys. Lett.* **2005**, 87, 242105.
19. H. Hiroshi, *J. Phys: Condens. Matter* **2002**, 14, R967.
20. W. D. Callister and D. G. Rethwisch, *Materials science and engineering*. (John wiley & sons NY, **2011**).
21. B. Mandl, J. Stangl, E. Hilner, A. A. Zakharov, K. Hillerich, A. W. Dey, L. Samuelson, G. Bauer, K. Deppert and A. Mikkelsen, *Nano Lett.* **2010**, 10, 4443.

22. J. Jian, X. Chen, M. He, W. Wang, X. Zhang and F. Shen, *Chem. Phys. Lett.* **2003**, 368, 416.
23. J. Ristić, M. Čilek, M. Fernández-Garrido, L. Cerutti, A. Trampert, U. Jahn and K. H. Ploog, *J. Cryst. Growth* **2008**, 310, 4035.
24. K. K. Madapu and S. Dhara, *CrystEngComm* **2016**, 18, 3114.
25. V. Kladko, A. Kolomys, M. Slobodian, V. Strelchuk, V. Raycheva, A. Belyaev, S. Bukalov, H. Hardtdegen, V. Sydoruk and N. Klein, *J. Appl. Phys.* **2009**, 105, 063515.
26. J.-S. Song, H. Rho, M. Jeong, J.-W. Ju and I.-H. Lee, *Phys. Rev. B* **2010**, 81, 233304.
27. B. Jogai, *Phys. Rev. B* **1998**, 57, 2382.
28. V. Darakchieva, P. Paskov, E. Valcheva, T. Paskova, B. Monemar, M. Schubert, H. Lu and W. Schaff, *Appl. Phys. Lett.* **2004**, 84, 3636.
29. K. Kim, W. R. Lambrecht and B. Segall, *Phys. Rev. B* **1996**, 53, 16310.
30. R. Cusco, E. Alarcon-Llado, J. Ibanez, T. Yamaguchi, Y. Nanishi and L. Artus, *J. Phys. Condensed Matter* **2009**, 21, 415801.
31. I. Tiginyanu, A. Sarua, G. Irmer, J. Monecke, S. Hubbard, D. Pavlidis and V. Valiaev, *Phys. Rev. B* **2001**, 64, 233317.
32. X. Wang, S.-B. Che, Y. Ishitani and A. Yoshikawa, *Appl. Phys. Lett.* **2006**, 89, 171907.
33. M. S. Hu, W. M. Wang, T. T. Chen, L. S. Hong, C. W. Chen, C. C. Chen, Y. F. Chen, K. H. Chen and L. C. Chen, *Adv. Funct. Mater.* **2006**, 16, 537.
34. A. Walsh, J. L. Da Silva and S.-H. Wei, *Phys. Rev. B* **2008**, 78, 075211.
35. S. Zhao, S. Fatholouloumi, K. Bevan, D. Liu, M. G. Kibria, Q. Li, G. Wang, H. Guo and Z. Mi, *Nano Lett.* **2012**, 12, 2877.
36. T. Stoica, R. Meijers, R. Calarco, T. Richter and H. Lüth, *J. Cryst. Growth* **2006**, 290, 241.
37. M. A. Leaci and D. Moras, *J. Appl. Phys.* **2005**, 97, 061301.
38. I. P. Seetoh, C. B. Soh, E. A. Fitzgerald and S. J. Chua, *Appl. Phys. Lett.* **2013**, 102, 101112.

CHAPTER 4

GROWTH OF InN NANOSTRUCTURES ON SAPPHIRE SUBSTRATE AND EXCITATION DEPENDENT RAMAN STUDIES

4.1 Introduction

As mentioned in the previous chapters, the growth of InN is suffered from the lack of native substrates. As a result, the misfit and threading dislocations are generated in order to relax the strain caused by the thermal and lattice mismatch.^{1,2} The misfit dislocations are one more factor to reduce the quality of the InN along with its inherent properties. In this context, nanostructures with the high surface to volume ratio can effectively alleviate strain effects through the lateral strain relaxation.³ Thus, it is vital to carry the growth the InN nanostructures in APCVD and study their properties. In addition, InN is reported to possess the surface electron accumulation (SEA) close to the surface region.⁴⁻⁶ The surface electron properties, however, can be manipulated using the growth parameters and external doping. Till now, the precise manipulation of the surface electron properties of InN reported only in case of nanostructures grown by controlled techniques such as MBE.⁷ It is essential to study the surface electron properties InN nanostructures grown by APCVD technique and the influence of the growth parameters.

In addition, InN is reported to have the widest phonon band gap and smallest photon band gap. As a result, InN was predicted to have the applications in hot carrier solar-cells.^{8, 9} Thus, it is important to study the phonon structure of InN with the excitation in the IR as well as in the visible region for developing InN based devices. The resonance excitation strongly influences the phonon structure. The band gap of

InN falls in the NIR region and one can expect dramatic changes in the phonon structure of InN when it is excited with light in the IR region, and subsequently in the device performance.

The present chapter discusses the growth of InN nanostructures using the APCVD technique via self-seeded catalytic approach. Subsequently, the vibrational and optical properties of these nanostructures were studied. In addition, the role of 2D plasmons in the Raman spectrum is discussed. The surface electron properties of selected samples are studied using the photoemission spectroscopy (PES). Finally, phonon structures of InN nanostructures are explored using excitation-dependent Raman studies. The effects of the intrinsic carrier concentration as well as thermally excited carriers were also studied for understanding the forbidden Raman mode in the near-resonance condition.

4.2 Growth of InN Nanostructures on Sapphire Substrate

4.2.1 Growth and morphological studies

InN nanocrystals were prepared using the APCVD technique with a horizontal tube furnace,¹⁰⁻¹² using metallic In (99.999%) and reactive NH₃ (99.999%) as the precursor materials. The growth was carried out on a sapphire substrate via self-seeded catalytic approach. The growth method was similar to the growth of the InN films, which was discussed in the previous chapter (Section 3.3). However, the method was slightly modified in order to achieve the growth of InN nanostructures. In contrast to the film growth, a low density of In nucleation sites were seeded by changing the arrangement as well as separation between the In metal sources and the substrate. In the present growth procedure, the In shots and sapphire substrate was kept with a separation of 1

cm in the downward flow direction (schematic Fig 2.1), whereas in previous case four In shots were kept around the substrate in a close proximity with a separation of 0.5 cm (schematic in Fig. 3.11b). The growth temperature was selected such that nanostructures possess the variable carrier density depending on the structural quality in the film. In the previous chapter, InN films show the asymmetric broadening in the $A_1(\text{LO})$ phonon mode in the Raman spectra if the growth is carried out $\geq 620^\circ\text{C}$. The asymmetric broadening of $A_1(\text{LO})$ phonon indicates that the sample grown $\geq 620^\circ\text{C}$ have higher carrier density as compared to that for the sample grown below it. In the present case, the growth of the nanostructures is carried out at 580, 600, 620, 630, and 650 $^\circ\text{C}$. Figures 4.1a–e show the variation of the morphology of the nanoparticles with growth temperature. The sample grown at 580 $^\circ\text{C}$ shows the nanostructures with random morphology (Fig. 4.1a). Similarly, the sample grown at 600 $^\circ\text{C}$ also shows randomly oriented nanostructures (Fig. 4.1b). The growth with plenty of protruded hexagonal nanostructures was observed in the case of the 620 $^\circ\text{C}$ grown sample (Fig. 4.1c). However, the 630 and 650 $^\circ\text{C}$ grown samples also show randomly oriented nanostructures with no specific features (Figs. 4.1d and 4.1e).

4.2.2 Raman spectroscopic studies: Observation of 2D plasmon peak

As discussed earlier, InN possesses SEA which can influence its vibrational and optical properties. The LO phonon modes create the microscopic electric field during the vibration resulting into the coupling of the LO phonon modes with the free charge carriers through the Fröhlich interaction. The coupling leads to the observation of plasmon-phonon coupling modes in the vibrational spectrum.^{12,13} Room-temperature (RT) Raman spectra of samples grown at different temperatures are shown in Figs.

4.1f–j. The distinct phonon peaks are observed around the wave numbers of 87, 445, 490 cm^{-1} , which correspond to the symmetry allowed $E_2(\text{low})$, $A_1(\text{TO})$, and $E_2(\text{high})$

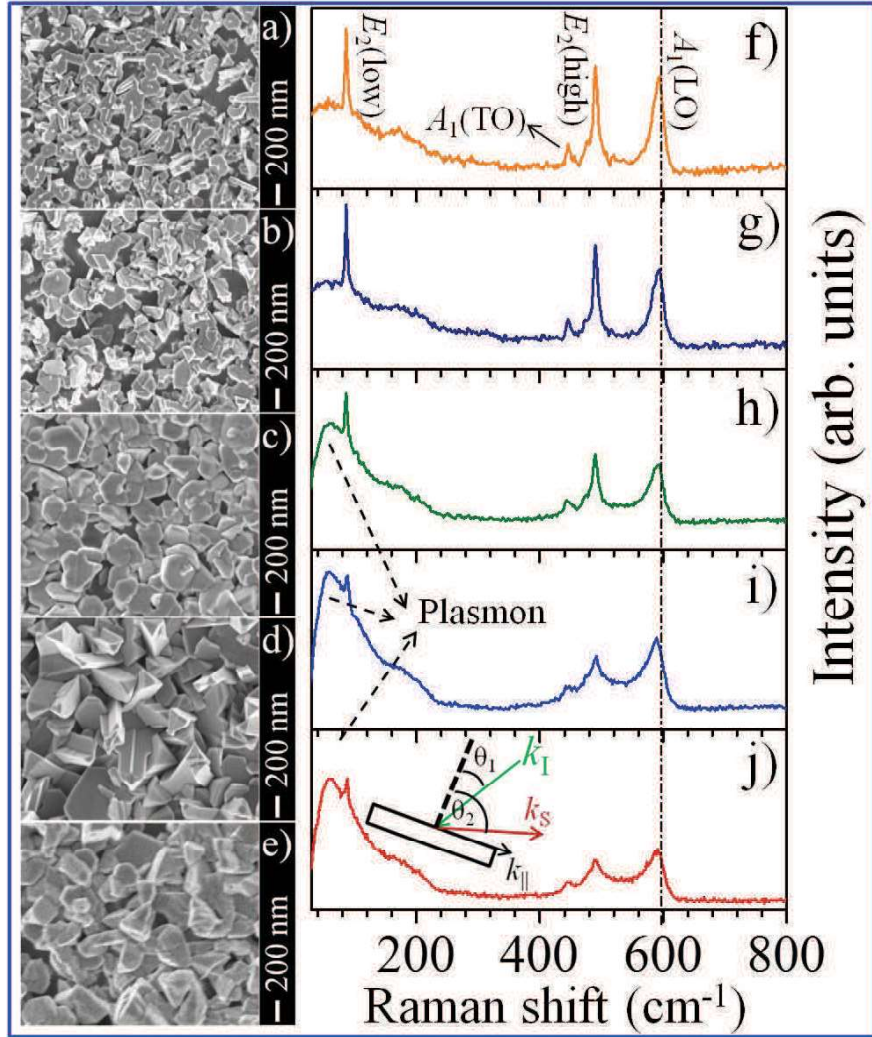


Figure 4.1. FESEM micrographs of the InN nanostructures grown at different temperatures. (a) 580 (b) 600 °C: shows random nanostructures, (c) 620 °C: shows nanostructure with protruded hexagonal features, (d) 630 °C and (e) 650 °C: shows random nanostructures. (f)–(j) Raman spectra of InN nanostructures grown at 580, 600, 620, 630, and 650 °C. A low-frequency peak, which is attributed to the 2D plasmon excitation, is evolved in high-temperature grown samples (≥ 620 °C). The schematic of the scattering geometry is shown in the inset of the (j).

phonon mode frequencies of the wurtzite InN, respectively.^{12,13} Considerably low full-width half maxima (FWHM) of the $E_2(\text{high})$ phonon modes reveal highly crystalline quality of the samples. The phonon mode near the unscreened $A_1(\text{LO})$ mode in the

spectra shows different behavior of asymmetric broadening in the higher temperature (≥ 620 °C) grown samples as compared to that for the lower temperature (<600 °C) grown samples. This observation suggests that Fano interference between carriers and LO phonons, instead of the plasmon-phonon coupling modes, dominates in the present case leading to the asymmetric nature of the $A_1(\text{LO})$ mode. Consequently, the peak observed in the range of $585\text{--}595\text{ cm}^{-1}$ is assigned as the unscreened $A_1(\text{LO})$ mode. Generally, the Fano line shape arises because of the interference between discrete phonon modes and background continuum electron transitions in the system.¹⁴ The red shift in the $A_1(\text{LO})$ phonon mode is observed with the increase in the growth temperature from 580 to 650 °C.

The asymmetric line shape of the $A_1(\text{LO})$ phonon mode elucidates the fact that the samples grown ≥ 620 °C may have higher carrier density compared to those for the samples grown below 620 °C (Figs. 4.1f-j). Increasing carrier density with increasing growth temperature may be understood from the following fact that the probability of the formation of nitrogen vacancies (V_N) increases with increasing growth temperature because of the low thermal stability of InN.¹² At the same time, V_N contribute to the background carrier density,² which may lead to the asymmetric broadening of the $A_1(\text{LO})$ phonon mode. In addition, instead of the low-frequency plasmon-phonon coupling mode (L^-),¹⁵ the phonon mode observed at 443 cm^{-1} is assigned as the $A_1(\text{TO})$ mode because of its passiveness towards carrier concentration. However, the $A_1(\text{TO})$ mode is forbidden in the present configuration. The appearance of the forbidden $A_1(\text{TO})$ mode is attributed to the breakdown of the polarization selection rules as a finite size effect in nanostructures.

In addition to the asymmetric broadening of the $A_1(\text{LO})$ phonon, there is a prominent difference in the low wavenumber region of the Raman spectra (Figs. 4.1f–j). There is a tiny peak appeared around 57 cm^{-1} for the row $\geq 620^\circ\text{C}$. The low-frequency peak is strengthened, as the growth temperature is increased. The low-frequency mode is attributed to the plasmon excitation in the InN nanostructures. However, the bulk plasmon frequency of the presently studied InN nanostructures is calculated to be 1968 cm^{-1} with the carrier density of $\sim 2.53 \times 10^{19} \text{ cm}^{-3}$, which is estimated from the Burstein–Moss (BM) shift in the PL spectra (discussed in the subsequent section). Moreover, the LSPR frequency of the In clusters, if at all present, in the InN matrix is reported to be in the range of $0.5\text{--}1 \text{ eV}$ ($4033\text{--}8100 \text{ cm}^{-1}$).^{15,16} Thus, the observed low wavenumber Raman spectral feature can neither be attributed to the bulk plasmon frequency nor to the LSPR of In clusters in the InN matrix. The low-frequency peak may originate because of the 2D plasmonic oscillations of the SEA. The 2D plasmonic oscillations can be probed using Raman spectroscopy.^{17,18} The condition for the excitation of the 2D plasmons in the layered structure is $k_{\parallel}d \ll 1$, where k_{\parallel} is the in-plane wave vector and d is the thickness of the layered structure.¹⁷ The in-plane wave vectors, in backscattering geometry, can be written as the $k_{\parallel} = (2\pi/\lambda)(\sin \theta_1 + \sin \theta_2)$, where θ_1 and θ_2 are the angles between the incident beam and normal to the surface and scattered beam and normal to the surface, respectively. The minimum and maximum in-plane wave vector transfer occur at angles of 0° and 90° , respectively, because of the random alignment nanocrystals with respect to the incident laser as shown in the schematic (inset of Fig. 4.1j). Considering d in the range of $4\text{--}10 \text{ nm}$ as the width of the SEA of InN nanostructures and incident and scattering angles of 45° , the value of k_{\parallel} can be calculated $2\sqrt{2}\pi/\lambda$ meeting the condition $[k_{\parallel}d$

(0.07–0.17)<<1] for the PP excitation.¹⁶ The presence of In–In adatoms on the surfaces of InN is the physical origin of the SEA.¹⁹

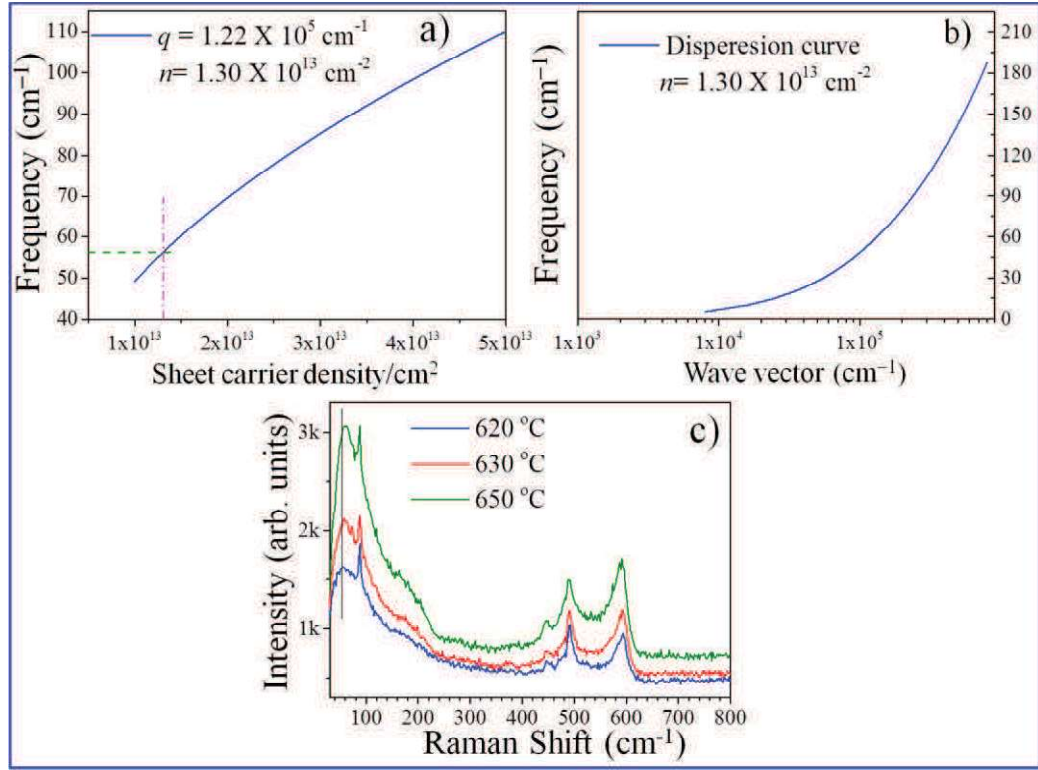


Figure 4.2. (a) Sheet carrier density-dependent 2D plasmon frequency of 2DEG corresponding to the SEA of InN and its (b) dispersion curve. (c) Variation of 2D plasmon peak frequency with increasing growth temperature.

The plasmon frequency (ω_p) is scaled with the square root of the carrier density of the system in the case of 3D plasmonic material. On the other hand, ω_p depends on the in-plane wave vector as well as areal carrier density in the case of the 2D plasmonics.^{17,18,20} The plasmon frequency of 2DEGs is written as

$$\omega_p^2 = \frac{n_s e^2}{m^*} \frac{q}{\epsilon_1 + \epsilon_2 \coth(qd)} \dots\dots\dots (4.1)$$

where n_s is the areal carrier density of 2DEG, m^* the effective mass of electron, ϵ_1 and ϵ_2 are the dielectric constants of the substrate and surrounding media, q is the in-plane wave vector and d is the thickness of the 2D electron system. The 2D plasmon

frequency of the SEA for InN was calculated using the equation (4.1). The variation of the plasma frequency with respect to the areal carrier density is shown in Fig. 4.2a. The bulk InN is considered as the substrate ($\epsilon_1=14$) for the calculation of plasmon frequency with the width of the SEA as 6 nm, and m^* as 0.13 m_0 (m_0 , rest mass of electron) in the SEA region.²¹ The calculated plasma frequency (Fig. 4.2a) is of the order of the observed low-frequency peak in the Raman spectra. The observed plasma frequency of 57 cm^{-1} (~ 1.7 THz) in the Raman spectra (Figs. 4.1f-j) corresponds to the areal carrier density $1.3 \times 10^{13} \text{ cm}^{-2}$, which closely matches with the earlier reported values.²² Dispersion curve corresponding to the areal carrier density of $1.3 \times 10^{13} \text{ cm}^{-2}$ is shown in Fig. 4.2b. Moreover, the plasmon frequency is found to be blue-shifted as the growth temperature increases above 620 °C (Fig. 4.2c).

4.2.3 PL and UPS studies: Confirmation of surface electron accumulation

Possession of SEA was substantiated by the PL emission studies of these nanostructures. The integrated PL intensities of the high temperature grown samples (≥ 620 °C) are found to be higher than that for the low temperature grown samples (Figs. 4.3a–c), indicating the possibility of a higher amount of SEA for the InN nanostructures in the former.²³ The broadening of band edge emission is attributed to the combination of radiative recombination processes in the surface region having high carrier density, and in the bulk of the medium with a low carrier density. The observed redshift in the PL emission with increasing growth temperature is ascribed to hydrostatic relaxation of the compressive strain, originated because of the lattice parameter as well as the thermal mismatch between the substrate and grown material.¹ Generally, the strain developed by the native defects is hydrostatic nature. In the present study, relaxation of the compressive strain takes place with the formation of a

native defect comprising of V_N . The relaxation of the compressive strain with increasing growth temperature is understood from the red shift of the $A_1(\text{LO})$ phonon mode (Figs. 4.1f–j).

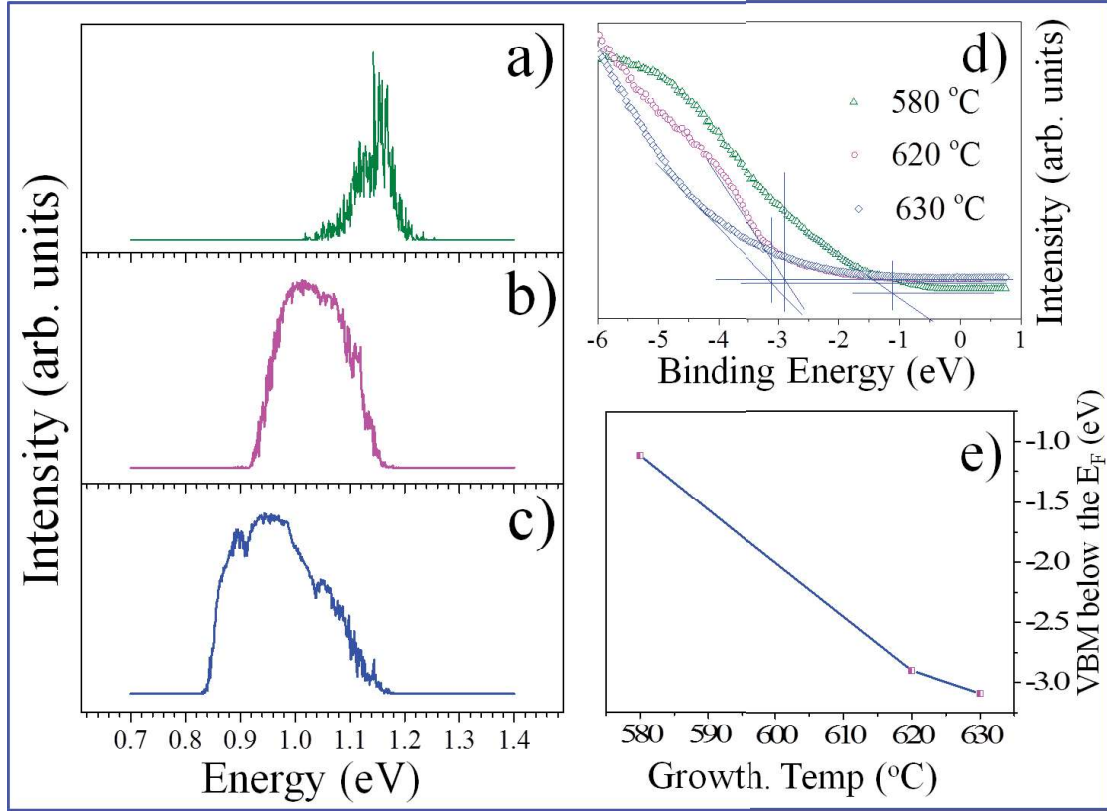


Figure 4.3. PL spectra of the nanostructures grown at (a) 580 (b) 620, and (c) 630 °C. d) VB photoemission spectra of samples grown at 580, 620, and 630 °C. e) Pinning of Fermi level (E_F) into the conduction band shown increasing with increasing growth temperature. Line shown is a guide for the eyes.

For degenerate semiconductors, one can calculate the carrier density of the nanostructures using the BM shift ²⁴

$$\Delta_{BM} = \frac{\hbar^2}{2m_e^*} (3\pi^2 n_e)^{2/3} \dots\dots\dots (4.2)$$

where Δ_{BM} is the energy shift from the original band gap and n_e is the carrier density in the system. The value of the intrinsic band gap and m_e^* of InN is taken as 0.75 eV and 0.052 ($m_e^*=0.06$), and hole effective mass, $m_h^*=0.44$),²⁵ respectively, for

the calculation of carrier density using BM shift of 0.45 eV. The carrier density, n_e , is calculated to be $2.53 \times 10^{19} \text{ cm}^{-3}$ from the BM shift using the equation (4.2). The calculated values of carrier density denote the bulk carrier density. However, one can expect the sheet carrier density to be more than an order of the bulk carrier density in the presence of the SEA,²² which can originate a plasmon peak in the THz frequency.^{16, 21}

On the other hand, PES is a well-established technique for studying the SEA. The UV photoemission spectroscopy (UPS), being a surface sensitive technique, is employed to study the valence band spectra (VBS) of the InN nanostructures for the analysis of the SEA. The VB spectra collected from samples grown at 580, 620, and 630 °C are shown in Fig. 4.3d. The position of VB onset with respect to the E_F is estimated from the intersection of the baseline and extrapolation line of the leading edge of the VB spectrum.²⁶ The positions of the VB onset of samples grown at 580, 620, 630 °C are estimated to be 1.11, 2.90 and 3.09 eV below the E_F , respectively (Fig. 4.3d). However, the VBS of InN are masked (especially for 630 °C grown sample) by the O related emission (~6 eV), which may originate from the Al_2O_3 substrate as the nanostructures are grown non-uniformly on the substrate. It is worth mentioning that we fail to get any signature of In_2O_3 in the Raman studies (Figs. 4.1f–j). The Raman spectroscopy can detect In_2O_3 phase if only significant amount of it coexists with the InN phase. So the role of O in the InN sub-lattice may be ruled out in the VBS of InN nanostructures. However, we recorded a monotonous blue shift of the VB spectra with increasing growth temperature. The shift cannot be related to the presence of O, as the substrate is the same for all the samples. Thus, the blue shift in the VBS for samples grown at different temperatures is essentially a characteristic of InN (Fig.

4.3e). The positions of the VB onset of the samples indicate that the E_F is pinned into the conduction band, as the band gap of InN is found in the range of 0.8–1.1 eV (Figs. 4.3a-c). The pinning of the E_F into the conduction band results in the downward surface band bending with the accumulation of surface electrons in the present samples.

4.3 Excitation Dependent Raman Studies of InN Nanostructures

Excitation-dependent vibrational properties were studied using Raman spectroscopy with various laser wavelengths of 488, 514.5 and 785 nm. Nanostructures grown at 580, 600, 620, and 650 °C were selected for the excitation-dependent study. The Raman spectra of InN nanostructures grown at different temperatures show similar features in the context of peak positions and the asymmetric broadening of the $A_1(\text{LO})$ mode for the high temperature grown samples when excited with 514.5 nm (Fig. 4.4a) and 488 nm (Fig. 4.4b) laser at RT.

However, as compared to other excitations of 514.5 and 488 nm, the RT Raman spectra of InN nanostructures excited with a 785 nm laser show a completely different phonon picture with a considerable broad peak in the range of 440–600 cm^{-1} (Fig. 4.4c). Nonetheless, the lower temperature grown samples still show the tiny peaks corresponding to the symmetry allowed modes of $A_1(\text{TO})$, $E_2(\text{high})$ and $A_1(\text{LO})$, indicated in the spectra by α , β and γ , respectively. An additional broad peak is also observed in the range of 540–560 cm^{-1} (indicated by δ in Fig. 4.4c). A tiny phonon mode in this region is reported by Inushima *et al.*,²⁷ without any assignment while no symmetry allowed Raman mode is reported for wurtzite InN in this frequency range. On the contrary, the forbidden $B_1(\text{high})$ mode of wurtzite InN is reported around 550

cm^{-1} . Additionally, Thakur *et al.*²⁸ also observed a peak in this region with the excitation of 785 nm and assigned it to be the $B_1(\text{high})$ mode; where peak intensity varies with carrier concentration in the system. Thus the broad peak observed in the range of the $540\text{--}560\text{ cm}^{-1}$ is assigned as the $B_1(\text{high})$ mode (Fig. 4.4c). Nevertheless, so far adequate attention has not been devoted in assigning the forbidden $B_1(\text{high})$ mode. In the present study, the appearance of the forbidden mode is attributed to the

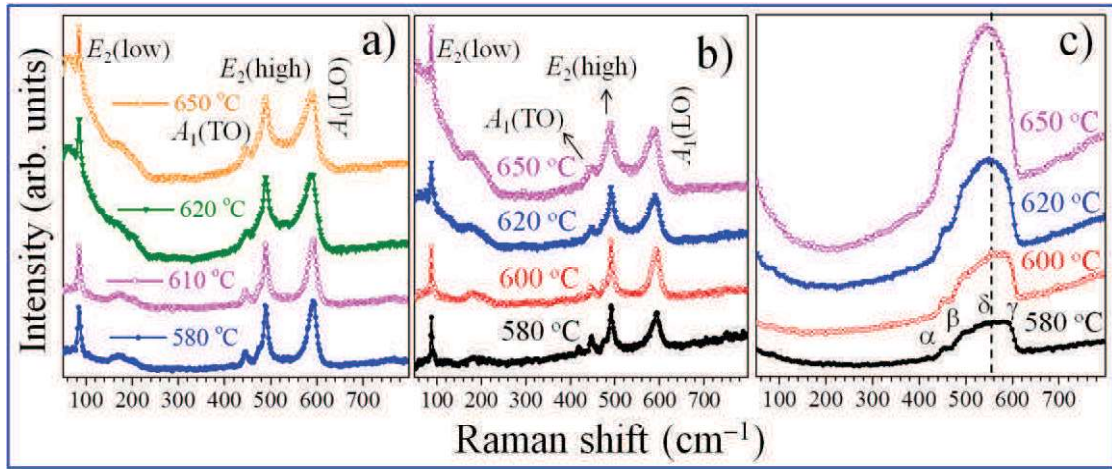


Figure 4.4. Raman spectra collected for samples grown at different deposition temperatures with different laser excitations. a) 514.5 nm: with the higher temperature (620 and 650 °C) grown samples showing the asymmetric broadening of the $A_1(\text{LO})$ phonon mode because of Fano interference. b) 488 nm: showing similar features to the 514.5 nm excitation. c) 785 nm: a broad feature dominating in the range of $440\text{--}590\text{ cm}^{-1}$ with the signature of the symmetry allowed Raman modes at corresponding peak positions of α ($A_1(\text{TO})$), β ($E_2(\text{high})$), and γ ($A_1(\text{LO})$) in addition to the forbidden mode, represented by δ ($B_1(\text{high})$), dominating in the higher temperature grown samples. A dashed vertical line is indicated to show the red shift of the $B_1(\text{high})$ mode with increasing growth temperature.

near- resonance conditions invoking the breakdown of the selection rule.²⁹ However, a structural disorder in the material can also induce the forbidden modes in between the TO and LO modes.³⁰ If the forbidden mode originates because of the structural disorder, then one can expect the same mode to appear in the Raman spectra excited with higher energies (514.5 and 488 nm) also. However, the forbidden mode of

$B_1(\text{high})$ was not observed in the Raman spectra with high energy excitations (Figs. 4.4a and 4.4b). This observation substantiates the fact that the forbidden $B_1(\text{high})$ mode, which appears in the Raman spectrum excited with 785 nm (Fig. 4.4c), is owing to the near-resonance conditions and it is not activated because of disorder in the material.³¹ The peak position and the intensity of the $B_1(\text{high})$ mode are found to vary with the carrier concentration in the samples. As indicated by the dashed vertical line in Fig. 4.4c, for the high-temperature grown samples of 620 and 650 °C, the peak is red-shifted as compared to that for the low temperature grown samples of 580 and

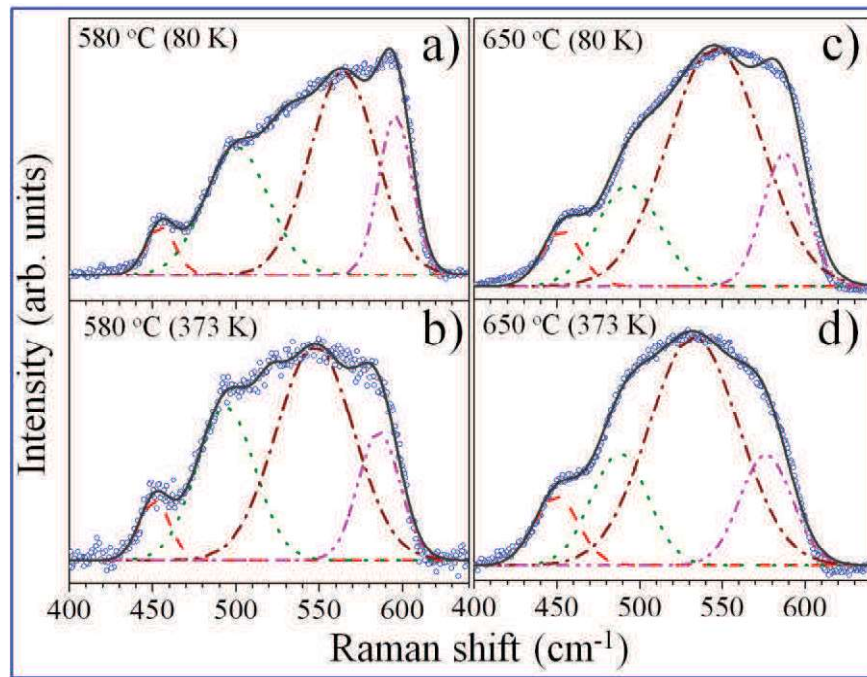


Figure 4.5. Temperature-dependent Raman spectra of InN nanoparticles grown at 580 and 650 °C with Gaussian fitting. Raman spectra collected at (a) 80 K and (b) 373 K for sample grown at 580 °C with the frequency of the forbidden mode at 565 and 544 cm^{-1} respectively. Raman spectra collected at (c) 80 K and (d) 373 K for sample grown at 650 °C with the frequency of the forbidden mode at 552 and 536 cm^{-1} , respectively.

600 °C. Moreover, the peak intensity of the $B_1(\text{high})$ mode is found to be strengthened significantly in the 650 °C grown sample, dominating over the other symmetry allowed Raman modes. The red shift of the $B_1(\text{high})$ mode with the increasing growth

temperature indicates that the phonon mode is strongly dependent on the carrier concentration in the material. The effect of temperature (80–373K) on the resonance induced forbidden $B_1(\text{high})$ mode was also studied using a long working distance 50X

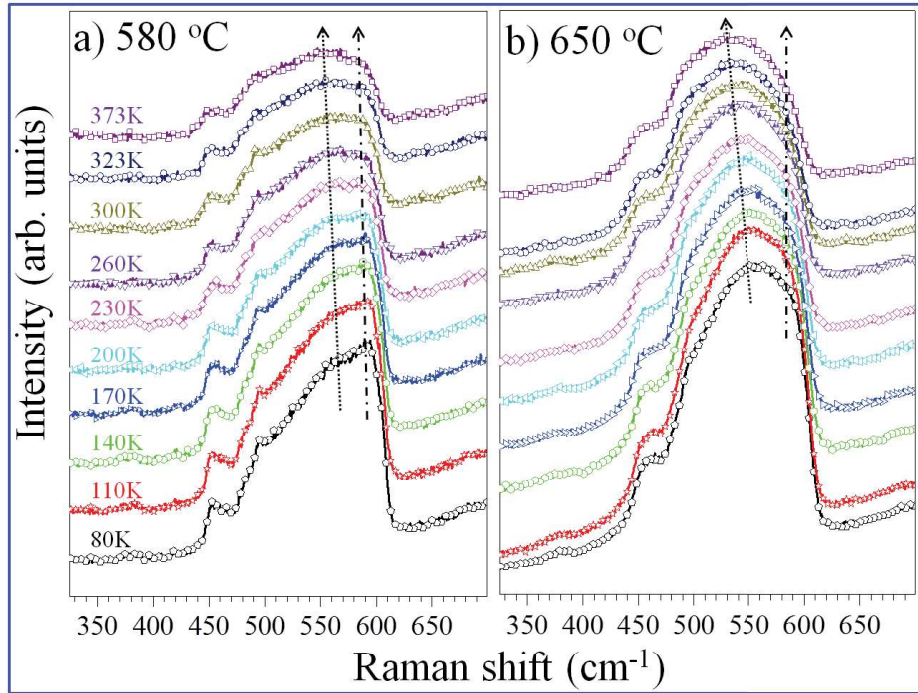


Figure 4.6. Temperature-dependent Raman spectra for (a) Sample grown at 580 °C, with the forbidden mode dominating over the $A_1(\text{LO})$ mode only at higher temperatures and for (b) Sample grown at 650 °C, with the forbidden mode dominating over $A_1(\text{LO})$ mode at all measurement temperatures. The $B_1(\text{high})$ and $A_1(\text{LO})$ phonon modes are indicated by dotted and dash-dotted lines in the both spectra, respectively, for guide to the eye.

objective lens with N.A. of 0.45. The Raman spectrum of the 580 °C grown sample measured at 80 K is shown with proper background correction and after de-convolution using a Gaussian function (Fig. 4.5a). The de-convoluted spectrum shows the forbidden $B_1(\text{high})$ mode at $\sim 565 \text{ cm}^{-1}$.² The ratio of the intensity of the $B_1(\text{high})$ and $A_1(\text{LO})$ phonon modes $[I(B_1(\text{high}))/I(A_1(\text{LO}))]$ was calculated to be 1.26. However, the $B_1(\text{high})$ mode was observed to have red-shifted to $\sim 544 \text{ cm}^{-1}$ for the same sample measured at 373 K (Fig. 4.5b) with a significantly high value of $I(B_1(\text{high}))/I(A_1(\text{LO})) \sim 1.60$. Raman spectra for the high temperature grown (650 °C)

sample at 80 and 373 K are shown in Figs. 4.5c and 4.5d, respectively. The wavenumber of the $B_1(\text{high})$ mode was found to be red-shifted from 552 to 536 cm^{-1} with the increase in temperature from 80 to 373 K. The $I(B_1(\text{high}))/I(A_1(\text{LO}))$ was found to be 1.76 and 1.98 at 80 and 373 K, respectively. In other words, the intensity of the forbidden mode is always stronger than that for the $A_1(\text{LO})$ phonon mode. Interestingly, $I(B_1(\text{high}))/I(A_1(\text{LO}))$ for the sample grown at 650 °C at 80 K was apparent to be stronger than that for the sample grown at 580 °C, at all temperatures (Fig. 4.6).

The variation in the strength of the $B_1(\text{high})$ mode can be explained in terms of carrier density dependent band filling effects. As discussed earlier, the carrier concentration increases as the growth temperature increases. Consequently, electrons are inclined to fill the high electronic levels in the conduction band. Moreover, the E_F level is pinned further into the conduction band, as a result of band filling and it shifts close to the excitation energy. Thus, the resonance conditions become prominent as the E_F approaches the excitation energy of 1.58 eV (785 nm). Consequently, resonance effects are prominent in the higher carrier concentration samples grown at 620 and 650 °C due to the increased proximity of filled levels towards the excitation energy. Thus, the forbidden $B_1(\text{high})$ mode, induced by near-resonance conditions, is more intense in the higher carrier concentration samples grown at 620 and 650 °C than that for samples grown at 580 and 600 °C with lower carrier concentrations.³¹

In order to corroborate the newly observed peak assignment as a forbidden $B_1(\text{high})$ mode, the excitation-dependent Raman studies are further carried out on intentionally doped InN NRs grown using the PAMBE. The n -type doping was carried out using Si. The PL spectra of undoped and Si-doped NRs were shown in the Figs.

4.7a and 4.7b, respectively. There was hardly any emission in the energy region of 1.2-2.3 eV for the undoped InN NRs. The PL emission was, however, observed in the

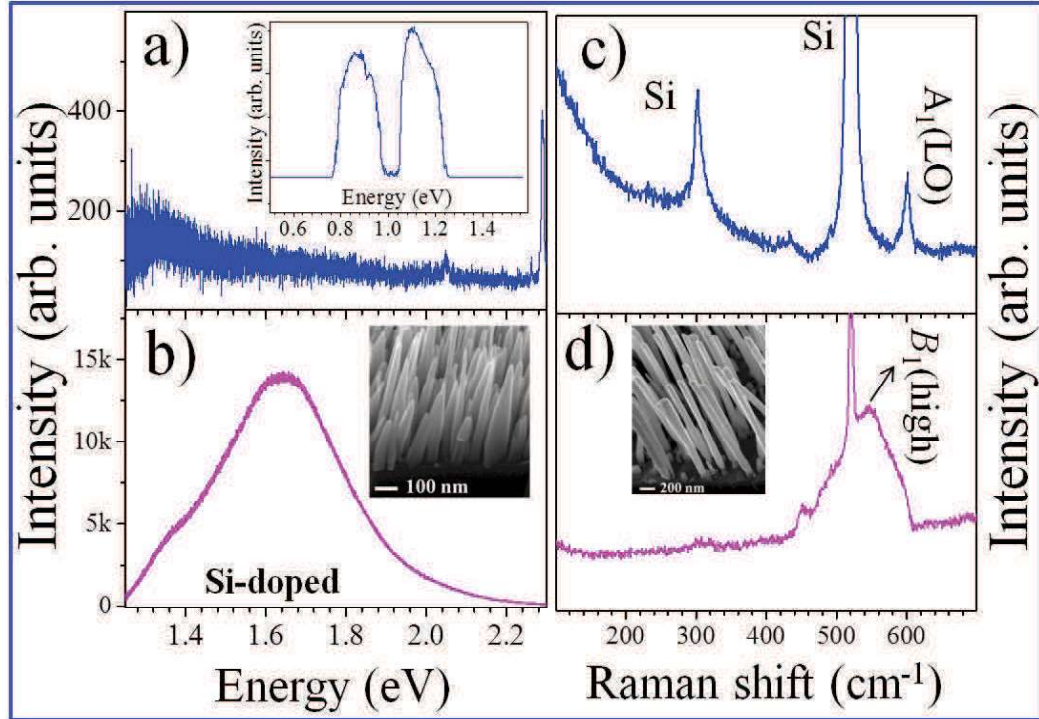


Figure 4.7. a) PL spectrum of undoped InN NRs. Inset shows the NIR PL emission. b) PL spectrum of Si-doped InN NRs. c) Raman spectrum of the undoped InN NRs. d) Raman spectrum of the Si-doped InN NRs. Inset of the figures (c) and (d) shows the morphology undoped and Si-doped InN NRs.

NIR region for these NRs (inset of the Fig. 4.7a). On the contrary, the PL emission was observed in the energy range 1.2-2.3 eV for the Si-doped *n*-type InN NRs (Fig. 4.7b). In other words, PL emission was largely blue-shifted because of the BM effect owing to the *n*-type doping. The Raman spectra of undoped and Si-doped InN NRs excited with 785 nm laser were shown in Figs. 4.7c and 4.7d, respectively. The symmetry allowed $A_1(\text{LO})$ Raman mode, and phonon mode related to Si substrates were observed (Figs. 4.7c) for the undoped NRs. Raman spectrum of Si-doped NRs, however, was distinctly different from the undoped NRs. A broad feature with a peak centered at 540 cm⁻¹ is observed only in case of the Si-doped NRs and the peak is

assigned as the forbidden $B_1(\text{high})$ mode. The observation of the forbidden mode is attributed to resonance Raman condition which is corroborated by the PL emission in the energy range 1.2-2.3 eV (Fig. 4.7c) showing the possible resonance. This observation strongly supports the assignment of newly observed peak as the forbidden $B_1(\text{high})$ mode.

4.4 Conclusion

InN nanoparticles were successfully prepared using an APCVD technique with a self-seeded catalytic approach. Increasing carrier concentration in the samples is achieved by increasing the growth temperature. In case of high-temperature grown InN samples, a peak was observed in the low wavenumber of THz region in the Raman spectra of InN nanostructures originating from excitation of the 2D plasmons of the SEA. The frequency of 2D plasmon peak was observed in the range of 54–60 cm^{-1} ($\sim 1.6\text{--}1.8$ THz). The PL and UPS studies further confirmed the possession of the SEA for the high temperature grown samples. The excitation-dependent vibrational properties of the InN nanoparticles are studied using Raman spectroscopy with different laser sources. Fano interference, instead of plasmon-phonon coupling, is found to dominate in the high carrier concentration samples in the case of $A_1(\text{LO})$ mode using the of 514.5 and 488 nm excitations. Near-resonance excitation, invoking the possible breakdown of the selection rule, induces significant changes in the Raman spectra with the appearance of the forbidden $B_1(\text{high})$ mode. The intensity and frequency of the $B_1(\text{high})$ mode is observed to be strongly dependent on the carrier concentration in the system.

4.5 References

1. C. Kisielowski, J. Krüger, S. Ruvimov, T. Suski, J. Ager III, E. Jones, Z. Liliental-Weber, M. Rubin, E. Weber and M. Bremser, *Phys. Rev. B* **1996**, 54, 17745.
2. A. G. Bhuiyan, A. Hashimoto and A. Yamamoto, *J. Appl. Phys.* **2003**, 94, 2779.
3. S. D. Hersee, X. Sun and X. Wang, *Nano Lett.* **2006**, 6, 1808.
4. I. Mahboob, T. Veal, C. McConville, H. Lu and W. Schaff, *Phys. Rev. Lett.* **2004**, 92, 036804.
5. L. Colakerol, T. D. Veal, H.-K. Jeong, L. Plucinski, A. DeMasi, T. Learmonth, P.-A. Glans, S. Wang, Y. Zhang and L. Piper, *Phys. Rev. Lett.* **2006**, 97, 237601.
6. W. Linhart, J. Chai, R. J. Morris, M. Dowsett, C. F. McConville, S. Durbin and T. D. Veal, *Phys. Rev. Lett.* **2012**, 109, 247605.
7. S. Zhao, S. Fatholouloumi, K. Bevan, D. Liu, M. G. Kibria, Q. Li, G. Wang, H. Guo and Z. Mi, *Nano Lett.* **2012**, 12, 2877.
8. G. Conibeer, D. König, M. Green and J. Guillemoles, *Thin Solid Films* **2008**, 516, 6948.
9. J. Wu, *J. Appl. Phys.* **2009**, 106, 5.
10. K. K. Madapu, S. Dhara, S. Amirthapandian, S. Polaki and A. Tyagi, *J. Phys. Chem. C* **2013**, 117, 21930.
11. K. K. Madapu, S. Dhara, S. Polaki, S. Amirthapandian and A. Tyagi, *CrystEngComm* **2015**, 17, 3139.
12. K. K. Madapu and S. Dhara, *CrystEngComm* **2016**, 18, 3114.
13. X. Wang, S.-B. Che, Y. Ishitani and A. Yoshikawa, *Appl. Phys. Lett.* **2006**, 89, 171907.
14. A. E. Miroshnichenko, S. Flach and Y. S. Kivshar, *Rev. Mod. Phys.* **2010**, 82, 2257.
15. T. Shubina, *Phys. Status Solidi A* **2010**, 207, 1054.
16. T. Shubina, A. Andrianov, A. Zakhar'in, V. Jmerik, I. Soshnikov, T. Komissarova, A. Usikova, P. Kop'ev, S. Ivanov and V. Shalygin, *Appl. Phys. Lett.* **2010**, 96, 183106.
17. D. Olego, A. Pinczuk, A. Gossard and W. Wiegmann, *Phys. Rev. B* **1982**, 25, 7867.
18. G. Fasol, N. Mestres, H. Hughes, A. Fischer and K. Ploog, *Phys. Rev. Lett.* **1986**, 56, 2517.
19. C. G. Van de Walle and D. Segev, *J. Appl. Phys.* **2007**, 101, 081704.
20. S. Allen Jr, D. Tsui and R. Logan, *Phys. Rev. Lett.* **1977**, 38, 980.
21. T. Shubina, N. Gippius, V. Shalygin, A. Andrianov and S. Ivanov, *Phys. Rev. B* **2011**, 83, 165312.
22. T. Veal, L. Piper, W. Schaff and C. McConville, *J. Cryst. Growth* **2006**, 288, 268.

23. Y. L. Chang, Z. Mi and F. Li, *Adv. Funct. Mater.* **2010**, 20, 4146.
24. A. Walsh, J. L. Da Silva and S.-H. Wei, *Phys. Rev. B* **2008**, 78, 075211.
25. K. K. Madapu, A. Sivadasan, M. Baral and S. Dhara, *Nanotechnology* **2018**, 29, 275707.
26. S. A. Chambers, T. Droubay, T. C. Kaspar and M. Gutowski, *J. Vac. Sci. Technol. B Microelectron. Nanometer Struct.* **2004**, 22, 2205.
27. T. Inushima, M. Higashiwaki and T. Matsui, *Phys. Rev. B* **2003**, 68, 235204.
28. J. Thakur, D. Haddad, V. Naik, R. Naik, G. Auner, H. Lu and W. Schaff, *Phys. Rev. B* **2005**, 71, 115203.
29. W. H. Weber and R. Merlin, *Raman scattering in materials science*. (Springer Science & Business Media, **2013**).
30. Y. Cho, M. Ramsteiner and O. Brandt, *Phys. Rev. B* **2012**, 85, 195209.
31. K. K. Madapu, S. Polaki and S. Dhara, *Phys. Chem. Chem. Phys.* **2016**, 18, 18584.

CHAPTER 5

NEAR-FIELD LIGHT-MATTER INTERACTION OF InN NANOSTRUCTURES AND PLASMONIC PROPERTIES

5.1 Introduction

Recently, heavily doped semiconductors have emerged as an alternative to low-loss plasmonic materials. In this context, InN is a degenerate semiconductor and possesses the unique property of surface electron accumulation (SEA), which provides a 2DEG system. In recent times, 2D plasmons in graphene generated much curiosity because of their terahertz (THz) resonance frequency.¹⁻⁵ In the case of 3D plasmonic material; the plasmon frequency (ω_p) is dependent on the carrier density (n) of the system (Equation 5.1).⁶

$$\omega_p = \sqrt{\frac{4\pi n e^2}{\epsilon_e (\epsilon + 2\epsilon_m)}} \dots\dots\dots (5.1)$$

where m_e is the effective electron mass, ϵ is the high-frequency dielectric constant, and ϵ_m is the dielectric function of surrounding medium. On the other hand, ω_p depends on the in-plane wave vector as well as areal carrier density in the case of the 2D plasmonics.⁷⁻⁹ The plasmon frequency of 2DEG is written as

$$\omega_p^2 = \frac{n_s e^2}{m^*} \frac{q}{\epsilon_1 + \epsilon_2 \coth(qd)} \dots\dots\dots (5.2)$$

where n_s is the areal carrier density of 2DEG, m^* the effective mass of electron, ϵ_1 and ϵ_2 are the dielectric constants of the substrate and surrounding media, q is the in-plane wave vector and d is the thickness of the 2D electron system. A 2D plasmon system can also be observed in the semiconductor inversion layers such as Si and GaAs.⁷⁻⁹

Recently, Dirac plasmons have also been observed in the topological insulators because of the downward band bending near the surface region.¹⁰ However, materials such as InAs and InN possess the inherent SEA, which can act as a 2DEG. Among these, InN is reported to possess the higher amount of sheet carrier density as compared to that of InAs. It is worth probing the plasmonic properties of InN with a naturally forming 2DEG for an interesting physics and new applications. The NSOM technique is proven as the major tool for visualizing the localized surface plasmon resonance (LSPR) and the propagation of surface plasmon polaritons (SPP).⁴ Moreover, the momentum mismatch between the SPP and propagating light can be overcome by evanescent field produced by NSOM probes.

Raman scattering cross section is found to be enhanced enormously with the adsorption of analyte molecules on the rough surfaces of noble metals. This phenomenon is called the surface-enhanced Raman scattering (SERS).¹¹ The enhancement of SERS is attributed to the combination of two phenomena comprising of, namely, the electromagnetic mechanism (EM) and chemical mechanism (CM).¹² Large contribution of the enhancement, however, is attributed to the EM and role of the CM is minimal with one-to-two orders of the value.¹¹ The EM exploits the surface plasmon resonance (SPR) phenomenon of noble metal nanoparticles and nano-protrusions. As a consequence of the SPR, electric field near the surface region is enhanced by four orders, and the enhanced field is evanescent in nature. However, SPR is strongly dependent on the excitation frequency, which should closely match with the resonance frequency of free electrons of the nanostructure. Most of the SERS enhancement measurements are carried out on the metallic nanostructures, especially Ag and Au nanoparticles, because of their visible region resonance frequency. In

contrast to EM, CM relies on the charge transfer mechanism which increases molecular polarizability.¹³ However, noble metal nanostructures suffer from their poor structural integrity, bio-compatibility, and cost-effectiveness. Recently, semiconductor nanostructures are being investigated as an alternative to metallic SERS substrates, which includes the metal oxide nanostructures, namely, TiO₂, ZnO, Fe₂O₃, alongside compound semiconductor, e.g., InAs, and elemental semiconductors of Si and Ge.¹³⁻¹⁸ In addition, graphene is also reported as the SERS substrate showing enhancement of one order.¹⁹ Because of the low carrier density in the semiconductors as compared to that for the metals, the frequency of SPR in the former is generally in the IR region.⁶ As a result, SERS enhancement in the semiconductors is expected to be very low in the process of EM. Thus, the SERS enhancement in the semiconductors can be attributed to CM through the charge transfer process.^{18,20,21} In the context of bio-compatibility, III–V nitrides are excellent candidates.²² However, to the best of our knowledge, until now, there are no reports available for III-nitrides as SERS substrates. In this context, it is worth mentioning that, InN shows a unique property of possessing the SEA close to its surface region which may be useful in SERS effect.

Present chapter explores the plasmonic properties of InN nanostructures and subsequently the applicability of the InN nanostructures as SERS substrate. The chapter is divided into two parts. In the first part (Section 5.2), surface plasmon properties of the InN nanostructures is explored using the real-space mapping of the surface plasmon fields with the aid of NSOM technique. For this study, high optical quality InN nanostructures grown at different temperatures using the APCVD technique were selected. The role of the SEA in the plasmonic properties is explicitly discussed. In the second part (Section 5.3), SERS activity of InN nanostructures is

explored. The SERS activity of InN nanostructures is probed using the different laser excitations. In addition, the role of SEA induced 2D plasmons in the enhancement of Raman spectra is probed. The measurements were carried out on the standard SERS analyte of Rhodamine 6G (R6G).

5.2 Near-field Light-matter Interaction of InN Nanostructures

Near-field light-matter interaction of InN nanostructures was studied using the aperture probe NSOM technique. The NSOM studies were carried out on InN nanostructures grown via APCVD technique. The details of the growth procedure were discussed in the previous Chapter 4 (Section 4.2). From the Raman analysis (Section 4.2.2), it was observed that nanostructures grown ≥ 620 °C possessed high carrier density, which was revealed by the asymmetric broadening of the $A_1(\text{LO})$ phonon mode in the Raman spectrum. In contrast, the nanostructures grown below 620 °C have symmetric $A_1(\text{LO})$ phonon mode. It reveals the fact that nanostructures grown below 620 °C possesses low carrier density as compared to the high temperature grown samples.²³ In addition, a 2D plasmon peak was observed in the spectrum of the nanostructure grown ≥ 620 °C possessing the SEA.^{24,25} The PL and UPS studies further confirmed the possession of the SEA in the high temperature grown nanostructures. For the NSOM studies, three InN nanostructure samples were selected, which were grown at 580, 620, and 630 °C. Among these, 580 °C grown sample does not possess the SEA; whereas samples grown at 620 and 630 °C possess the SEA.

5.2.1 NSOM imaging of nanostructures grown at 580 °C

Topographic (Figs. 5.1a–c) and corresponding NSOM images (Figs. 5.1d–f) of the nanostructures are shown for the sample grown at 580 °C. The images (Figs. 5.1a and

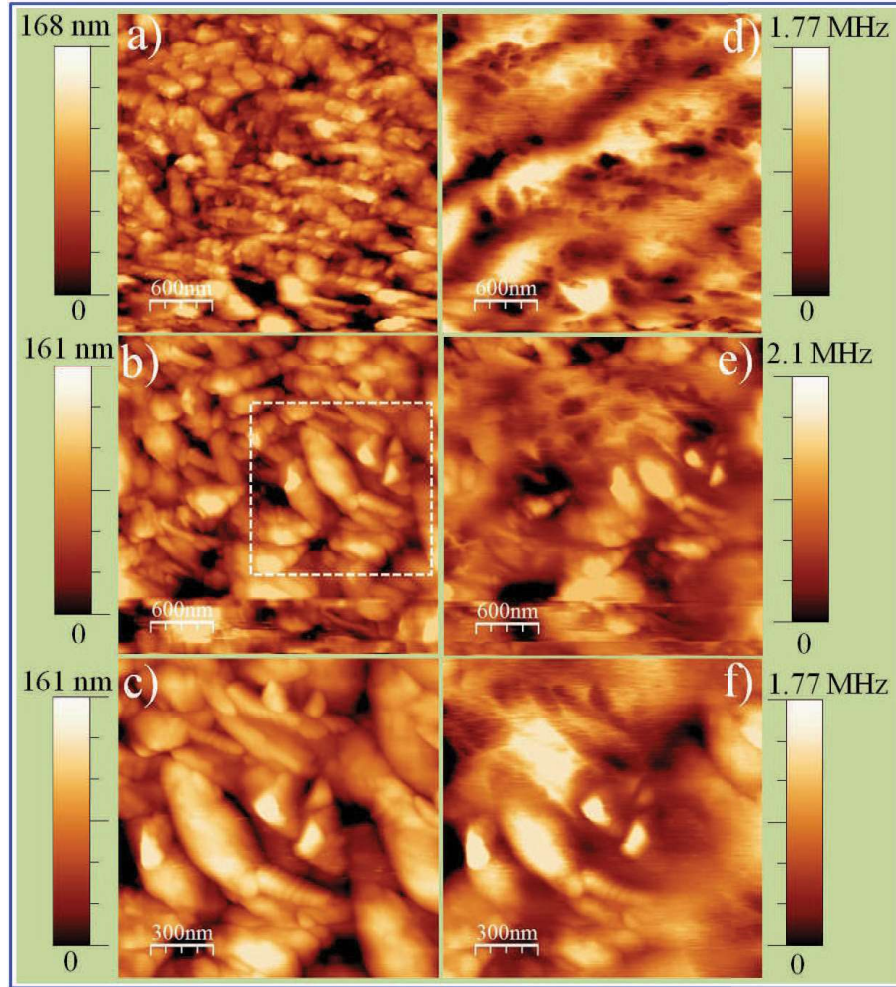


Figure 5.1. (a), (b), (c) Topography of sample grown at 580 °C and the corresponding (d), (e), (f) NSOM images, respectively. c) Zoomed scan of Fig. b (Dashed area). Observed optical contrasts in the NSOM images attributed to variation in the carrier density of individual nanoparticles.

5.1b) correspond to two different areas of the sample. However, the image shown in Fig. 5.1c is the zoomed scan of Fig. 5.1b (dashed area). The scale shown in the NSOM images represents the counts per second of a single photon counter for a given integration time. The topography and NSOM images allow us to directly correlate the optical intensity distribution with the structural image. The observed optical contrasts in the NSOM images are attributed to the intrinsic properties of individual nanoparticles. In the case of scattered-type NSOM with noble metal nanoparticles at

the end of the tip, the image can be understood based on the quasi-static approximation. The amplitude of the scattering intensity depends on the effective polarizability of the tip, which has the contribution from the tip as well as the image dipole in the sample.²⁶ However, in the present case, imaging of the nanostructures is performed using the aperture probe with light emitting from the aperture being considered as the point light source.²⁷ In the aperture case, there is always the same dipole defined by the aperture and the alternations in the contrast are due to changes in the dielectric properties of the sample or with the dipolar angle of a molecule interacting with the constant dipole.²⁸ Thus, one can think that the sample polarizability is the sole reason for the observed optical contrast in the NSOM image and the near-field scattering from the individual nanoparticles depends on the local dielectric function of the sample (ϵ_s). In case of the doped semiconductor, the dielectric function of the sample can be written as $\epsilon_s(\omega) = \epsilon_{opt} + \epsilon_{Drude}$, where ϵ_{opt} is the contribution from bound electrons and ϵ_{Drude} is the Drude's contribution to the dielectric function.²⁹ The Drude part of the dielectric function is attributed to the free carrier density in the system, and the complex dielectric function of the sample can be further written as,

$$\epsilon_s(\omega) = \epsilon_{opt} \left(1 - \frac{\omega_p^2}{(\omega^2 + i\gamma\omega)} \right) \dots\dots\dots (5.3)$$

$$\omega_p^2 = \frac{ne^2}{\epsilon_{opt}\epsilon_o m_e^*} \dots\dots\dots (5.4)$$

where ω is the excitation frequency; ω_p is the plasma frequency which is related to free carrier density (n), and electronic charge (e); ϵ_o is the static dielectric constant and γ is the damping constant.²⁹ The Valence band spectrum (VBS) shows that there is a negligible amount of SEA for the sample grown at 580 °C (Fig. 4.3d) and Raman

spectroscopic study does not show any plasmon related peak (Fig. 4.1f). Thus, sample grown at 580 °C is considered as a lightly doped semiconductor compared to those of samples grown at 620 and 630 °C. The free carrier density available in the system is attributed to the background carrier density instead of the SEA. For simplicity, if we neglect the damping parameter in equation (5.3), the dielectric function is solely dependent on ω_p and ω . In the case of lightly doped semiconductors, ω_p is significantly lower than ω (2.32 eV in the present study). There can be free carrier absorption of light for $\omega > \omega_p$. Thus, the optical contrast in the NSOM images (Figs. 5.1d-f) is attributed to free carrier absorption of the nanoparticles. The contrast in the NSOM images, however, depends on the carrier density of the individual nanoparticles. Nanoparticles, which have high carrier density, show significant absorption due to the available free carriers.²⁹ Thus, with the variation of local carrier density there is a variation in absorption and hence in the scattered light intensities leading to the variation in the optical contrasts of the NSOM images, as it appears in Figs. 5.1d-f. The variation in the intrinsic carrier density is attributed to the local growth conditions, structural defects, chemical impurities and internal strain in the particles.

5.2.2 NSOM imaging of nanostructures grown at 620 °C

Topographic (Figs. 5.2a and 5.2b) and NSOM (Figs. 5.2c and 5.2d) images are shown for sample grown at 620 °C. In contrast to the sample grown at 580 °C, a significant absorption was observed in these nanoparticles. Line profiles of the scattered intensities are shown in Figs. 5.2e and 5.2f. There is a significant enhancement of the electric field intensity surrounding each nanoparticle along with the strong absorption at the same time. In the case of sample grown at 620 °C, the distinct optical contrast in

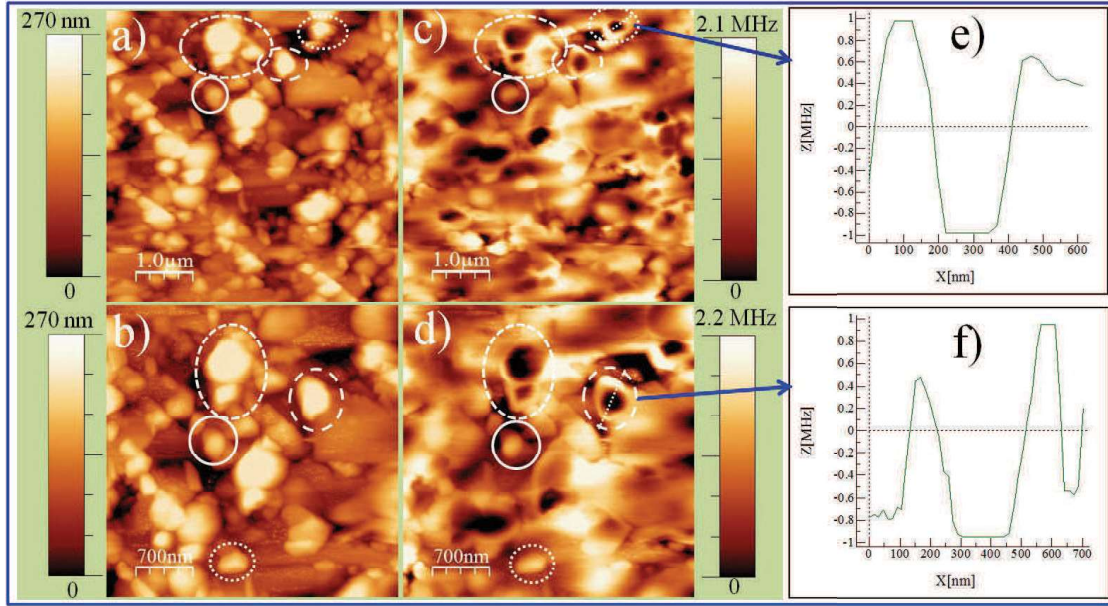


Figure 5.2. (a) Topography and corresponding (c) NSOM images of sample grown at 620 °C. NSOM images showing the strong extinction of the light at some of the nanoparticles and near-field enhancement around them. (b) Zoomed scan of (a) and (d) being the corresponding NSOM image showing similar kind of topography and optical images. Correlated particles in the topography and NSOM images are shown with circles and ellipses. (e) and (f) showing the line profile of scattered intensity across the nanoparticles indicated by the blue arrows.

the NSOM images may be because of strong absorption of the light. Enhancement of the electric field surrounding each nanoparticle is attributed to the resonance kind of behaviour of nanoparticles with the availability of sufficient free carrier density originating from the SEA in the system. The plasmonic behaviour of these nanoparticles is also confirmed by the Raman spectroscopic analysis (Fig. 4.1h). The SEA behaves like absolute free carriers, similar to metals supporting plasmonic features.

5.2.3 NSOM imaging of nanostructures grown at 630 °C

From the VBS of sample grown at 630 °C, the surface sheet carrier density is found to be increased compared to those of samples grown at 580 and 620 °C, as inferred from symmetric broadening of $A_1(\text{LO})$ phonon in Fig. 4.1i. In addition, the plasmon peak in

the Raman spectrum is enormously strengthened because of the increase of surface sheet carrier density in sample grown at 630 °C (Fig. 4.1i). As a result, the surface plasmon effects are expected to be more prominent in sample grown at 630 °C. The topography (Fig. 5.3a) and corresponding NSOM (Fig. 5.3b) images of sample grown at 630 °C, collected at an arbitrary position, are shown. A similar kind of optical contrast is also observed in the case of sample grown at 620 °C (Figs. 5.2c and 5.2d) with near-field enhancement of the electric field leading to prominent absorption around each nanoparticle.

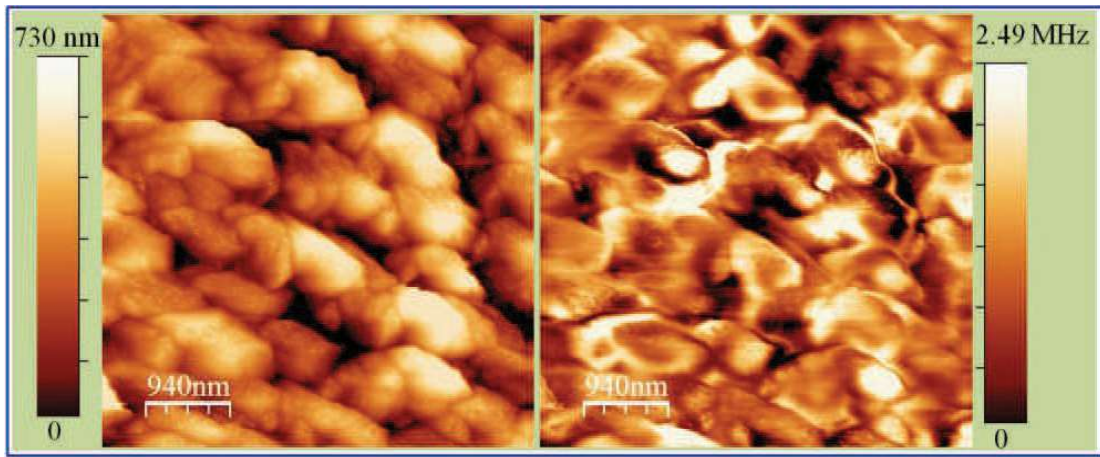


Figure 5.3. (a) Topography and corresponding (b) NSOM images of sample grown at 630 °C. A similar kind of near-field enhancement around each nanoparticle, as in the case of sample grown at 620 °C, is observed in the NSOM image, except for a prominent absorption around the nanoparticles.

Figures 5.4a and 5.4b reveal the topography and corresponding NSOM images of sample grown at 630 °C, respectively, scanned at another arbitrary area. A 3D NSOM image (Fig. 5.4d) is shown corresponding to the 2D image (Fig. 5.4b). However, there is a striking difference between the NSOM images of sample grown at 630 °C compared to the other samples. Periodic fringes are observed at each particle in the NSOM images instead of a resonance kind of behaviour. The observed fringes are attributed to the excitation of the propagating SPPs (wavelength, λ_p).

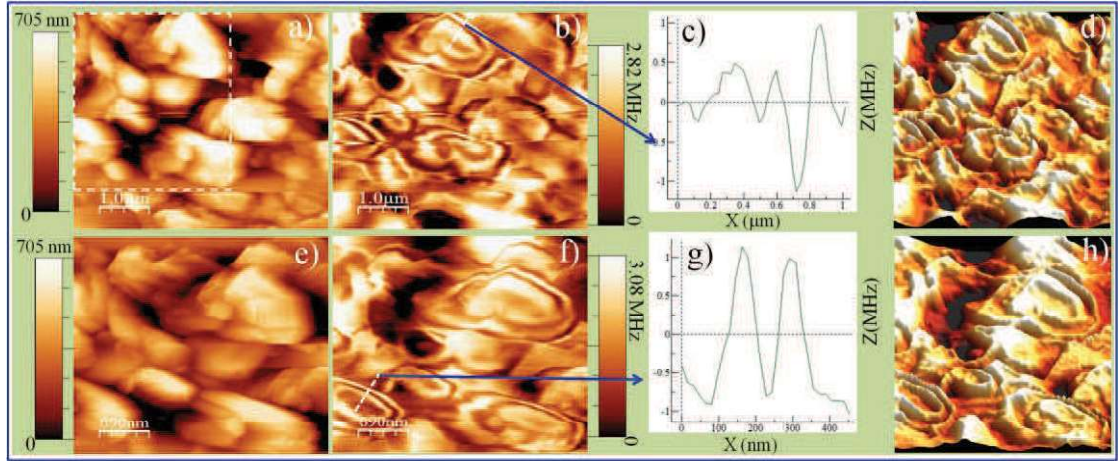


Figure 5.4. (a), (e) Topography and corresponding (b), (f) NSOM images, respectively, for sample grown at 630 °C. (e), (f) Zoomed-in scan of (a), (b); zoomed area is indicated by dashed lines. Periodic fringes are clearly observed because of the interference of the generated and reflected SPPs. (c), (g) Line profiles of the periodic fringes. Collected region is indicated by the blue arrows. (d), (h) 3D images corresponding to (b), (f).

The evanescent field produced by the sub-wavelength aperture excites the SPPs and they propagate towards the edge of the surface where they get reflected back. Thus, the observed fringes may be the result of the interference of the excited and back-reflected SPPs.⁵ Furthermore, the topography of the zoomed scan (dashed area in Fig. 5.4a) is recorded (Fig. 5.4e). Similar kinds of fringes are also observed in the corresponding NSOM image ((Fig. 5.4f) along with its 3D view (Fig. 5.4h). Thus, it may be suggested that the fringes observed in the NSOM images are because of excitation of the SPPs and not from any topography related artefacts. The line profile of the fringes corresponding to selected nanoparticles is shown in the Figs. 5.4c and 5.4g. The periodicity of fringe (δ), which is related to the wavelength of the SPP ($\delta = \lambda_p/2$), is calculated as 250 and 137 nm for Figs. 5.4c and 5.4g, respectively. Thus, the λ_p is calculated as 500 and 274 nm for Figs. 5.4c and 5.4g, respectively. The variation in the SPP wavelength for different nanoparticles is attributed to the variation in the carrier density of individual nanoparticles.³⁰ The origin of the SPPs

must be attributed to the 2DEG of the SEA. This is further corroborated by the observed 2D plasmon peak in the Raman spectra (Figs. 4.1h-j). The 2D nature of the electron gas and very high sheet carrier density are the sole reasons for the observation of the very small SPP wavelengths. There is a similar kind of shortening of the SPP wavelength by around forty times compared to the excitation wavelength reported in the case of graphene.^{4,5} Moreover, in the present case, the possibility of excitation of the SPPs with high excitation energy is attributed to the unique nature of band bending at the InN surface. The surface downward band bending prevails, as the Fermi level (E_F) is pinned into the conduction band. The E_F is pinned at 2.9 eV above the VB maximum near the surface region (Fig. 4.3d) which prevents the inter-band transitions with the excitation of 2.32 eV (532 nm). Moreover, sheet carrier density possesses metallic nature because of the 2D nature of electron accumulation. Finally, the generation and stability of the SPPs are attributed to the 2D plasmonic nature and unique surface band bending. In order to confirm that the fringes observed are because of the wave nature of SPPs, NSOM imaging is further performed in another area of sample grown at 630 °C, which shows the topography (Fig. 5.5a) and corresponding NSOM (Fig. 5.5b) images. However, from the topographic images, it is revealed that nanoparticles are within the clustered regions. Interestingly, the NSOM images show interference fringes between the particles. These fringes are distributed in a way such that bright regions are seen at the edges and dark regions even at the top of the particle where there is the largest height in the topography. Thus, the contrast in the optical image cannot correlate to the topographic height effect of the nanostructures as it shows opposite character. The possible likely explanation is that the SPPs are generated by the cluster of nanoparticles, which acts as a continuous medium. The

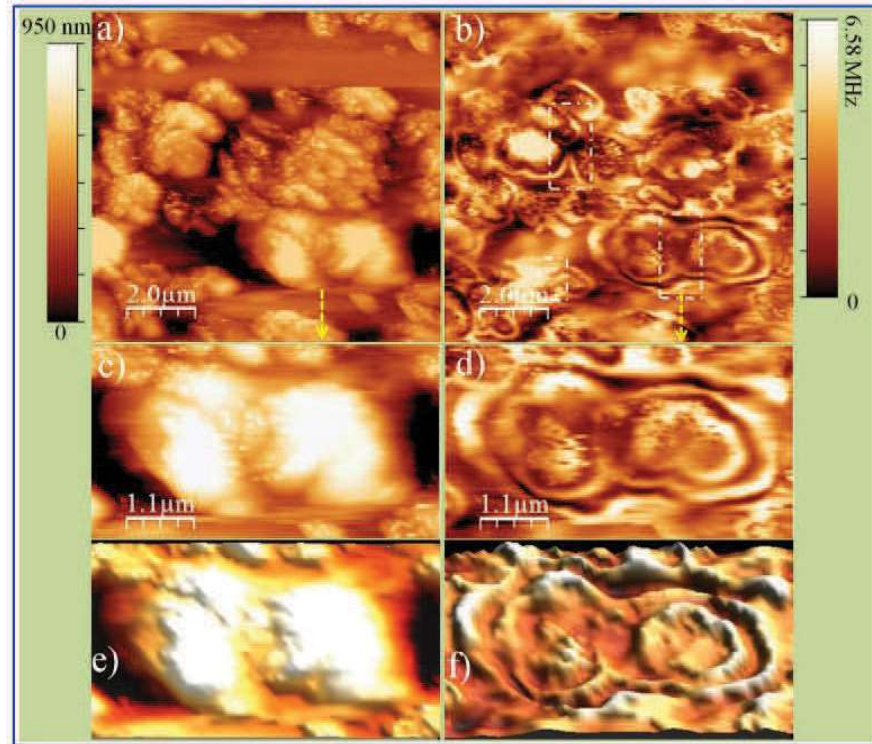


Figure 5.5. (a) Topography and corresponding (b) NSOM images of the nanostructures of grown at 630 °C. Destructive interference of SPPs (in the dash-dotted area) generated by two adjacent InN nanoparticles is clearly observed. (c) Topography and corresponding (d) NSOM images show the zoomed image of the region revealing destructive interference (indicated by arrows). Corresponding 3D images are also shown in the (e) topography and (f) NSOM images.

interaction is clearly supported by the observed destructive interference between the SPPs generated by the two adjacent nanoparticles in the cluster, as shown clearly in the dash-dotted areas ((Fig. 5.5b). In essence, the observation of the destructive interference further confirms that the recorded fringes are because of the SPPs generated by the accumulated surface electrons of InN and is not related to any other phenomena. The zoomed image of one of the regions revealing destructive interference (indicated by an arrow) is shown in the topography (Fig. 5.5c) and corresponding NSOM (Fig. 5.5d) images. Corresponding 3D views are also shown for its topography (Fig. 5.5e) and NSOM (Fig. 5.5f) images. In the present case, even though nanostructures possess SEA, the SPP generation is not observed in every

nanostructure, as observed in the NSOM images of the samples grown >620 °C. In order to support the SPP propagation, the nanostructure must have sufficient plane area on the surface normal to the excitation. In the case of small nanostructures (size $< \lambda_p$), resonance enhancement around the nanoparticles is observed instead of the generation of the SPP (Figs. 5.2 and 5.3). The observation of resonance enhancement is attributed to the existence of localized modes with the surface plasmon wavelength λ_p . Similar kind of resonance enhancement is also observed in the case of the tapered graphene nanostructures.⁴ As a result, we observed the SPP generation in a few of the NSOM images where the nanostructures have sufficient plane area on the surface.

5.3 SERS Activity of InN Nanostructures

SERS activity of the InN nanostructures was explored using the standard SERS analyte such as R6G. For measuring the SERS activity, two samples grown at 580 and 650 °C were selected. Among these, high-temperature grown sample possesses the SEA. The SERS substrate was prepared by a quite simple approach. The Al_2O_3 substrate with InN ($\text{Al}_2\text{O}_3/\text{InN}$) nanostructures grown on it was immersed in the 10^{-3} M R6G solution for a while (1 or 2 s) and subsequently dried under the IR lamp. In the literature, several methods were adopted for the measurement of SERS enhancement factors (EFs).³¹ One of the simple approaches is to collect Raman spectrum in the presence and in the absence of SERS substrate with the same concentration of the analyte and experimental conditions. In the present study, we utilized the unintentionally made scratches on the sample as bare substrate. In other words, Raman spectrum was collected from the area of scratches, where there were no nanostructures and was compared with the Raman spectrum collected from the area with InN nanostructures.

Raman spectrum of the R6G molecules adsorbed on the InN nanostructures grown at 580 °C is shown in Fig. 5.6a. The inset of Fig. 5.6a shows the optical image of the R6G molecules adsorbed on Al₂O₃/InN substrates. The circles in the inset figure represent the area for the collection of Raman spectra. The dashed circle represents the R6G on the bare Al₂O₃ substrate where the continuous circle represents the R6G on InN nanostructures. Raman spectra show the distinct peaks at frequencies of $\nu_1 = 614 \text{ cm}^{-1}$, $\nu_2 = 774 \text{ cm}^{-1}$, $\nu_3 = 1189 \text{ cm}^{-1}$, $\nu_4 = 1309 \text{ cm}^{-1}$, $\nu_5 = 1363 \text{ cm}^{-1}$, $\nu_6 = 1512 \text{ cm}^{-1}$,

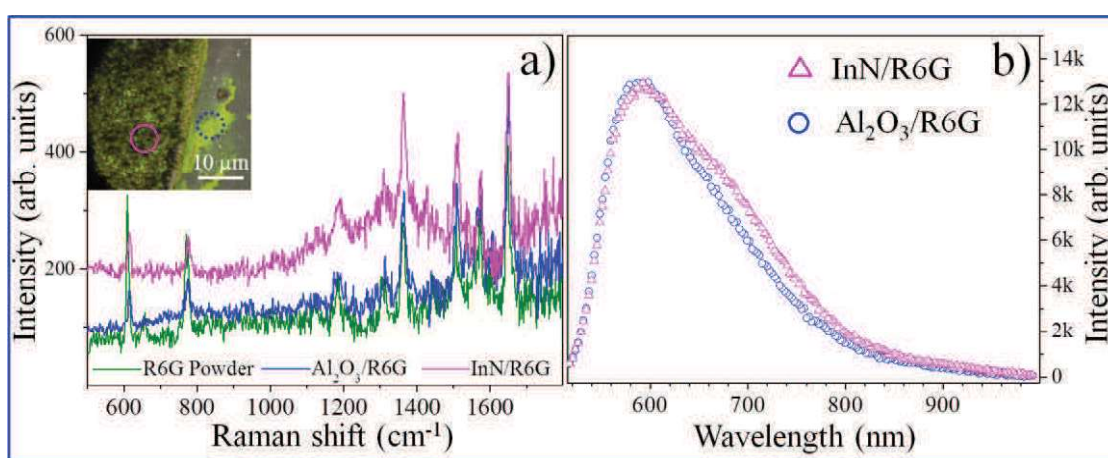


Figure 5.6 a) SERS enhancement studies on InN nanostructures grown at 580 °C. Inset figure shows the optical images of R6G adsorbed substrate with the presence (continuous circle; Al₂O₃/InN/R6G) and the absence (dashed circle; Al₂O₃/ R6G) of nanostructures where the Raman spectra were collected. b) Luminescence band of 10⁻³ M R6G in the presence and the absence of the InN nanostructures.

$\nu_7 = 1574 \text{ cm}^{-1}$ and $\nu_8 = 1651 \text{ cm}^{-1}$. The observed peaks were closely matched with reported values of R6G molecules. While other modes correspond to the aromatic symmetric stretching of the R6G molecule; ν_1 , ν_2 and ν_3 correspond to the C–C–C ring in-plane bending, out-of-plane bending of the H atoms of the xanthene skeleton, and C–C stretching vibrations, respectively.^{32,33} In the present study, Raman enhancement was calculated using the vibrational mode of $\nu_8 = 1651 \text{ cm}^{-1}$. Raman spectrum in case of the sample grown at 580 °C without any SEA shows the same intensity along with

overlap in the spectral features (Fig. 5.6a). Moreover, Raman spectral intensity is almost same for R6G bulk powder (green) and R6G adsorbed on the Al_2O_3 (magenta) in the scratch region. Thus, the interaction volume is same for R6G powder and R6G on Al_2O_3 . It shows the negligible amount of enhancement of the intensity in the presence of the nanostructures grown at 580 °C (Fig. 5.6a). In addition, the luminescence of the R6G molecules is collected in the presence and the absence of the InN nanostructures (Fig. 5.6b), and no enhancement in the luminescence band is observed. A shoulder is observed (Fig. 5.6b) in the luminescence spectrum of R6G molecules on InN nanostructures ~ 620 nm, which is discussed subsequently.

The SERS enhancement of the InN nanostructures grown at 650 °C is further carried out to study the effect of the SEA, as the nanostructures grown at

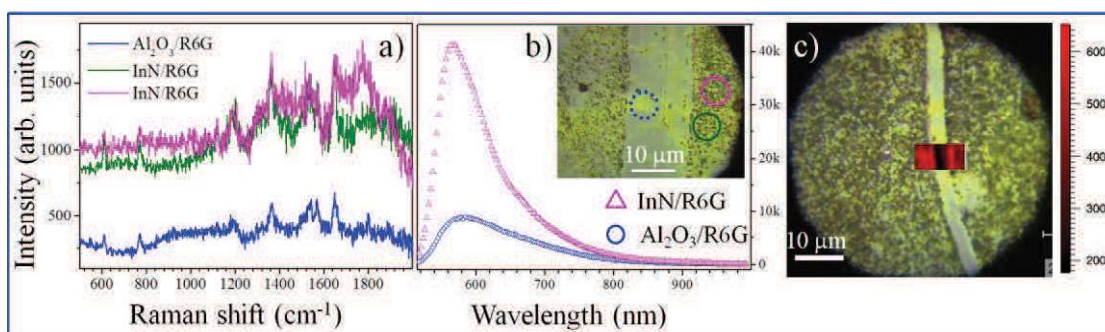


Figure 5.7. SERS and PL enhancement studies on InN nanostructures grown at 650 °C. a) Raman spectra collected in the presence (corresponding to the continuous circle) and the absence (corresponding to the dashed circle) of InN nanostructures. b) Luminescence of R6G molecules in the presence and the absence of InN nanostructures. Inset of (b) shows the area of collection of Raman and PL spectra. c) Intensity mapping of Raman mode $\nu_8 = 1651 \text{ cm}^{-1}$ showing the enhanced intensity in the presence of the InN nanostructures.

≥ 620 °C analyzed to possess prominent SEA (Figs. 4.1h-j). The electrons in the SEA behave like absolute 2DEG. Raman spectra of the R6G molecules adsorbed on the InN nanostructures, grown at 650 °C, are shown in Fig. 5.7a. As compared the InN nanostructures grown at 580 °C, the spectra witness the considerable amount of

enhancement in the presence of InN nanostructures grown at 650 °C. The background correction was carried out using the cubic spline interpolation. The enhancement factor (EF) is calculated using the following equation:

$$EF = \frac{I_{SERS} N_{Normal}}{I_{Normal} N_{SERS}} \dots\dots\dots (5.5)$$

where I_{SERS} is the intensity of a specific Raman mode of R6G; I_{Normal} is the intensity of the same mode of R6G in the absence of SERS substrate; N_{Normal} is number of R6G molecules in the excited volume in case of normal Raman analysis; and N_{SERS} is the number of adsorbed R6G molecules for a single nanostructure with an average size.

The N_{Normal} can be calculated using the effective excitation volume, $V = \pi(D/2)^2 H$; where the diameter of the beam size, $D = 0.4 \mu m$, and H is the effective depth of the focus ($\sim 1 \mu m$). Subsequently, N_{Normal} was calculated using the following equation,

$$N_{Normal} = (V\rho/M)N_A \dots\dots\dots (5.6)$$

where ρ and M are the density (1.26 g/cm^3) and molecular weight (479.02 gm/mol) of the R6G; and N_A is the Avogadro's number. The N_{Normal} is calculated to be $\sim 3.5 \times 10^8$. The N_{SERS} (8.9×10^4) is evaluated using the average surface area of the nanostructures and molecular foot print of the R6G ($\sim 2.2 \text{ nm}^2$) with the assumption of the self-assembled monolayer. However, N_{SERS} depends on the surface coverage of the analyte molecules (mono or multilayer). Because of finite decay length (30 nm) of the enhanced field, the number of layers influenced by the enhanced field is more than one monolayer. The thickness of the monolayer of the R6G molecule is 1.2 nm .³⁴ Thus, the number of layers experience the enhanced field is ~ 25 which is taken into account of N_{SERS} calculation. Here, nanostructures are approximated as spherical

particles with the size of 100 nm for the simplicity of calculation. The calculated EF is $\sim 1.4 \times 10^4$ for the Raman mode of $\nu_8 = 1651 \text{ cm}^{-1}$. In addition, luminescence from the R6G molecules is collected in the presence and the absence of InN nanostructures (Fig. 5.7b) showing enhancement of four times in the luminescence band. Similar to the sample grown at 580°C (Fig. 5.6b), a shoulder peak is also observed in the luminescence spectrum of the present sample with R6G (Fig. 5.7b). Raman intensity is carried out with the excitation of ν_8 in an area which covers the nanostructures depleted region also (Fig. 5.7c) showing enhancement of peak intensity in the presence of nanostructures.

R6G is one of the most frequently used dyes for applications in dye lasers and as a fluorescence tracer. The absorption and luminescence bands of R6G are dependent on the concentration of R6G molecules. This phenomenon is reported for aqueous solutions³⁵ and thin films.³⁴ The absorption and emission properties of R6G can be explained by the exciton model theory. According to the exciton theory, the dye molecule is considered as a point dipole. The dye molecules are configured as monomers (isolated molecules) and aggregate molecules (dimers and trimers). There are two basic dimer configurations such as perfectly sandwiched structure (H-type) and perfectly aligned structure (J-type). The former is characterized by intense absorption and forbidden emission because of dipole selection rules. In addition, the blue shift in the absorption edge is observed as compared to the monomer. The later configuration is fluorescent with a red shift in the absorption and luminescence bands as compared to the monomer. However, the dimer of R6G molecules can be configured with a distorted sandwich structure such as an oblique H-type dimer. This oblique dimer is fluorescent and possesses the characteristics of both H- and J-type

dimer. The emission from the oblique dimer is red shifted as compared to monomer emission and depends on the angle between the transition moments of the dipole. In addition, excimer can also be formed by the association of excited molecule and unexcited molecule. Emission from the adsorbed molecules on the InN nanoparticles

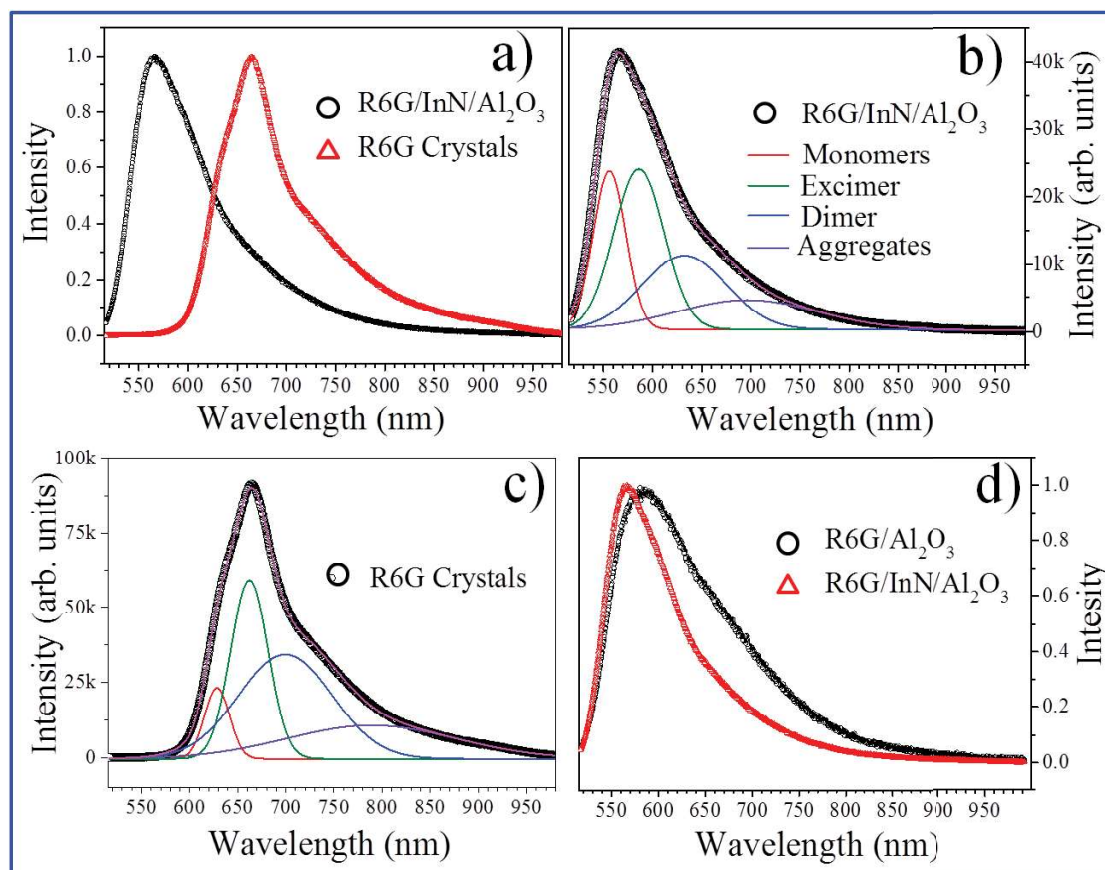


Figure 5.8. a) Normalized emission spectrum of the R6G adsorbed on the InN nanoparticles and R6G bulk crystals. b) and c) de-convoluted emission spectrum of adsorbed R6G on InN nanoparticles and R6G bulk crystals, respectively. The spectra were fitted with the Gaussian curves. d) Normalized emission spectrum of the R6G collected from scratch and nanoparticles area.

is strongly blue-shifted as compared to the bulk crystallites (Fig. 5.8a). The observed shift corroborates to the fact that the adsorbed molecules are not aggregated. Moreover, the emission spectrum of adsorbed molecules is dominated by three main peaks centered at 556, 586, and 632 nm which correspond to monomer, excimer, and dimer,

respectively (Fig. 5.8b). In contrast, the emission spectrum of bulk crystals is dominated by aggregate crystallites cantered around ~ 660 nm (Fig. 5.8c). These observations further confirm that adsorbed molecules are not aggregated. In addition, the emission spectrum collected from the scratch and nanoparticles area shows the negligible amount of shift (Fig. 5.8d).

The SERS measurements are carried out in different areas of the substrates, which also show the similar kind of enhancement. As the absorption edge of R6G (532 nm) is close to the 514.5 nm excitation, the SERS studies are further carried out using the 488 nm laser excitation to avoid the luminescence back ground. In case of 488 nm excitation also, similar kind of enhancement in the Raman spectral intensity is clearly observed (Fig. 5.9).

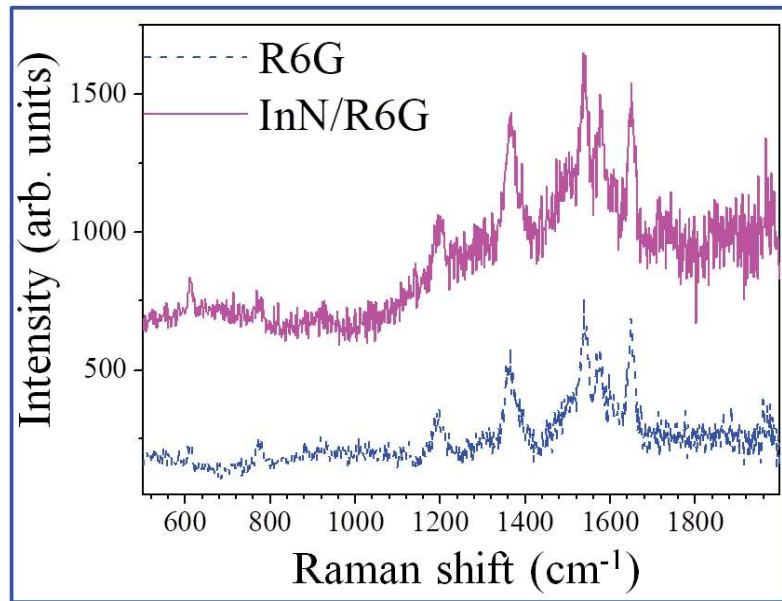


Figure 5.9. SERS studies of InN nanostructures grown at 650 °C with excitation of 488 nm laser.

Usually, SERS enhancement in the Raman spectra is contributed by both EM and CM. The plasmon frequency of the InN nanostructures was calculated using the equation (5.1) for $\epsilon_e = 0.07 \epsilon_0$ and $\epsilon_\infty = 6.7$.³⁶ Carrier density ($n \sim 2.53 \times 10^{19} \text{ cm}^{-3}$) of

InN nanostructures is estimated using the BM shift.²³ The plasmon frequency is calculated as 1968 cm^{-1} , which is far from excitation frequencies ($514.5\text{ nm} \approx 19436\text{ cm}^{-1}$; $488\text{ nm} \approx 20492\text{ cm}^{-1}$), as well as the low-frequency peak observed at $\sim 54\text{ cm}^{-1}$ for high-temperature grown samples (Figs. 4.1h-j). Thus, SPR cannot prevail in these nanostructures, and the role of EM can be ruled out in the enhancement of Raman spectral intensity. In general, SERS enhancement of the semiconductor nanostructures is attributed to the CM. In CM, the charge transfer takes place between the highest occupied molecular orbital (HOMO) levels of adsorbed molecules and lowest unoccupied molecular orbitals (LUMO) to the semiconductor energy levels. The charge transfer is feasible if the semiconductor valence band (VB) and conduction band (CB) levels closely match with the HOMO and LUMO levels of the adsorbed molecule.¹³ In the present case, the R6G molecule has the LUMO and HOMO levels of -4.0 eV and -5.70 eV , respectively.¹⁸ On the other hand, InN is calculated to have the VB of $\sim 0\text{ eV}$ and the CB lies $\sim 0.6\text{--}0.65\text{ eV}$ above the VB.³⁷ These values indicated that charge transfer between R6G and InN may not be favorable because there is no close matching between R6G and InN energy levels. Moreover, in the present study, a variation in Raman spectral intensity enhancement was observed for the nanostructures grown at low ($580\text{ }^{\circ}\text{C}$) and high temperatures ($650\text{ }^{\circ}\text{C}$) (Figs. 5.6 and 5.7a). It reveals that there may be other reason than what it is usually attributed to CM for semiconducting materials. To understand the SERS enhancement, we studied the near-field light-matter interaction of these nanostructures using NSOM probe. NSOM imaging (Fig. 5.10) is carried out with the excitation of 532 nm laser using aperture probe of size 100 nm . Topography (Fig. 5.10a) and NSOM (Fig. 5.10b) image of nanostructures grown at $580\text{ }^{\circ}\text{C}$ show a direct correlation between

morphology and optical image of the sample, respectively. In addition, one can observe the high optical resolution image in NSOM because of the near-field imaging. Similarly, 650 °C grown sample is also studied for topography (Fig. 5.10c) and NSOM image (Fig. 5.10d). In contrast to the near-field optical image of the sample

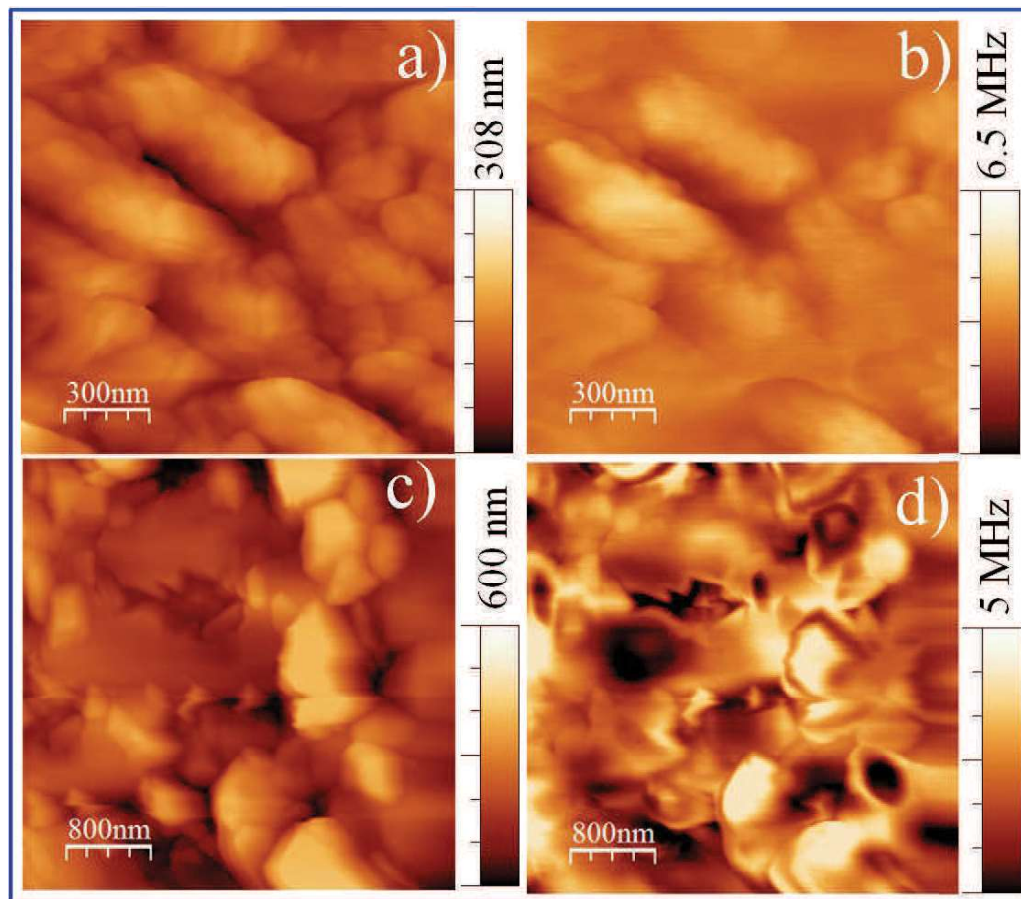


Figure 5.10. Near-field light-matter interaction of InN nanostructures grown at 580 and 650 °C. (a) Topography of InN nanostructures grown at 580 °C and (b) corresponding NSOM image. High magnification (c) topography and (d) NSOM image of InN nanostructures grown at 650 °C.

grown at 580 °C (Fig.5.10b), high magnification NSOM image of 650 °C grown sample (Fig. 5.10d) shows a clear enhancement of the near-field intensity around the nanostructures with the absorption of light. Similar kind of near-field light enhancement was observed for the samples grown ≥ 620 °C (Figs. 5.2, 5.3 and 5.4).

Thus, near-field light-matter interaction analysis reveals that InN nanostructures with SEA show the enhancement for the light intensity in the vicinity of nanostructures.

The observed near-field enhancement of light intensity in the vicinity of nanostructures might be the reason for the SERS enhancement in case of nanostructures grown at 650 °C. However, observed field enhancement cannot be attributed to the SPR of bulk carrier density in the system because 3D plasmon frequency is far from the excitation frequency. The enhancement of light intensity around the nanostructures may be originated because of the excitation of 2D plasmons of the SEA as SPPs, where electrons behave like 2DEG. This argument is corroborated by the observation of the low-frequency peak in the Raman spectra of nanostructures which possesses the SEA. In the present study, Raman measurement conditions readily fulfill the condition of $k_{\parallel}d \ll 1$ for the excitation of 2D plasmons of InN SEA, which is elaborately discussed in the section 4.2.2. The observed enhancement is attributed to 2D plasmon excitation, and the EF is three orders higher than that for graphene sample.¹⁹ The EF value is also found to be higher by one-to-two orders higher than that for some of the oxide-based semiconducting substrates.¹³ The observed EF value, however, is substantially lower than the best values reported for 3D plasmons using noble metal nanostructures.³³ The SERS enhancement of noble metal nanoparticles is originated as confinement of light is smaller than the diffraction limit owing to LSPR and subsequent field enhancement. Similarly, confinement of light also prevails in case of SPPs. However, confinement of light due to LSPR is expected to be very high because of the small size of metal nanoparticles ($a \ll \lambda$, where ‘ a ’ is the size of the nanoparticles and λ is the excitation wavelength). Moreover, the decay length of SPP is in the order of $\lambda/3$ – $\lambda/5$. Thus, the confinement of

light also has the same order and subsequently the field enhancement is expected to be low. In addition, a significant amount of total electric field energy of SPP mode resides inside the conductor. These are the factors which can be the reason for the observed modest enhancement in the Raman spectra of the 2D plasmon. The low frequency of SPP as well as a semiconducting absorbing medium also might be the reason for the moderate enhancement in the present case.

5.4 Conclusion

Plasmonic properties of InN nanostructures were explored by the real-space imaging of the surface plasmons using NSOM technique. The plasmonic properties of InN are attributed to the 2DEG of the SEA. Samples with the presence of SEA show a resonance kind of behaviour demonstrating the near-field enhancement of light, as well as the propagating SPPs in NSOM images. The wavelength of the SPPs, generated by the InN nanoparticles, is estimated to be in the range of 274–500 nm. Shortening of the SPP wavelength is attributed to the 2D nature of the electron gas in the SEA. Thus, InN can be a potential plasmonic material in the THz plasmonic region, for which plasmonic properties can be tailored using the variation of carrier density in the SEA. Well-organized InN nanostructures can even be utilized in sub-wavelength photonic devices.

The SERS activity of InN nanostructures is explored using the Rhodamine 6G molecules. InN nanostructures with SEA show the considerable enhancement in the Raman spectral intensity. The enhancement factor is calculated to be $\sim 1.4 \times 10^4$. The SERS enhancement is attributed to the excitation of the 2D plasmons of 2DEG corresponding to the SEA of InN rather than the 3D surface plasmon resonance of noble metal nanostructures as well as the chemical mechanism of semiconducting

substrates. The observed moderate enhancement factor is attributed to the large decay length of SPP and subsequent small confinement of light in contrast to LSPR. Results indicate that materials with the SEA, namely, InN and InAs can also be used as the semiconductor SERS substrates.

5.5 References

1. Z. Fei, G. O. Andreev, W. Bao, L. M. Zhang, A. S. McLeod, C. Wang, M. K. Stewart, Z. Zhao, G. Dominguez and M. Thiemens, *Nano Lett.* **2011**, 11, 4701.
2. L. Ju, B. Geng, J. Horng, C. Girit, M. Martin, Z. Hao, H. A. Bechtel, X. Liang, A. Zettl and Y. R. Shen, *Nat. Nanotechnol.* **2011**, 6, 630.
3. F. H. Koppens, D. E. Chang and F. J. Garcia de Abajo, *Nano Lett.* **2011**, 11, 3370.
4. J. Chen, M. Badioli, P. Alonso-González, S. Thongrattanasiri, F. Huth, J. Osmond, M. Spasenovi , A. Certeo, A. Piquer and P. Odiro , *Nature* **2012**, 487, 77.
5. Z. Fei, A. Rodin, G. Andreev, W. Bao, A. McLeod, M. Wagner, L. Zhang, Z. Zhao, M. Thiemens and G. Dominguez, *Nature* **2012**, 487, 52.
6. J. M. Luther, P. K. Jain, T. Ewers and A. P. Alivisatos, *Nat. Mater.* **2011**, 10, 361.
7. S. Allen Jr, D. Tsui and R. Logan, *Phys. Rev. Lett.* **1977**, 38, 980.
8. D. Olego, A. Pinczuk, A. Gossard and W. Wiegmann, *Phys. Rev. B* **1982**, 25, 7867.
9. G. Fasol, N. Mestres, H. Hughes, A. Fischer and K. Ploog, *Phys. Rev. Lett.* **1986**, 56, 2517.
10. P. Di Pietro, M. Ortolani, O. Limaj, A. Di Gaspare, V. Giliberti, F. Giorgianni, M. Brahlek, N. Bansal, N. Koirala and S. Oh, *Nat. Nanotechnol.* **2013**, 8, 556.
11. E. Le Ru and P. Etchegoin, *Principles of Surface-Enhanced Raman Spectroscopy: and related plasmonic effects*. (Elsevier, **2008**).
12. M. Moskovits, *J. Raman Spectrosc.* **2005**, 36, 485.
13. X. Wang, W. Shi, G. She and L. Mu, *Phys. Chem. Chem. Phys.* **2012**, 14, 5891.
14. L. G. Quagliano, *J. Am. Chem. Soc.* **2004**, 126, 7393.
15. A. Musumeci, D. Gosztola, T. Schiller, N. M. Dimitrijevic, V. Mujica, D. Martin and T. Rajh, *J. Am. Chem. Soc.* **2009**, 131, 6040.
16. Y. Wang, W. Ruan, J. Zhang, B. Yang, W. Xu, B. Zhao and J. R. Lombardi, *J. Raman Spectrosc.* **2009**, 40, 1072.
17. N. C. Lindquist, P. Nagpal, K. M. McPeak, D. J. Norris and S.-H. Oh, *Rep. Prog. Phys.* **2012**, 75, 036501.

18. W. Ji, B. Zhao and Y. Ozaki, *J. Raman Spectrosc.* **2016**, 47, 51.
19. X. Ling, L. Xie, Y. Fang, H. Xu, H. Zhang, J. Kong, M. S. Dresselhaus, J. Zhang and Z. Liu, *Nano Lett.* **2009**, 10, 553.
20. X. Wang, W. Shi, G. She and L. Mu, *J. Am. Chem. Soc.* **2011**, 133, 16518.
21. M. Mohammadpour and Z. Jamshidi, *J. Phys. Chem. C* **2017**, 121, 2858.
22. P. Sahoo, S. Suresh, S. Dhara, G. Saini, S. Rangarajan and A. Tyagi, *Biosens. Bioelectron.* **2013**, 44, 164.
23. K. K. Madapu, S. Polaki and S. Dhara, *Phys. Chem. Chem. Phys.* **2016**, 18, 18584.
24. K. K. Madapu and S. Dhara, *Appl. Phys. A* **2018**, 124, 435.
25. K. K. Madapu, A. Sivadasan, M. Baral and S. Dhara, *Nanotechnology* **2018**, 29, 275707.
26. F. Keilmann and R. Hillenbrand, *Phil. Trans. R. Soc. Lond.* **2004**, 362, 787.
27. X. Ren, A. Liu, C. Zou, L. Wang, Y. Cai, F. Sun, G. Guo and G. Guo, *Appl. Phys. Lett.* **2011**, 98, 201113.
28. E. Betzig and R. J. Chichester, *Science* **1993**, 262, 1422.
29. M. Fox, *Optical Properties of Solids* (New York: Oxford University Press, **2001**)
30. Z. Fei, M. Goldflam, J.-S. Wu, S. Dai, M. Wagner, A. McLeod, M. Liu, K. Post, S. Zhu and G. Janssen, *Nano Lett.* **2015**, 15, 8271.
31. E. Le Ru, E. Blackie, M. Meyer and P. G. Etchegoin, *J. Phys. Chem. C* **2007**, 111, 13794.
32. P. Hildebrandt and M. Stockburger, *J. Phys. Chem.* **1984**, 88, 5935.
33. S. Nie and S. R. Emory, *Science* **1997**, 275, 1102.
34. M. Chapman, M. Mullen, E. Novoa-Ortega, M. Alhasani, J. F. Elman and W. B. Euler, *J. Phys. Chem. C* **2016**, 120, 8289.
35. F. M. Zehentbauer, C. Moretto, R. Stephen, T. Thevar, J. R. Gilchrist, D. Pokrajac, K. L. Richard and J. Kiefer, *Spectrochim. Acta, Part A* **2014**, 121, 147.
36. K. K. Madapu, N. R. Ku, S. Dhara, C. P. Liu and A. K. Tyagi, *J. Raman Spectrosc.* **2013**, 44, 791.
37. I. Mahboob, T. Veal, L. Piper, C. McConville, H. Lu, W. Schaff, J. Furthmüller and F. Bechstedt, *Phys. Rev. B* **2004**, 69, 201307.

CHAPTER 6

WORK FUNCTION MEASUREMENTS OF InN NANOSTRUCTURES

6.1 Introduction

It is well-known that work function values of semiconductors are dependent on the doping level.¹ Recently, quality of InN phase is enormously improved with controlled growth techniques such as the MBE.²⁻⁵ As a result, the physical properties of InN are having been established. The reports on the work function values of InN are scarce. In addition, it is well known that InN possesses the surface electron accumulation (SEA) close to the surface region because of its narrow band gap. As a result of the SEA, the downward band bending is observed close to the surface region. The 2DEG is formed along the surface because of downward surface band bending (E_{SBB}).^{3,6-8} Thus, it is very important to study the work function values of InN because of its degenerate nature and possession of the SEA. The work function can be measured by various techniques such as Kelvin probe (KP), photoelectron spectroscopy (PES), and from the analysis of electron beam induced current (EBIC) in scanning electron microscopy (SEM). In KP method, contact potential difference (CPD) is measured by nullifying the current between the periodically vibrating parallel plate capacitor. The measured CPD in KP method corresponds to the whole area of the sample. The spatial resolution of the KP method can be enormously increased using the Kelvin probe force microscopy (KPFM), where it exploits the AFM technique. The KPFM measures the CPD between the conductive AFM tip and the sample surface.¹ The CPD is defined as,^{9,10}

$$CPD = \frac{\phi_{tip} - \phi_{sample}}{-e} \dots\dots\dots (6.1)$$

where ϕ_{tip} and ϕ_{sample} are the work functions of the tip and sample, respectively; and e is the elementary charge. However, the CPD is strongly influenced by surface parameters such as adsorbed species and oxide layers. It is straightforward to estimate the work function of metals using the CPD by considering parallel plate capacitor. However, in the case of semiconductors, the CPD is related to the surface potential rather than work function because of space-charge-layer on the semiconductor surfaces. The parallel plate capacitor model can be assumed when the tip radius of curvature is significantly larger than the tip-sample distance. In the ambient conditions, the typical tip-sample distance is in the range of 20-30 nm. However, under the ultra-high vacuum conditions, the tip-sample distance can be as small as ~ 1 nm. In the present study, the radius of curvature of the Si cantilever probe is 25 nm. With these conditions, one can safely assume the parallel plate capacitor model. In addition, the accuracy of the measured CPD values depends on the size of the tip. In the amplitude modulation (AM)-KPFM, for small radii tip, an electrostatic force is dominated by the cone of the tip. Whereas electrostatic force is dominated by the end of the tip for large radii tip. The CPD values measured for features with a size larger than the tip radius is more accurate as compared to the features with the smaller size.

In the present chapter, the KPFM measurements were carried out on one of the best quality undoped and Si-doped InN nanorods (NRs) for establishing the work function of them. Role of the NR size on the measured CPD and subsequent work function values are explicitly discussed. The size-dependent work function of InN NRs is reported, and the role of downward E_{SBB} is discussed.

6.2 Raman and PL Spectroscopic Studies

InN NRs were grown on Si substrates using plasma-assisted molecular beam epitaxy (PAMBE). The *n*-type doping was carried out at the growth temperature of 475 °C for the 4 hr by maintaining the Si beam equivalent pressure of 5.8×10^{-9} mbar. In addition, undoped InN NRs were also grown at the same temperature with growth time of 2 hr.¹¹

The Raman spectrum of the undoped InN NRs using 514.5 nm excitation shows (Fig. 6.1a) the symmetric $A_1(\text{LO})$ ($\sim 592 \text{ cm}^{-1}$) and sharp $E_2(\text{high})$ ($\sim 489 \text{ cm}^{-1}$) phonon modes. In addition to these modes, $A_1(\text{TO})$ ($\sim 438 \text{ cm}^{-1}$) and $E_2(\text{low})$ ($\sim 85 \text{ cm}^{-1}$) phonon modes are also observed. The observed phonon modes correspond to the symmetry allowed Raman modes of wurtzite phase of InN.¹² The sharp $E_2(\text{high})$ phonon mode reveals that InN NRs have high crystalline quality. In contrast, the Raman spectrum of the Si-doped InN NRs (Fig. 6.1b) is distinct from the Raman spectrum of undoped NRs, especially for the line shape of $A_1(\text{LO})$ phonon mode. Usually, the asymmetric broadening of $A_1(\text{LO})$ phonon mode is originated because of Fano interference between the free carriers and longitudinal optical (LO) phonon modes through the Fröhlich interaction.¹² The Fano line shape, observed only in case of the Si-doped InN NRs, is attributed to the increased carrier density because of Si doping. The $E_2(\text{high})$ mode is also found to be broadened (Fig. 6.1b), which may be because of doping related defect formation in the sample.

The PL spectrum of the ensemble undoped InN NRs is shown in Fig. 6.1c. There is no emission observed in the energy range of 1.2-1.6 eV. However, the PL spectrum of the undoped InN NRs shows two peaks in the NIR energy range of 0.5-1.4 eV (inset of the Fig. 6.1c). The observed two peaks in the PL spectrum are

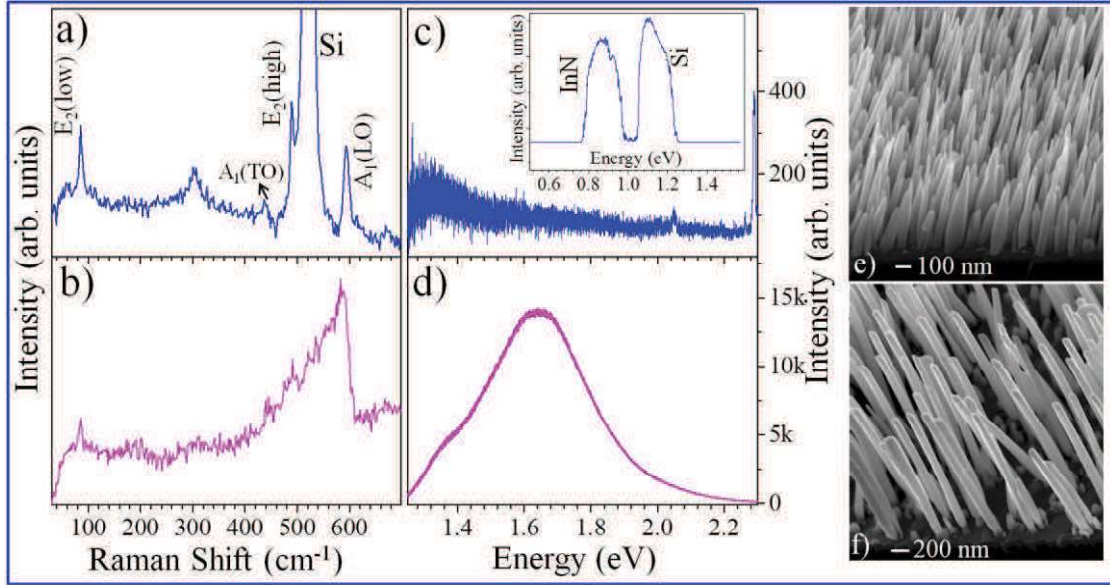


Figure 6.1. Raman spectra of (a) undoped and (b) Si-doped InN NRs. PL spectra of (c) undoped and (d) Si-doped InN NRs. Inset of (c) shows the NIR PL emission of the undoped InN NRs. e) and f) show the scanning electron microscopic images of undoped and Si-doped NRs.

attributed to the emission from the InN NRs (~ 0.87 eV) and Si substrate (1.12 eV). The PL emission from the InN NRs is slightly blue-shifted as compared to the reported band edge emission (~ 0.75 eV) from the InN.¹² The observed blue shift may be attributed to the Burstein-Moss (BM) shift because of unintentional doping. The AFM topography shows that the size of the undoped NRs is in the range of the 10-24 nm (Fig. 6.2). A broad emission peak centered at around 1.64 eV is observed in the PL spectrum of ensemble Si-doped InN NRs (Fig. 6.1d). The PL emission is significantly blue-shifted from the reported band edge emission of InN (0.75 eV). The large blue shift in the PL emission is attributed to the BM shift because of increased carrier density with Si doping. Since the position of the PL emission is greater than the band gap of InN, E_F may be pinned to the conduction band resulting into a downward surface band bending near surface region with the possession of the SEA. The carrier density of the Si-doped InN NRs is estimated to be $\sim 4.5 \times 10^{19} \text{ cm}^{-3}$ using the BM

shift (equation 4.2). In addition, the size of the Si-doped InN NRs is increased as compared to the undoped NRs with the sizes in the range of 50-250 nm (Fig. 6.1f).

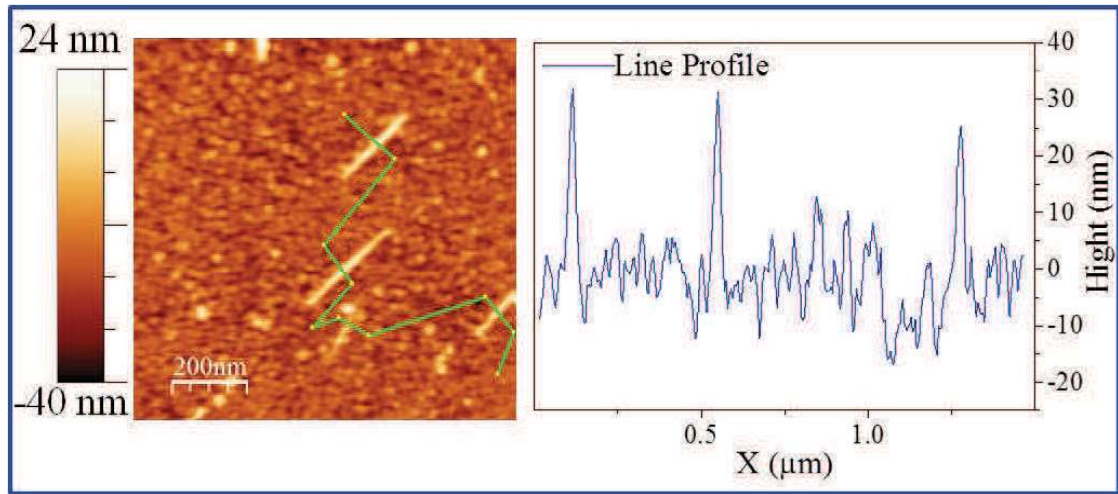


Figure 6.2. Typical AFM topography images of undoped InN NRs and corresponding line profiles.

6.3 Kelvin Probe Force Microscopy Study of InN Nanostructures

6.3.1 KPFM measurements on undoped InN nanorods

KPFM measurements were carried out in high vacuum conditions ($\sim 7.5 \times 10^{-7}$ mbar) in order to avoid substantial surface contamination. For the KPFM measurements, the NRs were mechanically transferred to electron-beam deposited Au film. The CPD maps of the undoped InN NRs were depicted in Fig. 6.3. Because of the small size of NRs, 10-24 nm (Figs. 6.2 and 6.3), the CPD values might be strongly influenced by the Au film. As a result, a poor signal to noise ratio is recorded in the CPD maps providing negligible information of undoped NRs. The size-dependent CPD values and corresponding work function values are plotted in Fig. 6.4. The work function values of undoped InN NRs are in the order of Au film.

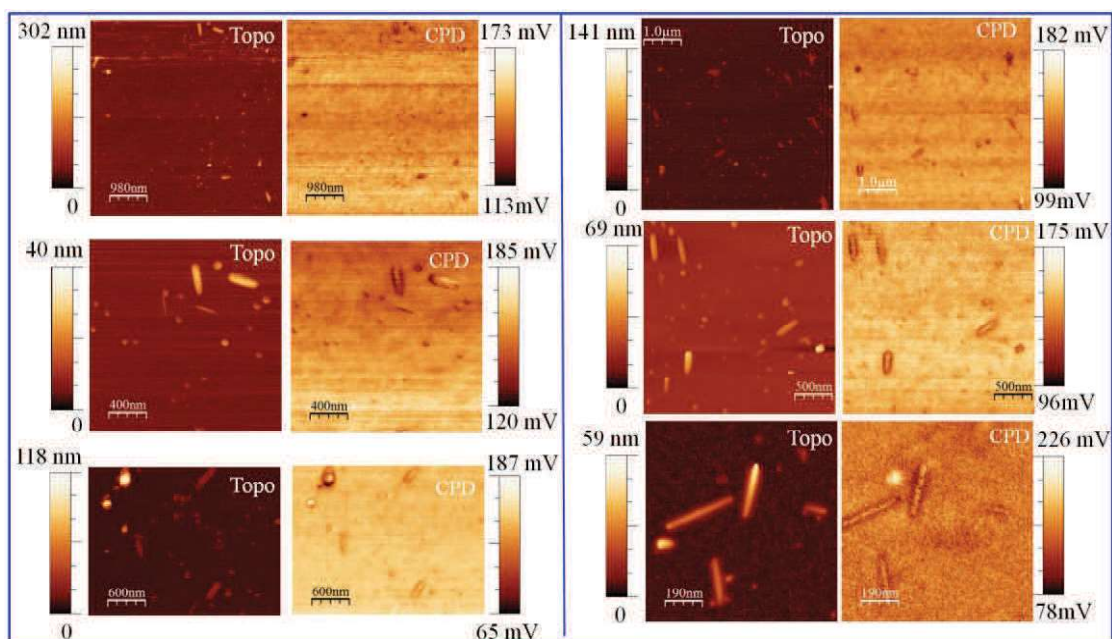


Figure 6.3. Topography and corresponding CPD maps of undoped NRs carried out at different areas of the substrates.

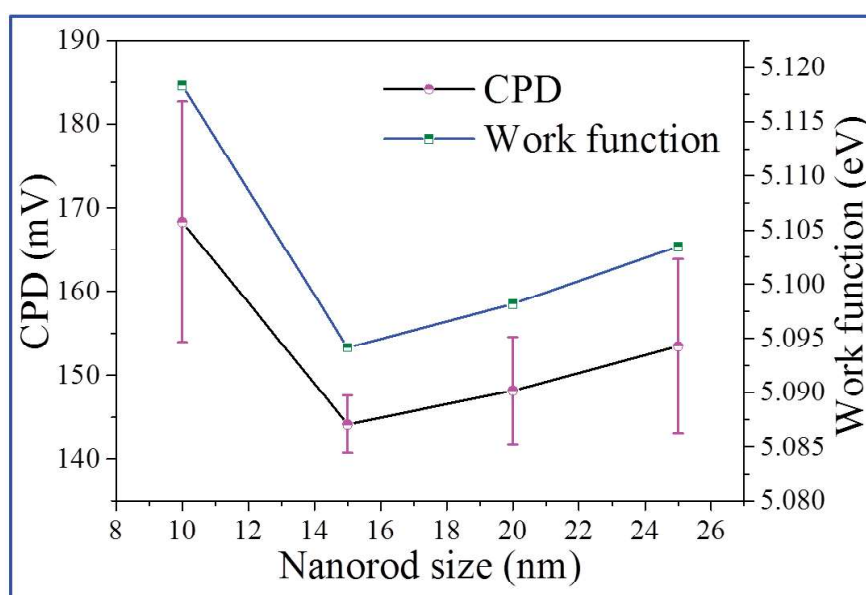


Figure 6.4. Size-dependent CPD values (right Y-axis) and corresponding calculated work function values (left Y-axis) for undoped InN NRs.

6.3.2 KPFM measurements on Si-doped InN nanorods

The topography (Figs. 6.5a-d) and corresponding CPD maps (Figs. 6.5e-h), are shown for Si-doped InN NRs. A clear one-to-one correlation is observed in the topography

and the CPD images. As mentioned in the previous section, the topography images reveal the fact that there is a large dispersion in the size of the NRs. Interestingly, the CPD maps of the NRs also show the variation in contrast. Thus, the variation in the CPD values must be originated because of the change in position of the E_F or work function for different NRs. We carried out the statistical analysis to obtain the size-dependent CPD values. Nearly isolated NRs are selected for measuring the CPD values to avoid the effect of proximity of NRs. The CPD values are averaged against the size of the NRs. Subsequently, the average CPD values of NRs were plotted against the size of the NRs (Fig. 6.6, right Y- axis).

The CPD values of NRs decrease as the size of the NRs is increased. The work function values are calculated using the equation (6.1) and plotted in the Fig. 6.6 (left Y-axis). The parallel plate capacitor is assumed for the estimation of work function values using the CPD values of degenerate InN NRs. The work function values are

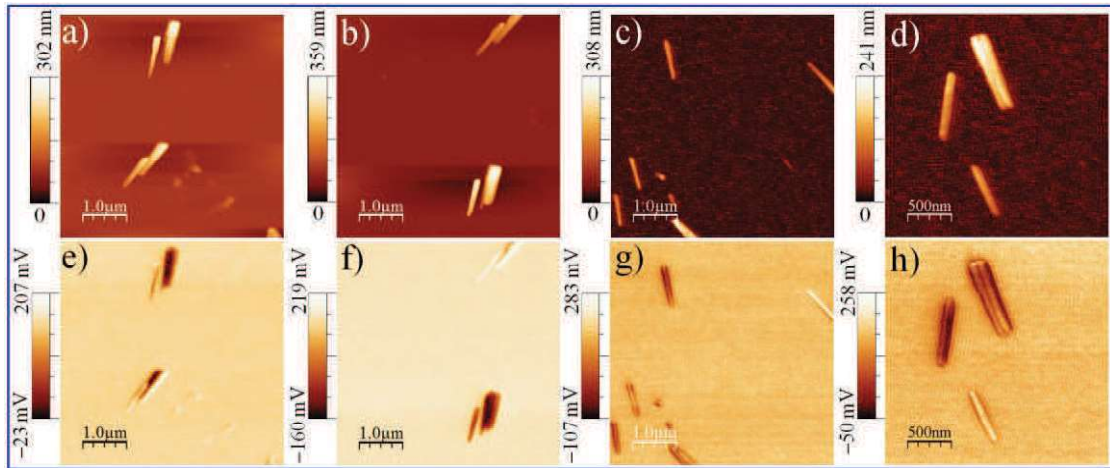


Figure 6.5. (a)-(d) Topographic images of the Si-doped InN NRs dispersed on the electron beam evaporated Au film and (e)-(h) are the corresponding CPD maps.

also found to decrease as the size of the NRs is increased (left Y-axis in Fig. 6.6). This trend can be understood by looking at the schematic band diagram of the coupled

system of conducting Pt/Ir tip and InN NR (Fig. 6.7). The work function of NRs can be written as,

$$\phi_{InN} = \chi - (E_F - E_{C-Bulk}) - E_{SBB} \dots\dots\dots (6.2)$$

Usually, for non-degenerate semiconductors electron affinity (χ) is not dependent on the doping concentration.¹³ Even though InN is a degenerate semiconductor, χ is assumed to be constant in the present study. Thus, according to the equation (6.2) the work function of InN NRs is dependent on the second ($E_F - E_{C-Bulk}$) and third (E_{SBB}) terms. The value of $E_F - E_{C-Bulk}$ is related to the carrier density (n), and in case of degenerate semiconductors the relationship can be written as $E_F - E_{C-Bulk} = k_B T (\ln(n/N_c) + 2^{-3/2} (n/N_c))$, where N_c is the effective density of states of n -type material and k_B is the Boltzmann constant. However, for NRs belonging to the same sample, one cannot expect a substantial change in the carrier density of the individual NRs.

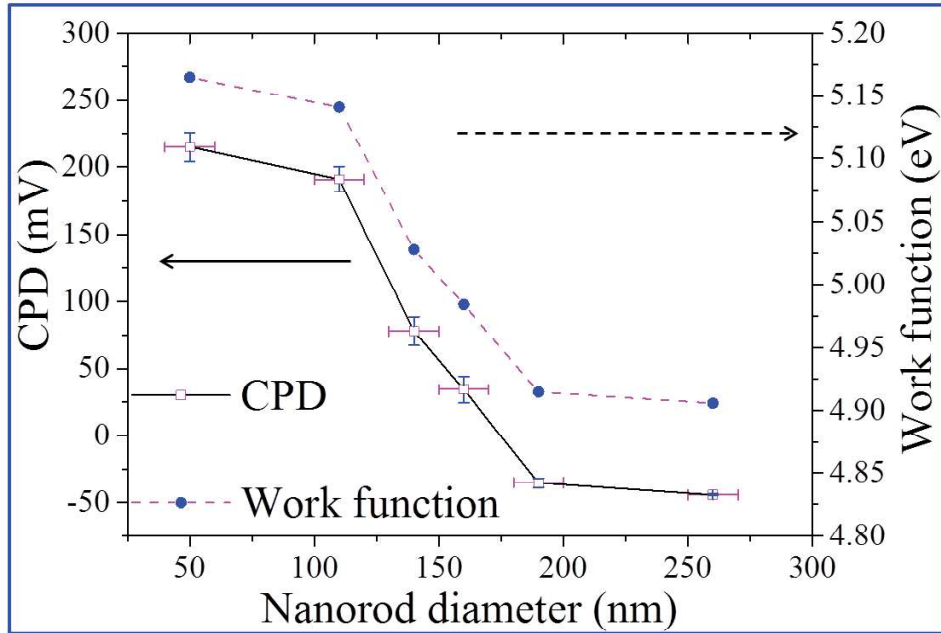


Figure 6.6. Size-dependent CPD values (right Y-axis) and corresponding calculated work function values (left Y-axis) for Si-doped InN NRs.

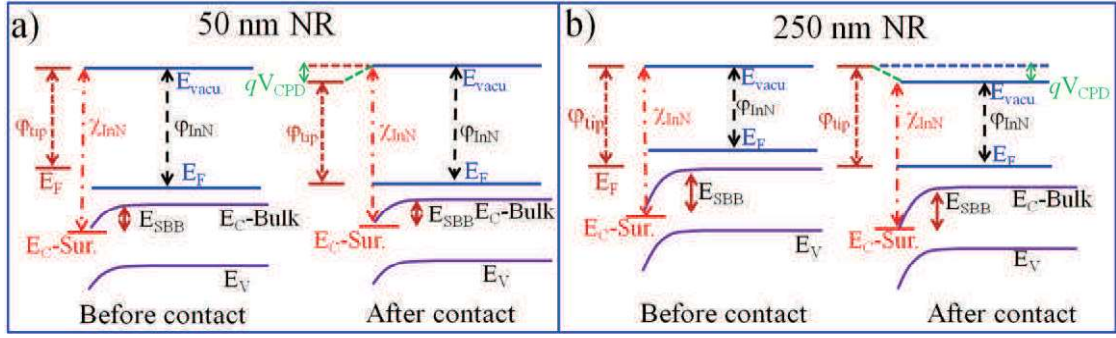


Figure 6.7. Band alignments of the coupled system of conducting AFM tip and InN NRs of sizes (a) 50 nm and (b) 250 nm before and after contact.

As a result, the effect of the second term in the variation of the work function values is negligible. Thus, the variation in the work function values of InN NRs must be attributed to the variation in the E_{SBB} . Similar kind of downward E_{SBB} work function is reported in case N-polar InN films.⁵ Thus, the variation in the work function values must be originated because of the changes in the E_{SBB} values. Thus, according to equation (6.2), the decrease of work function of the NRs indicates that the E_{SBB} is increased with the increase in the size of the NRs.

The magnitude of the E_{SBB} is related to the carrier density near the surface region. In other words, the extent of downward E_{SBB} is dependent on the sheet carrier density in the SEA.¹⁴ However, the surface carrier density is dependent on the number of surface states (N_{SS}^+). The downward E_{SBB} increases as the N_{SS}^+ increases. In most of the time, change in N_{SS}^+ is observed for samples grown with different growth conditions. In the present case, however, the studied NRs are extracted from the same sample. Thus, one cannot expect a substantial change in the N_{SS}^+ in NRs. Moreover, an explicit dependence of work function on the size of the NRs is observed (Fig. 6.6). Thus, the variation in the work function must be originated because of changes in the size of the NRs rather than N_{SS}^+ . Effect of the size of NRs on the E_{SBB} can be understood by looking the distribution of free electrons in the conduction band.

Inhomogeneous spatial distribution of free electrons in the conduction band results because of the SEA.¹⁵⁻¹⁷ It is reported that distribution of free electrons in conduction band is influenced by the size of NRs and it is inevitable when the size of NRs is ~30 nm.¹⁴ For the larger size NRs, the surface carrier density is higher as compared to that for the core of the NRs, as there can be an increment of two orders in the electron density near surface region as compared to that for the core of the NRs.¹⁷ As the size of the NRs reduces, the electrons are prone to be distributed uniformly. As a result, surface carrier density reduces for the smaller size NRs. The reduction in the surface carrier density implicates in the reduction in the value of E_{SBB} . Similar kind of band flattening is reported in case of GaN nanowires leading to the fast decay time of persistent photocurrent for the smaller size nanowires.^{18,19} Thus, the observed variation in the work function is attributed to the variation in the E_{SBB} as a result of the change in NR size. The NRs with larger diameter possesses the higher value of E_{SBB} as compared to that for the smaller sized NRs. By assuming the constant electron affinity, the difference in downward E_{SBB} for the NRs of 250 nm and 50 nm is ~260 mV.

To corroborate the assumption of the possible change of E_{SSB} with the size of the NRs, we have collected PL spectra from isolated Si-doped NRs. As discussed in the previous section, there may be an inhomogeneous distribution of free electrons in the conduction band because of downward surface band bending. In PL emission, the photo-generated electrons and holes are driven away because of the electric field produced by downward bending near surface region. There can be three regions in the NR: 1) core region with a minimum number of electrons because of the migration of electrons to surface, 2) extreme surface region with the lack of holes, and 3) optically active intermediate region with the substantial electrons and trapped holes

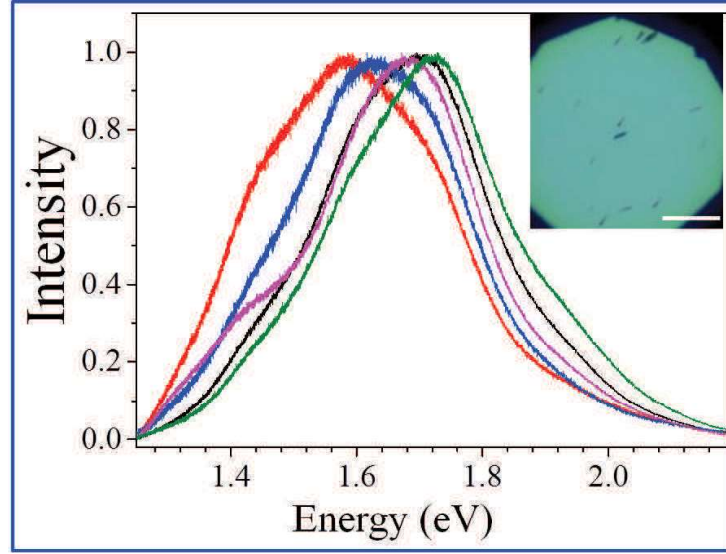


Figure 6.8. Photoluminescence spectra of isolated InN NRs. Inset figure shows the optical image of well dispersed NRs on SiO₂ substrate and the scale in the figure is 10 μm.

because of the weak electric field.¹⁷ The luminescence intensity, peak position and FWHM are strongly dependent on the surface downward band bending. The typical PL spectra collected (Fig. 6.8) from five isolated NRs after dispersing them on crystalline Si substrate (inset Fig. 6.8). It clearly depicts that there is a change in the peak position, broadening, and intensity of PL emission from one NR to another. Thus, the change in the emission parameters must be attributed to the variation in the downward surface bending values arising because of the variation in size. So, these observations confirm that indeed there is a change in the E_{SBB} in individual NRs. As a result, the work function of the NRs is dependent on the size of the NRs.

6.4 Conclusion

In conclusion, work function values of undoped and Si-doped NRs were estimated by measuring the contact potential difference of NRs using Kelvin probe force microscopy at high vacuum. Because of the small size of the undoped NRs, the CPD values have the poor signal to noise ratio. The work function values Si-doped InN

NRs are found to be strongly dependent on the size of the NRs. The observed size-dependent work function values are attributed to the variation in the downward surface band bending values with respect to the size of the NRs caused by a change in the sheet carrier density of the surface electron accumulation.

6.5 References

1. M. Nonnenmacher, M. o'Boyle and H. K. Wickramasinghe, *Appl. Phys. Lett.* **1991**, 58, 2921.
2. W. Linhart, J. Chai, R. Morris, M. Dowsett, C. McConville, S. Durbin and T. Veal, *Phys. Rev. Lett.* **2012**, 109, 247605.
3. S. Zhao, S. Fatholouloumi, K. Bevan, D. Liu, M. G. Kibria, Q. Li, G. Wang, H. Guo and Z. Mi, *Nano Lett.* **2012**, 12, 2877.
4. S. Zhao, B. Le, D. Liu, X. Liu, M. Kibria, T. Szkopek, H. Guo and Z. Mi, *Nano Lett.* **2013**, 13, 5509.
5. A. Eisenhardt, S. Krischok and M. Himmerlich, *Phys. Rev. B* **2015**, 91, 245305.
6. L. Colakerol, T. Veal, H.-K. Jeong, L. Plucinski, A. DeMasi, T. Learmonth, P.-A. Glans, S. Wang, Y. Zhang, L. Piper, P. Jefferson, A. Fedorov, T.-C. Chen, T. Moustakas, C. McConville and K. Smith, *Phys. Rev. Lett.* **2006**, 97, 237601.
7. K. K. Madapu and S. Dhara, *Appl. Phys. A* **2018**, 124, 435.
8. K. K. Madapu, A. Sivadasan, M. Baral and S. Dhara, *Nanotechnology* **2018**, 29, 275707.
9. W. Melitz, J. Shen, A. C. Kummel and S. Lee, *Surf. Sci. Rep.* **2011**, 66, 1.
10. Y. Rosenwaks, R. Shikler, T. Glatzel and S. Sadewasser, *Phys. Rev. B* **2004**, 70, 085320.
11. T. Gotschke, E. Schäfer-Nolte, R. Caterino, F. Limbach, T. Stoica, E. Sutter, K. Jeganathan and R. Calarco, *Nanotechnology* **2011**, 22, 125704.
12. K. K. Madapu, S. Polaki and S. Dhara, *Phys. Chem. Chem. Phys.* **2016**, 18, 18584
13. S. M. Sze and K. K. Ng, *Physics of semiconductor devices*. (John wiley & sons, **2006**).
14. J. Segura-Ruiz, A. Molina-Sanchez, N. Garro, A. García-Cristóbal, A. Cantarero, F. Iikawa, C. Denker, J. Malindretos and A. Rizzi, *Phys. Rev. B* **2010**, 82, 125319.
15. C.-H. Shen, H.-Y. Chen, H.-W. Lin, S. Gwo, A. Klochikhin and V. Y. Davydov, *Appl. Phys. Lett.* **2006**, 88, 253104.
16. T. Stoica, R. J. Meijers, R. Calarco, T. Richter, E. Sutter and H. Lüth, *Nano Lett.* **2006**, 6, 1541.

17. J. Segura-Ruiz, N. Garro, A. Cantarero, C. Denker, J. Malindretos and A. Rizzi, *Phys. Rev. B* **2009**, 79, 115305.
18. R. Calarco, M. Marso, T. Richter, A. I. Aykanat, R. Meijers, A. vd Hart, T. Stoica and H. Lüth, *Nano Lett.* **2005**, 5, 981.
19. H.-Y. Chen, R.-S. Chen, N. K. Rajan, F.-C. Chang, L.-C. Chen, K.-H. Chen, Y.-J. Yang and M. A. Reed, *Phys. Rev. B* **2011**, 84, 205443.

CHAPTER 7

SUMMARY OF THESIS AND SCOPE FOR FUTURE WORK

7.1 Summary of Thesis

The present thesis reported growth of InN nanostructures, and their near and far-field optical properties. In this thesis, emphasis was given to the understanding of the growth mechanism of InN nanostructures and thin films. In addition, plasmonic properties InN nanostructures, for the first time, were explored using the near-field scanning optical microscopy (NSOM). Subsequently applicability of the InN nanostructures as SERS substrate was studied. Finally, the work function of the InN nanorods (NRs) was studied using Kelvin probe force microscopy (KPFM). A summary of each chapter is presented below.

In Chapter 1, a brief literature survey was provided on the basic physical properties of InN and challenges in the synthesis of InN phase. The unique property such as surface electron accumulation (SEA) of InN was introduced. The controversies related band gap of the InN was explained based on the Burstein-Moss (BM) effect. Vibrational properties and plasmon-phonon coupled modes were elaborately discussed. In addition, the importance of measurements of the work function and the possibility of the InN as the plasmonic material were discussed. Finally, the necessity of the growth of InN nanostructures using atmospheric pressure chemical vapour deposition (APCVD) technique was emphasised.

The growth and experimental techniques used in this study were discussed in Chapter 2. The details of the APCVD technique was elaborately presented, as it was the primary growth technique. In addition, NSOM and KPFM techniques were

explicitly detailed. Role of the NSOM technique in the study of plasmonic properties was elaborately discussed along with the principle of the KPFM technique for measuring the contact potential difference (CPD).

The growth of InN nanostructures and thin films are described in Chapter 3. This chapter is categorized into two parts based on the source material used in the growth process. In the first part, the growth of the InN nanostructures was carried out using the In_2O_3 powder as source material and NH_3 as the reactive gas in the temperature range of 550–700 °C. Morphology of the nanostructures was solely dependent on the growth temperature, evolving from the quantum dot (QD) sized nanoparticles to NRs. A threshold temperature of 630 °C is recorded for the growth of NRs. At 630 °C, nucleation started with multifaceted particles having {10–12} surface planes. Subsequently, hexagonal polyhedral NRs were grown along the [0001] direction with non-polar surfaces of $\bar{1}0\bar{1}0$ planes {10–10}. Temperature-dependent evolution of morphology was explained based on the competitive processes of nucleation and growth rates. In the second part, high optical quality InN films were grown on a sapphire substrate using the APCVD technique in the temperature range of 560–650 °C. The self-seeded catalytic approach was adopted to overcome the nucleation barrier for depositing InN films. Simultaneous effect of strain and the BM shift on the optical emission properties of InN films was investigated using the Raman and photoluminescence (PL) spectroscopic studies. Compressive strain, resulting from the lattice and thermal expansion mismatch, was relaxed at high temperature by hydrostatic tensile strain produced from the N vacancies. A large blue shift of the band gap of InN (1.2 eV) was observed as a resultant effect of compressive strain in films as well as a BM shift.

In Chapter 4, the growth of InN nanostructures and their phonon structure were evaluated in the near and off-resonance conditions. High-quality InN nanoparticles were grown using an APCVD technique via a self-seeded catalytic approach in the temperature range of 580–650 °C. Samples with increasing carrier densities were grown, with the help of increasing growth temperature, to understand the role of carrier density in the optical phonon structure. The growth temperature-dependent carrier density of the nanostructures and their corresponding SEA properties were studied using the Raman spectroscopy. It was found that nanostructures grown ≥ 620 °C possess the SEA. The presence of the SEA was confirmed by Raman studies, which was further corroborated by PL and ultra-violet photoelectron spectroscopy (UPS) studies. The frequency of 2DEG corresponding to the SEA was found to be in the THz region of $54\text{--}60\text{ cm}^{-1}$ ($\sim 1.6\text{--}1.8\text{ THz}$). In addition, excitation dependent vibrational properties of the InN nanostructures were studied using Raman spectroscopy with different laser sources. Near-resonance excitation (785 nm), invoking the possible breakdown of the selection rule, induced significant changes in the Raman spectra with the appearance of the forbidden mode $B_1(\text{high})$. The intensity and frequency of the $B_1(\text{high})$ mode were observed to be strongly dependent on the carrier concentration in the system.

The plasmonic properties of InN nanostructures and its applications in SERS were explored in Chapter 5. In this chapter, the surface plasmon properties of InN nanoparticles originating from the SEA were demonstrated using the real-space mapping of the surface plasmon fields for the first time with the help of NSOM technique. The periodic fringes were observed in the NSOM images of InN nanostructures. The observed fringes were attributed to the interference of propagated

and back-reflected surface plasmon polaritons (SPPs). The wavelength of the SPPs was estimated to be in the range of 274–500 nm. The observation of SPPs was solely attributed to the 2DEG corresponding to the SEA of InN. Observation of SPPs indicated that InN with the SEA could be a promising THz plasmonic material for light confinement.

The SEA dependent SERS activity of InN nanostructures was also explored using the Rhodamine 6G (R6G) molecules. The SERS enhancement was observed for the InN nanostructures which possess the SEA. The enhancement factor of four orders ($\sim 1.4 \times 10^4$) was calculated with the assumption of monolayer coverage of analyte molecule. The SERS enhancement of InN nanostructures was attributed to the 2D plasmonic nature of InN nanostructures invoking the SEA, rather than the contributions from 3D surface plasmon resonance and chemical interaction.

In Chapter 6, the work functions of undoped and Si-doped InN NRs were estimated using the KPFM technique by measuring the CPD. The work function of doped InN NRs was found to depend on the size of NRs. Size-dependent work function of the InN NRs was attributed to the variation in the downward surface band bending caused by the SEA rather than a change in the position of Fermi level.

7.2 Scope for Future Work

The present thesis explored that InN with the SEA can act as a plasmonic material. One can further establish the plasmonic properties of well-organized InN structures such as InN meta-materials. In addition, sheet carrier density dependent surface plasmon properties can also be explored. One has to further understand the behaviour of the 2D plasmon peak in the Raman spectrum at different incident angles and in the presence of the magnetic field. Hotspot properties between degenerate plasmonic

material and noble metal nanoparticles can be carried out using the tip-enhanced Raman spectroscopy (TERS). Finally, InN is a piezoelectric material, so the influence of the SEA on the piezoelectric properties of these nanostructures can also be studied.